Investigation of the Heterodimeric ABC Exporter TmrAB using Pulsed Electron-Electron Double Resonance Spectroscopy

Dissertation

zur Erlangung des Doktorgrades

der Naturwissenschaften

vorgelegt beim Fachbereich Physik

der Johann Wolfang Goethe-Universität

in Frankfurt am Main

von

Michael Rudolph

aus Gera

Frankfurt am Main 2024

(D 30)

Vom Fachbereich Physik der Johann Wolfgang Goethe - Universität als Dissertation angenommen.

Dekan: Prof. Dr. Roger Erb

1. Gutachter: Prof. Dr. Benesh Joseph

2. Gutachter: Prof. Dr. Robert Tampé

Datum der Disputation: 10.06.2024

ABSTRACT

ATP-binding cassette (ABC) transporters shuttle diverse substrates across biological membranes. They play a role in many physiological processes but are also the reason for antibiotic resistance of microbes and multi drug resistance in cancer, and their dysfunction can lead to serious diseases. Transport is achieved through an ATP-driven closure of the two nucleotide binding sites (NBSs) which induces a transition between an inward-facing (IF) and an outward-facing (OF) conformation of the connected transmembrane domains (TMDs). In contrast to this forward transition, the reverse transition (OF-to-IF) that involves Mg^{2+}-dependent ATP hydrolysis and release is less understood. This is particularly relevant for heterodimeric ABC transporters with asymmetric NBSs. These transporters possess an ATPase active consensus NBS (c-NBS) and a degenerate NBS (d-NBS) with little or no ATPase activity. Crucial details regarding function and mechanism of the transport cycle remain elusive.

Here, these open questions were addressed using pulse electron-electron double resonance (PELDOR or DEER) spectroscopy of the heterodimeric ABC exporter TmrAB. To better understand the transport cycle, the underlying kinetics of the conformational transitions need to be elucidated. By introducing paramagnetic nitroxide (NO) spin probes at key positions of TmrAB and employing time-resolved PELDOR spectroscopy, the forward transition could be followed over time and the rate constants for the conformational transition at the TMDs and NBSs were characterized. The temperature dependence of these rate constants was further analyzed to determine for the first time the activation energy of conformational changes in a large membrane protein. For TMD opening and c-NBS dimerization, values of 75 ± 27 kJ/mol and 56 ± 3 kJ/mol, respectively were found. These values agree with reported activation energies of peptide transport and peptide dissociation in other ABC transporters, suggesting that the forward transition may be the rate-limiting step for substrate translocation.

The functional relevance of asymmetric NBSs is so far not well understood. By combining Mg^{2+}-to-Mn^{2+} substitution with Mn^{2+}-NO and NO-NO PELDOR spectroscopy, the binding of ATP-Mn^{2+}, the conformation of the NBSs, and the conformation of the TMDs could be simultaneously monitored for the first time. These results reveal an asymmetric post-hydrolytic state. Time-resolved investigation showed that ATP hydrolysis at the active c-NBS triggers the reverse transition, whereas opening of the impaired d-NBS regulates the return to the IF conformation.

ZUSAMMENFASSUNG

ATP-binding cassette (ABC) Transporter transportieren verschiedene Substrate über biologische Membranen. Sie spielen eine Rolle bei vielen physiologischen Prozessen, sind aber auch der Grund für die Antibiotikaresistenz von Mikroben und die *multi drug resistance* bei Krebs, und ihre Fehlfunktion kann zu schweren Krankheiten führen. Der Transport erfolgt über eine ATP-gesteuerte Schließung der beiden Nukleotidbindestellen (NBS), der einen Übergang zwischen einer nach innen gerichteten (IF) und einer nach außen gerichteten (OF) Konformation der verbundenen Transmembrandomänen (TMD) bewirkt. Im Gegensatz zu diesem Vorwärtsübergang ist der Rückwärtsübergang (OF-zu-IF), der eine Mg^{2+}-abhängige ATP-Hydrolyse und -Freisetzung beinhaltet, weniger gut verstanden. Dies gilt besonders für heterodimere ABC-Transporter mit asymmetrischen NBSs. Diese Transporter verfügen über eine ATPase-aktive konsensus NBS (c-NBS) und eine degenerierte NBS (d-NBS) mit geringer oder keiner ATPase-Aktivität. Entscheidende Details zu Funktion und Mechanismus des Transportzyklus sind nach wie vor ungeklärt.

Hier wurden diese offenen Fragen mit Hilfe gepulster Doppel-Elektron-Elektron-Resonanzspektroskopie (PELDOR oder DEER) des heterodimeren ABC-Exporters TmrAB untersucht. Als Elektronenspinresonanz (ESR) -Methode findet die PELDOR-Spektroskopie Anwendung zur Untersuchung der Abstände zwischen paramagnetischen Zentren in Molekülen oder Materialien. Sie beruht auf der Messung der dipolaren Kopplung zwischen Elektronenspins und bietet Einblicke in Struktur und Dynamik komplexer Systeme auf der Nanoskala. Als Ensemble-Technik liefert sie Ergebnisse über die Verteilung von Zuständen in der gemessenen Probe.

Um den Transportzyklus von TmrAB besser zu verstehen, muss die zugrunde liegende Kinetik der Konformationsübergänge aufgeklärt werden. Durch die Einführung paramagnetischer Nitroxid (NO)-Spinsonden an Schlüsselpositionen von TmrAB – an TMDs, c-NBS und d-NBS - und die Anwendung zeitaufgelöster PELDOR-Spektroskopie konnte der Vorwärtsübergang über die Zeit verfolgt werden. Durch eine Verringerung der experimentellen Temperatur auf Werte unterhalb der physiologischen Aktivität konnte die Zeit zur Gleichgeweichtseinstellung auf eine Zeitskala von Sekunden bis Minuten erhöht werden, und ermöglichte so eine zeitliche Auflösung der Konformationsübergänge. Identische Proben von TmrAB wurden unter verschiedenen Bedingungen und bei unterschiedlichen Temperaturen für

zunehmende Zeitdauern inkubiert, um zeitaufgelöste Schnappschüsse der konformationellen Zusammensetzung des Probenensembles zu erhalten. Unter Bedingungen, bei denen ATP binden kann, jedoch nicht hydrolysiert wird, zeigen die TMD-Spinsonden eine zunehmende Öffnung von der IF- zur OF-Konformation. Die NBS-Spinssonden zeigen eine zunehmende Dimerisierung mit fortschreitender Inkubationsdauer. Zusätzlich sind beide Effekte bei erhöhter Temperatur stärker ausgeprägt und laufen schneller ab. Ein geeignetes kinetisches Modell der Konformationsübergänge wurde an die Populationen von OF-Konformation und dimerisierter NBS als reversible Reaktion erster Ordnung angepasst, um die Geschwindigkeitskonstanten für den Konformationsübergang an den TMDs und NBSs so zu charakterisieren. Die Temperaturabhängigkeit dieser Geschwindigkeits-konstanten wurde weitergehend mittels der Arrhenius-Gleichung analysiert, um zum ersten Mal die Aktivierungsenergie von Konformationsänderungen in einem großen Membranprotein zu bestimmen. Dabei wurden für die TMD-Öffnung und die c-NBS-Schließung Werte von 75 ± 27 kJ/mol bzw. 56 ± 3 kJ/mol ermittelt. Diese Werte stimmen mit berichteten Aktivierungsenergien für Peptidtransport und Peptiddissoziation in anderen ABC-Transportern überein, was darauf hindeutet, dass der Vorwärtsübergang der geschwindigkeitsbestimmende Schritt für die Substrattranslokation sein könnte.

Dieses Experiment wurde wiederholt, nachdem das konservierte katalytische Walker-B-Glutamat in der c-NBS durch Glutamin (E-to-Q) ersetzt wurde, was zu $TmrA^{EQ}B$ führte. Diese Substitution verringert die ATPase-Aktivität erheblich und stabilisiert dadurch die NBSs in ihrem geschlossenen Zustand. Die Geschwindigkeit und das Ausmaß des Übergangs von der IF- zur OF-Konformation wurde dadurch deutlich erhöht. Bemerkenswert ist, dass die $TmrA^{EQ}B$-Daten im Arrhenius-Graph einen viel steileren Anstieg aufweisen, was zu einer 50 kJ/mol höheren Aktivierungsenergie für den Vorwärtsübergang und einer 60 kJ/mol höheren Aktivierungsenergie für den Rückwärtsübergang führt. Dieser relative Anstieg der Aktivierungsenergie bewirkt den schnelleren Übergang zur OF-Konformation und stabilisiert die OF-Konformation durch eine weitere Verringerung des Rückwärtsübergangs. Neben seiner wesentlichen Rolle für die ATP-Hydrolyse spielt das katalytische Glutamat damit eine Schlüsselrolle bei der Regulierung der Kinetik des Übergangs von der IF- zur OF-Konformation.

Auf der Grundlage der beobachteten Auswirkungen des Verlusts der ATPase-Funktion an der c-NBS wurde der Einfluss der ATP-Hydrolyse auf die Übergangskinetik weiter untersucht. An den TMDs verschoben sich die Populationen innerhalb von 10 s in die OF-Konformation, was eine deutlich beschleunigte Kinetik im oberen Millisekundenbereich im Vergleich zum Übergang unter nicht-hydrolysierenden

Bedingungen ergab. Andererseits zeigt die c-NBS eine anfänglich stark beschleunigte Dimerisierung, gefolgt von einer langsamen Abnahme der geschlossenen Konformation über die restliche Inkubationszeit. Bei der d-NBS ist dieses Verhalten nicht zu beobachten. Die Hydrolyse-bedingte Abnahme des verfügbaren freien ATP führt dazu, dass weniger Transporter im geschlossenen c-NBS-Zustand verbleiben. Da die d-NBS eine deutlich verringerte ATPase-Aktivität hat, wird sich dieser allmähliche Rückgang des ATP-Spiegels zuerst und stärker auf die c-NBS auswirken. Die Tatsache, dass die TMDs nicht empfindlich auf die Abnahme der ATP-Konzentration reagieren, deutet darauf hin, dass die Öffnung der c-NBS allein nicht ausreicht, um die TMDs in die IF-Konformation zurückzuführen. Die Frage, ob sich eine oder beide NBSs während eines Transportzyklus vollständig öffnen, wird derzeit diskutiert. Es ist gut möglich, dass verschiedene Transporter unterschiedliche Mechanismen aufweisen, die durch die zugrundeliegende Konformationskinetik der (symmetrischen oder asymmetrischen) NBSs und TMDs vorgegeben sind.

Die funktionelle Bedeutung asymmetrischer NBSs ist bisher noch nicht geklärt. Magnesiumionen sind notwendig, damit die Hydrolyse von ATP zu ADP durch ABC-Transporter katalysiert werden kann. Dies bedeutet, dass Mg^{2+}-Ionen während des Transportzyklus in den NBS lokalisiert sein müssen. Aufgrund ihrer Ähnlichkeit in Größe und Ladung kann Mg^{2+} in biologischen Systemen und biochemischen Reaktionen durch Mn^{2+} ersetzt werden. Im Gegensatz zu Mg^{2+} ist zweiwertiges Mangan jedoch paramagnetisch und kann daher als EPR-spektroskopisch aktiver Ersatz für Magnesium dienen. Durch die Kombination von Mg-zu-Mn-Substitutionen mit Mn^{2+}-NO-PELDOR-Spektroskopie konnten die Bindung von ATP-Mn^{2+} sowie die Konformation der NBSs erstmals gleichzeitig verfolgt werden. Diese Ergebnisse zeigten, dass ATP-Mn^{2+} bevorzugt in der c-NBS hydrolysiert wird, während die d-NBS ATP-Mn^{2+} stabil bindet.

In einem weiteren Schritt wurde das soeben beschriebene Mn^{2+}-NO-PELDOR-Experiment mit einer NO-NO-PELDOR-Messung kombiniert, die die Konformationsänderung an den TMDs untersuchte, um zwei der wichtigsten Transporterdomänen und ihre Konformationszustände zu korrelieren. Dieser Ansatz ist in der Literatur bisher nicht beschrieben worden. Es ergab sich ein asymmetrischer post-hydrolytischer Zustand: aus der Untersuchung der TMDs war ersichtlich, dass TmrAB unter Hydrolysebedingungen sowohl in der IF- als auch in der OF-Konformation vorliegt. Die Beobachtungen der NBS zeigen, dass die c-NBS bereits ihr ATP-Mn^{2+} durch die schnelle Hydrolyse verloren hat. Das bedeutet, dass sich ein erheblicher Teil der Transporter noch in der OF-Konformation befindet, während das ATP bereits an der c-NBS hydrolysiert wurde. Diese Beobachtung ist ein starkes Indiz für die

asymmetrische Kopplung von c-NBS und d-NBS an die TMDs. Dieser asymmetrische Verlust von ATP aus der OF-Konformation würde die Freisetzung von ADP und anorganischer Phosphatgruppe aus einer teilweise geschlossenen c-NBS erfordern. Diese Freisetzung könnte entweder durch einen Tunnel in der c-NBS und/oder durch eine teilweise Öffnung der c-NBS erfolgen, um den Nukleotidaustausch zu ermöglichen.

Durch Wiederholung der gleichzeitigen Messung von NO-NO- und Mn^{2+}-NO-PELDOR in katalytisch beeinträchtigtem $TmrA^{EQ}B$ konnte eine Okklusion von ATP-Mn^{2+} an der c-NBS unter hydrolysierenden Bedingungen erreicht werden. Somit führt die E-zu-Q-Substitution zu einer stabilen Okklusion von Mn^{2+}-ATP an der c-NBS und die drastisch verringerte ATP-Hydrolyse führt dazu, dass ein größerer Anteil Transporter in der OF-Konformation stabilisiert ist. Die hohe Präsenz von lokalisiertem Mn^{2+} in beiden NBSs ermöglichte außerdem die Messung von Mn^{2+}-Mn^{2+}-PELDOR. Die gleichzeitige Bestimmung von NO-NO-, Mn^{2+}-NO- und Mn^{2+}-Mn^{2+}-Interspin-Abständen in ein und derselben Probe ist bisher noch nicht durchgeführt worden. Der hier entwickelte experimentelle Ansatz könnte in Zukunft auch auf homodimere Systeme angewendet werden, um die katalytische Asymmetrie zu untersuchen.

Durch die Kombination des Ansatzes zur zeitaufgelösten Probenvorbereitung mit Mn^{2+}-NO PELDOR-Messungen kann das dynamische Verhalten von zwei wichtigen Proteindomänen gleichzeitig beobachtet und verglichen werden. Durch gleichzeitige NO-NO- und Mn^{2+}-NO-PELDOR-Spektroskopie konnte die Schließung der TMDs über einen Zeitraum von 5 min beobachtet werden, während nur die d-NBS ein okkludiertes Mn^{2+} beherbergt, das über diesen Zeitraum verloren geht. Die Quantifizierung der Modulationstiefe der Mn^{2+}-NO PELDOR-Messungen zeigte weiterhin, dass das Schließen der TMDs und der Verlust von Mn^{2+} aus der d-NBS korrelierte Prozesse sind. Es wurde beobachtet, dass sich in Gegenwart von ATP ein erheblicher Anteil der c-NBS in der geschlossenen Konformation befindet und TmrAB nicht in seine IF-Konformation zurückkehren kann. Nur durch ATP-Entfernung kann die Rückkehr in den IF-Zustand eingeleitet werden, was mit dem Verlust von ATP-Mn^{2+} aus der c-NBS einhergeht. Diese Beobachtungen führten zu dem Schluss, dass die Hydrolyse an der c-NBS der erste Schritt sein muss, um die Rückkehr der TMDs in die IF-Konformation einzuleiten. Die Hydrolyse von ATP an der c-NBS schwächt das NBD-Dimer ausreichend, um den Rückwärtsübergang energetisch zu erleichtern. Der Verlust des zweiten ATP in der d-NBS könnte dann zu einer vollständigen Dissoziation des NBD-Dimers führen und die Rückkehr von TmrAB in den IF-Zustand bewirken.

Der Einfluss von Mg^{2+} auf den Rückwärtsübergang wurde weiter untersucht. Die Beobachtungen an den TMDs und c-NBS belegen erneut die Bedeutung der Hydrolyse

an der c-NBS für den Rückwärtsübergang. Interessanterweise hatte eine ADP-Konzentration von 10 mM einen beschleunigenden Einfluss auf den Rückwärtsübergang. Es könnte sein, dass ADP als Bindungskonkurrent zu ATP in der d-NBS fungiert und durch den Ersatz von unhydrolysiertem ATP dort den Rückwärtsübergang beschleunigt. Dies wird durch ein Kontrollexperiment in katalytisch beeinträchtigtem $TmrA^{EQ}B$ gestützt: hier zeigt ADP keine Wirkung auf den Rückwärtsübergang, weil ohne ATP-Hydrolyse an der c-NBS das NBD-Dimer ausreichend stabilisiert ist und der ATP-ADP-Austausch an der d-NBS wenig Einfluss auf die Rückkehr in den IF-Zustand hat. Wie ADP hatte auch eine Substratkonzentration von 50 µM (1:1) eine beschleunigende Wirkung auf den Rückwärtsübergang. Dies war eine überraschende Beobachtung und wurde bisher nicht beschrieben. Da dieser Effekt im E-to-Q-Hintergrund nicht zu beobachten war, kann angenommen werden, dass es sich bei dieser Beschleunigung ebenfalls um einen post-hydrolytischen Effekt handelt. Nach der ATP-Hydrolyse an der c-NBS und der daraus resultierenden Schwächung des NBD-Dimers und der OF-Konformation könnte das Substrat mit der nun energetisch leichter zugänglichen IF-Konformation interagieren, zu der es eine hohe Affinität aufweist, und so den IF-Zustand stabilisieren und die Rückkehr zu ihm beschleunigen. Diese Hypothese bedarf jedoch sorgfältiger Überprüfung.

Zusammengenommen vertiefen die hier vorgestellten Ergebnisse unser Verständnis des Transportzyklus in heterodimeren ABC-Transportern. Der Transportmechanismus in TmrAB kann auf der Grundlage dieser neuen Erkenntnisse detailliert dargestellt werden. Es konnte gezeigt werden, dass die Dimerisierung der NBSs und das Öffnen der TMDs endotherme Prozesse sind, und dass ohne ATP-Bindung an den NBSs die IF-Konformation auch bei höheren Temperaturen der bevorzugte Zustand ist. Zwar kann die thermische Energie für die NBD-Dimerisierung auch ohne ATP ausreichen, doch erst die Bindung von ATP stabilisiert die OF-Konformation ausreichend, um den Substrattransport zu ermöglichen. Beim IF-zu-OF-Übergang hat der Vorwärtsübergang eine Aktivierungsenergie, die etwa 30 kJ/mol höher ist als der Rückwärtsübergang. Bei den hohen physiologischen Temperaturen von TmrAB wird der Vorwärtsübergang begünstigt. Es ist möglich, dass die NBS-Schließung und die TMD-Öffnung nacheinander (über einen Zwischenzustand) oder gleichzeitig erfolgen. Die ATP-Hydrolyse an der c-NBS destabilisiert anschließend den OF-Zustand und ist der Auslöser für den Beginn des Rückwärtsbergangs. Dadurch könnte ein okkludierter Zwischenzustand entstehen, der sich mit beschleunigter Geschwindigkeit vollständig in die IF-Konformation umkehrt. Mit einer stark reduzierten ATPase-Aktivität bindet die d-NBS stabil ATP. Dies verhindert die

vollständige Öffnung der (beiden) NBS und führt zu einem asymmetrischen post-hydrolytischen Zustand. Die langsame Hydrolyserate der d-NBS könnte als zellulärer "Energiesparmodus" dienen. Mit einer so veränderten Energielandschaft ist ein heterodimerer ABC-Transporter in der Lage, sowohl die IF- als auch die OF-Konformation zu erreichen, ohne dass beide ATPs in einem Transportzyklus hydrolysiert werden müssen. Dies könnte auch die Lebensdauer der OF-Konformation verlängern und die Freisetzung von Substrat aus der niedrigaffinen Bindungstasche ermöglichen. Das Gesamtgleichgewicht könnte durch ein Wechselspiel zwischen Mg^{2+}-ATP-, Mg^{2+}-ADP- und Substratkonzentrationen sowie den Raten für Vorwärts- und Rückwärtsübergänge reguliert werden.

Die zeitaufgelöste Präparation von Proben in Kombination mit einer temperaturabhängigen Beobachtung der Konformationsverteilungen durch PELDOR-Spektroskopie eröffnet eine neue Methodik zur Untersuchung der Kinetik von Biomolekülen. Sie kann dazu beitragen, die komplexen Pfade der Konformationsübergänge vollständig zu verstehen. Zusammen mit der strategischen Kombination von Versuchsbedingungen mit verschiedenen paramagnetischen Sonden lassen sich wichtige Aspekte der Funktion von ABC-Transportern aufklären. Aber es sind auch neue Fragen aufgetaucht, und es bleiben viele Herausforderungen und Möglichkeiten. Inwiefern unterscheiden sich katalytisch symmetrische Transporter von ihren asymmetrischen Gegenstücken? Wie beeinflusst die ATP-Hydrolyse mechanistisch die Konformationskinetik? Wie beeinflussen die biophysikalischen Eigenschaften der Lipidmembran die Aktivität der ABC-Transporter? Wie wirkt sich die Anwesenheit von Substrat auf den Vorwärtsübergang aus?

Für diese Fragen sind die dynamischen Eigenschaften von ABC-Transportern von zentraler Bedeutung. Experimentell flexible Ansätze, die hochauflösende Informationen über dynamische Eigenschaften von Proteinkonformationen liefern, wie die PELDOR-Spektroskopie, werden daher für die Untersuchung von ABC-Transportern entscheidend bleiben.

Letztendlich wird die große Herausforderung darin bestehen, unser mechanistisches Verständnis in neue Therapien gegen Krankheiten umzusetzen, die auf Störungen der ABC-Transporter oder der Multi Drug Resistance beruhen. Dazu müssen verschiedene, sich ergänzende wissenschaftliche Bereiche zusammenarbeiten, wobei noch unbekannte und spannende Techniken auf ihre Entdeckung warten.

Wir stehen selbst enttäuscht und sehn betroffen
Den Vorhang zu und alle Fragen offen.

(Berthold Brecht, Der gute Mensch von Sezuan)

CONTENTS

LIST OF TABLES

LIST OF FIGURES

SYMBOLS

$\boldsymbol{A}$	hyperfine tensor
a_{iso}	isotropic hyperfine coupling constant
$\boldsymbol{B}_0$	static magnetic field vector
$\boldsymbol{B}_1$	oscillating magnetic field vector
B_1	microwave field
$\mathbf{D}$	zero-field splitting tensor (eq 1.19)
$\mathbf{D}$	dipole-dipole coupling tensor (eq 1.22)
D	axial zero-field parameter
E	rhombic zero-field parameter
E_a	activation energy
$\boldsymbol{g}$	g tensor
g_e	g factor of the free electron, 2.0023193043737
g_{eff}	effective g value
g_{iso}	isotropic g value
g_n	nuclear g factor
$\mathcal{H}$	spin Hamiltonian operator
$\mathcal{H}_0$	static spin Hamiltonian operator
h	Planck constant, $6.62606876 \times 10^{-34} Js$
$\hbar$	$h/2\pi$, $1.054571596 \times 10^{-34} Js$
$\boldsymbol{I}$	nuclear spin vector operator
I	nuclear spin quantum number
$\boldsymbol{J}$	exchange coupling tensor
$\boldsymbol{K}$	kernel matrix
K_0	elementary kernel
k	decay rate constant
k_1 / k_{-1}	forward / reverse rate constant
$\boldsymbol{L}$	orbital angular momentum
$\boldsymbol{M}$	total magnetic moment vector

m_I	nuclear spin projection quantum number
m_S	electron spin projection quantum number
$\boldsymbol{P}$	distance distribution vector
$\widetilde{\boldsymbol{P}}$	nuclear quadrupole tensor
P_{IF}	population of the inward-facing TMD conformation
P_{OF}	population of the outward-facing TMD conformation
P_{open}	population of the open NBS conformation
P_{closed}	population of the closed NBS conformation
Q	nuclear quadrupole moment
$\boldsymbol{q}$	electric field gradient parameter
R	universal gas constant, $8.31446261815324 \times 10^{-34} JK^{-1}mol^{-1}$
$\boldsymbol{r}$	distance vector
r	distance
$\boldsymbol{S}$	electron spin vector operator
S	electron spin quantum number
$\boldsymbol{T}$	dipolar hyperfine coupling tensor
T	temperature
T_m	phase memory relaxation time
T_1	longitudinal relaxation time
T_2	transverse relaxation time
t	time
$\boldsymbol{V}$	dipolar signal vector
β_e	Bohr magneton, $9.27400899 \times 10^{-24} JT^{-1}$
β_n	nuclear magneton, $5.05078317 \times 10^{-27} JT^{-1}$
Δ	modulation depth
η	asymmetry parameter (nuclear quadrupole interaction)
θ	polar angle between z-axis and vector (eq 1.9)
θ	flip angle between effective field in rotating frame and z-axis (eq 1.28)
$\boldsymbol{\mu}_S$	spin magnetic moment
μ_0	permeability of vacuum, $4\pi \times 10^{-7} T^2 J^{-1} m^3$
τ_c	rotational correlation time
ϕ	polar angle in the xy-plane (eq 1.9)

ω	frequency, $\omega = 2\pi\nu$
ω_{nut}	Rabi frequency
ω_S	Larmor frequency
Ω_S	resonance offset frequency
$\mathbf{1}$	unit matrix

ABBREVIATIONS

10xHis	decahistidine
ABC	ATP-binding cassette
ADP	adenosine 5’-diphosphate
AIC	Akaike information criterion
AMP-PNP	5'-adenylyl-β-γ-imidodiphosphate
APCs	antigen-representing cells
ATP	adenosine 5’-triphosphate
ATPase	adenosine 5’-triphosphatase
ATPγS	adenosine 5’-O-(3-thio)triphosphate
AWG	arbitrary waveform generator
cAMP	cyclic adenosine monophosphate
CFTR	cystic fibrosis transmembrane conductance regulator
CH	coupling helix
CNBD	cyclic-nucleotide binding domain
c-NBS	consensus NBS
cryo-EM	cryogenic electron microscopy
cs	consensus sequence
cw	continuous wave
Cys	cysteine
DEER	double electron-electron resonance
d-NBS	degenerate NBS
DNP	dynamic nuclear polarisation
E.coli	*Escherichia coli*
E_a	activation energy
ECF	energy coupling factor
EDFS	echo-detected field sweep / echo-detected field-swept
EDNMR	ELDOR-detected NMR
EDTA	ethylenediaminetetraacetic acid

EFG	electric field gradient
ELDOR	electron-electron double resonance
ENDOR	electron-nuclear double resonance
EPR	electron paramagnetic resonance
ER	endoplasmic reticulum
E-to-Q / EQ	glutamate-to-glutamine (substitution)
EZ	electron Zeeman (interaction)
FID	free induction decay
FL	fluorescein
FRET	Förster resonance energy transfer
FT	Fourier transformation
FTIR	Fourier transform infrared spectroscopy
HEPES	4-(2-hydroxyethyl)-1-piperazineethanesulfonic acid
HF	hyperfine (interaction)
HSV	herpes simplex virus
ICP-47	infected cell protein 47
IF	inward-facing
IMAC	immobilized metal affinity chromatography
IPTG	isopropyl β-D-1-thiogalactopyranoside
K5F	short peptide with a FL-labelled lysine residue, substrate of TmrAB
LPS	lipopolysaccharide
MAS	magic angle spinning
MD	molecular dynamics
MDR	multidrug resistance
MHC I	major histocompatibility complex class I
MHQ	microsecond freeze-hyperquenching
MTSL	1-oxyl-2,2,5,5-tetramethyl-3-pyrroline-3-methyl)methanethiosulfonate spin label
MOPS	3-(N-morpholino)propanesulfonic acid
NBD / NBDs	nucleotide binding domain / domains
NBS / NBSs	nucleotide binding site / sites
NMR	nuclear magnetic resonance

NO	nitroxide
NQ	nuclear quadrupole (interaction)
NTPase	nucleoside triphosphatase
NZ	nuclear Zeeman (interaction)
OF	outward-facing
PDA	point dipole approximation
PDB	protein data bank
PDS	pulsed dipolar spectroscopy
PELDOR	pulse electron-electron double resonance
P_i	orthophosphate
PLD / PLDs	periplasmic domain(s)
RFQ / µRFQ	rapid freeze quench / microfluidic rapid freeze quench
s/n	signal-to-noise
SAXS	small-angle X-ray scattering
SBD	substrate binding domain
SBP	substrate binding protein
SDM	side-directed mutagenesis
SDSL	site-directed spin labelling
SDS-PAGE	sodium dodecyl sulfate polyacrylamid gel electrophoresis
SF	stopped-flow (mixing setup)
smFRET	single-molecule FRET
SRT	shot repetition time
ssNMR	solid state NMR
TAP	transporter associated with antigen processing
TEM	transmission electron microscopy
TM	transmembrane helix
TMD / TMDs	transmembrane domain(s)
TmrAB	*Thermus thermophilus* multidrug resistance protein AB
TR	time-resolved
trEM	time-resolved cryo-EM
UR	unlocked return
WT*	cysteine-free variant (of TmrAB)

ABBREVIATIONS

XXS	X-ray solution scattering
ZFS	zero-field splitting (interaction)
β-DDM	dodecyl-β-D-maltosid
β-ME	β-mercaptoethanol

1 INTRODUCTION

1.1 Membrane transport

Biological membranes are selectively permeable barriers that surround cells and cellular compartments. These membranes play a crucial role in maintaining the internal environment of cells by controlling the passage of various molecules and ions into and out of the cell.[1] The transport of molecules across cell membranes is essential for many cellular processes, including nutrient uptake, waste removal, signal transduction, and the maintenance of ion balance.[2] For this reason, membrane proteins and other biomolecules involved in the regulation of membrane transport are the target for a rapidly rising number of therapeutics.[3] The mechanisms of membrane transport are highly diverse, but can be categorized into two major types: passive diffusion and active transport.[4]

Passive diffusion involves the direct movement of molecules across the membrane. It occurs down a concentration gradient, from an area of higher concentration to an area of lower concentration. One of the most common types of passive transport is diffusion, where small, nonpolar molecules such as oxygen and carbon dioxide can freely move across the lipid bilayer of the membrane. Facilitated diffusion is another form of passive transport that involves the movement of molecules across the membrane with the help of specific membrane proteins called carriers or channels. These proteins facilitate the diffusion of certain substances that would otherwise be unable to cross the lipid bilayer due to their size, charge, or hydrophilic nature. For passive and facilitated diffusion, energy is only required for the solute to lose its hydration sphere, diffuse through the lipid bilayer, and then acquire a new hydration sphere on the other side of the membrane.[5]

Active transport, on the other hand, requires the expenditure of additional energy to transport molecules against their concentration gradient, from an area of lower concentration to an area of higher concentration. The process of primary active transport is achieved by specialized integral membrane proteins called transporters or pumps, which utilize cellular energy, often in the form of adenosine triphosphate (ATP) or other nucleotides, to actively transport ions or molecules across the membrane. Another type of active transport is called secondary active or coupled transport. In coupled transport, the movement of one molecule or ion is coupled with the movement of another molecule or ion down its concentration gradient. This allows the favorable movement of one molecule to drive the uphill movement of another molecule.[4]

Membrane transport is a highly regulated process, and the selectivity of membranes is critical for maintaining cellular homeostasis.[6] The presence of specific transport proteins and channels in the membrane determines the permeability of different molecules and ions. Cells can control the activity of these transporters through various mechanisms such as regulation of protein expression, post-translational modifications, and the use of energy sources.[7–9]

1.2 ABC transporters

Among the group of active transport proteins, ATP-binding cassette (ABC) transporters constitute one of the largest and most diverse superfamilies. They are found in all domains of life, including bacteria, archaea, and eukaryotes, and are therefore considered to be among the oldest gene families.[10] They are polyphyletic and have thus evolved more than once independently, which gave rise to several protein subfamilies.[11] ABC transporters play crucial roles in the translocation of a wide range of molecules across cellular membranes, including ions, nutrients, metabolites, lipids, and drugs. They are involved in many physiological processes, as will be elaborated in chapter 1.2.4. On the other hand, dysfunction of ABC transporters, either at expression or at activity level, has been associated with genetic diseases such as Tangier disease, obstetric cholestases, and cystic fibrosis[12], while disorders at the blood-brain barrier can lead to severe neurological diseases.[13] Furthermore, they are responsible for multidrug resistance (MDR) by effluxing drugs from the targeted cells. MDR therefore leads to both the antibiotic resistance of microbes and the failure of anticancer chemotherapy and thus poses a serious threat to the public health.[14,15]

1.2.1 Structure of ABC transporters

Thanks to technical advances, our knowledge on the structural basis of ABC transporters has significantly expanded over the last decades. The underlying architecture of ABC transporters consists of four core domains: two evolutionarily highly conserved nucleotide-binding domains (NBDs) that represent the unifying element of ABC systems, and two structurally variable transmembrane domains (TMDs) that constitute the translocation pathway (**Figure 1.1a**).[16] These four domains can be organized in various ways and genetically encoded as separate polypeptides, or fused together in any combination to result in multidomain polypeptides.[17] In bacteria and archaea, often distinct subunits are formed, or they are combined into homo- or heterodimerizing half-transporters, each half consisting of one TMD and one NBD (**Figure 1.1b**). Eukaryotic ABC transporters are either built from two half-

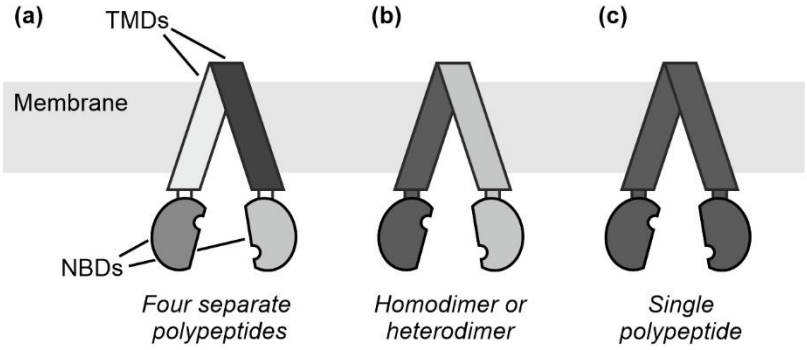

Figure 1.1. Schematical structure of an ATP-binding cassette (ABC) transporter. Each transporter consists of two transmembrane domains (TMDs) coupled to two nucleotide binding domains (NBDs). These domains can be organized in various ways and are often either encoded as distinct polypeptides (a), or with one TMD and one NBD fused together, respectively, resulting in a homodimeric or heterodimeric hybrid protein (b), or fused into one single polypeptide (c).

transporters or as a full transporter, where all four domains are expressed as one polypeptide chain (**Figure 1.1c**).[18] The exact architecture of the NBDs is illustrated by the maltose transporter $MalFGK_2$ in **Figure 1.2**. The NBDs consist of two subdomains: a larger catalytic core similar to RecA-type motor ATPases that is expanded by an ABC-specific three-stranded antiparallel β-sheet (ABCβ), as well as an α-helical subdomain (ABCα) unique to ABC transporters (**Figure 1.2a**).[19,20] The RecA-like subdomain consists of a six-stranded β-sheet surrounded by four α-helices. It is associated with phosphate binding and is also found in other P-loop containing nucleoside triphosphate hydrolases (NTPases). The eponymous ATP-binding cassette is a characteristic and defining element found in the NBDs and contains seven highly conserved motifs: A-loop, Walker A motif, Q-loop, signature motif, Walker B motif, D-loop and H-switch (**Figure 1.2b**).[21,22] The A-loop is part of the ABCβ region and contains an aromatic residue (often a tyrosine) and mediates the binding of ATP by π-π-stacking interaction with the adenine (**Figure 1.2c**). The Walker A motif with the consensus sequence (cs) GxxGxGK(S/T) (x can be any residue) is localized in the RecA-type core and forms the P-loop. This phosphate-binding loop contains a highly conserved lysine residue that is also involved in ATP binding by interacting with the β- and γ-phosphate of ATP. Furthermore, the serine or threonine residue following the lysine coordinates the Mg^{2+} ion associated to the ATP.[23] On the P-loop follows the Q-loop with the cs

ϕ(ϕ/Q)Q (ϕ can be any hydrophobic residue) that coordinates the Mg^{2+} ion through its glutamine residue. It is also involved in sensing the γ-phosphate and interacting with the TMDs. The signature motif is only found in the ABC superfamily and is located in the ABCα subdomain. It has the cs LSGGQ and forms the C-loop. The C-loop siphons the positive charge of the helical dipole to the terminal phosphate of ATP and contributes to NBD dimerization upon ATP binding (see chapter 1.2.2).[24] The Walker B motif with the cs: ϕϕϕϕDE (ϕ can be any hydrophobic residue) contains an aspartate that helps to coordinate the Mg^{2+} ion. The aspartate is followed by the putatively catalytic glutamate, which could polarize the attacking water molecule and thus enables ATP hydrolysis.[25] The Walker B motif is followed by the D-loop with the cs SALD. The D-loop is involved in the formation of the ATP hydrolysis site by positioning the attacking water.[26] Finally, the H-switch could stabilize the catalytic transition state through its histidine residue that helps positioning the attacking water, nucleotide base and magnesium ion.[23]

1.2.2 Function of the nucleotide binding domains

The main function of ABC transporters is the ATP-induced conformational change between distinct conformations that is – in most systems – coupled to substrate transport, either in an import or an export direction. For this, large-scale rearrangements of both the NBDs and the TMDs are necessary. In line with their different phylogenetic origins, the structurally variable TMDs show vast differences in their function and mechanism that will be examined in chapter 1.2.4, and mechanistic similarities within the ABC superfamily are restricted to the conserved dimerization of the NBDs.[27] In the absence of ATP, the NBDs exist in an open conformation and are more or less separated, depending on the transporter at hand. The binding of two ATP molecules induces dimerization of the NBDs. For this, the Walker A and B motifs, as well as the A-, Q-, and H-loops of NBD1 and the signature motif of NBD2 form one nucleotide binding site (NBS), and vice versa for NBD2-NBD1 (**Figure 1.2a,c**). This leads to two ATP molecules being sandwiched between the dimerized NBDs. It was also shown that the RecA-like subdomain and the ABCα subdomain undergo an induced-fit rotation toward each other.[28]

The formation of the closed NBD conformation is essential for ATP hydrolysis, and prevention of dimer formation results in the loss of ATPase activity.[29,30] The C-loops of the two signature motifs align the ATP molecules for hydrolysis by directing the positive charge of the helical dipole of one helix to the γ-phosphate of ATP, priming it for the attacking lytic water.[31] As with all kinases, the presence of a Mg^{2+} ion is required for ATP hydrolysis to take place. The Mg^{2+} coordinates to the β- and γ-

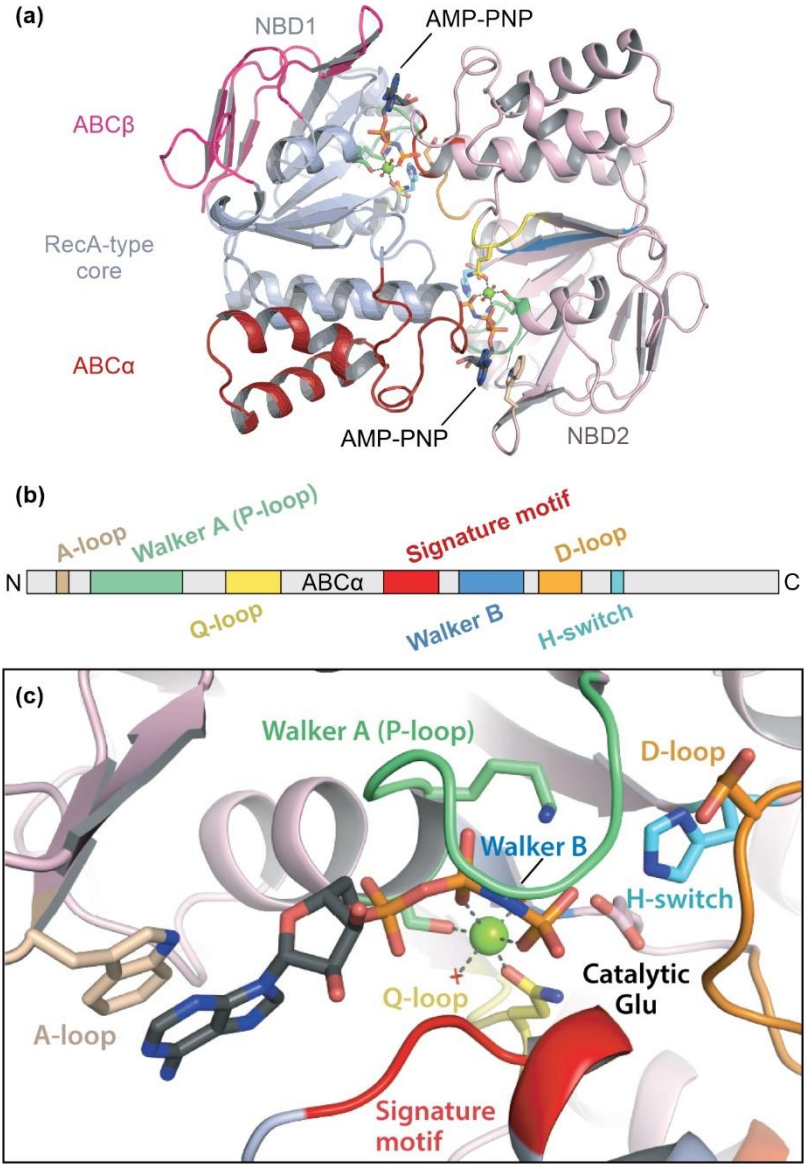

(Figure caption overleaf)

[p. 5] Figure 1.2. The NBD and the role of the ABC in ATP binding and NBS formation. This is illustrated by the adenylyl-imidodiphosphate- (AMP-PNP) bound structure of the maltose transporter $MalFGK_2$ with the Protein Data Bank (PDB) code 3RLF. (a) View onto the isolated, dimerized NBDs ($MalK_2$ subunit) of $MalFGK_2$ from the membrane towards the cytoplasm. For the NBD1, the ABCα (red) RecA-type core (light blue) and ABCβ (magenta) are highlighted. The bound nonhydrolyzable ATP analog AMP-PNP and the Mg^{2+} ion (green) are included For the NBD2, the sequence motifs are highlighted according to panel b. (b) Linear arrangement of sequence motifs in the NBD. (c) Zoom into a simplified version of one of the NBSs in dimerized $MalK_2$. The sequence motifs are colored according to panel b, and important residues are depicted as sticks. Interactions within the octahedral coordination sphere of the Mg^{2+} ion (green) are indicated by dashed lines. Figure adapted and modified from[23].

phosphoryl groups, while the beforementioned oxygen-containing sidechains of P-loop, Q-loop and B motif complete the octahedral coordination (see **Figure 1.2c**).[32] This coordination is necessary to position the ATP correctly for successful hydrolysis. A base is catalysing the hydrolysis by promoting the attacking water. There are strong indications that the catalytic glutamate of the Walker B motif fulfils the task of the catalytic base.[33] It is highly conserved and points towards the γ-phosphate of ATP. In addition, several studies showed that mutation of this residue leads to a significant reduction or even complete loss of ATPase activity.[34] Other possible bases for the polarisation of the attacking water are a conserved glutamine residue in the Q-loop[35] and the histidine residue in the H-switch[36]. There is additional disagreement over the question, whether the phosphoryl transfer happens through an associative (S_N2-like) or a dissociative (S_N1-like) transition state. While various results from kinases other than ABC transporters could suggest either an S_N1-like[37], or an S_N2-like[38] transition state, this question remains, as many aspects of the precise mechanism of ATP hydrolysis, unanswered.[32]

But why does the binding of ATP lead to the dimerization of the NBDs, while ATP hydrolysis induces dissociation of the dimer? From an energetic point of view, ATP-Mg^{2+} bound to the NBS represents a low-energy state, and simulations on the ABC transporter ABCB1 showed that it has a strong stabilizing effect of approximately 42 $kJ \cdot mol^{-1}$ on the NBD dimer.[39] On the other hand, the hydrolysis product ADP-Mg^{2+} and inorganic phosphate (P_i) represent a high-energy state that will induce the separation of the dimer. The hydrolysis of ATP to ADP and the release of P_i thus weakens the interaction between the NBDs, disrupts the dimer interface and induces the (re-) opening of the NBDs, until exchange of ADP for new ATP again induces dimerization.

This cyclic change of the NBD dimerization from the open to the closed conformation is transduced to the TMDs through coupling helices at the interface between NBDs and TMDs.[40,41] The structure of these coupling helices is conserved between different TMD folds, although the exact position of the coupling helices in relation to the transmembrane helices may vary.[31] The coupling helices form a ball-and-socket joint[42,43] with a grove in the NBD that is located at the γ-phosphate-sensitive interface between the RecA-like core and the ABCα subdomain[23]. Thus, absence and presence of the γ-phosphate lead to a rearrangement of the TMDs from an inward-facing (IF) to an outward-facing (OF) conformation. This conformational change between the IF and OF conformations is key for the function of ABC transporters, as it enables an alternating access to the translocation pathway from the two sides of the membrane. For ABC importers, this means that substrate uptake takes place in the OF conformation, while the substrate is released in the IF conformation. For ABC exporters, the substrate binds to the transporter in the IF conformation and dissociates in the OF conformation on the other side of the membrane.

1.2.3 Asymmetric nucleotide binding sites

A distinct feature of many ABC transporters is the presence of asymmetry with respect to their ATPase sites. This is often the case for ABC systems that exist as a fused hybrid in form of a heterodimeric complex (see chapter 1.2.1), or as a full-length transporter with nonidentical NBDs. However, even homodimeric ABC transporters could employ an asymmetric mechanism, as was found for the homodimeric ABC transporter MsbA.[44]

In those transporters with nonidentical NBDs, one NBS is referred to as the consensus NBS (c-NBS) and contains all the conserved motifs mentioned above. The other NBS is termed the degenerate NBS (d-NBS) since it deviates from the consensus sequence. Precisely, these deviations center around the substitution of the catalytically important glutamate in the Walker B motif for an aspartate residue, while substitutions in the H-switch and the signature motif have also been documented.[45] These substitutions cause the d-NBS to be catalytically inactive or to have a significantly reduced ATPase activity, hence a degenerate NBS cannot sustain substrate transport on its own.[46] Based on analysis of interactions, it was suggested that ATP hydrolysis is blocked or reduced at the d-NBS as a result of the increased distance of the degenerate Walker B aspartate to the γ-phosphate of ATP.[47] However, replacing the aspartate in the degenerate site with a glutamate could not increase the ATPase activity in the heterodimeric ABC transporter TmrAB[48], indicating that the

catalytic asymmetry is rather imprinted onto the whole d-NBS and does not rely on one single noncanonical residue.

The presence of such catalytic asymmetry is a general blueprint among many ABC exporters, and an asymmetric response may be relevant for their functionality.[49] The sequence of the degenerate NBS has been evolutionarily conserved, suggesting that the catalytic asymmetry might be associated with a new function. It is widely acknowledged that a degenerate NBS could result in significant differences in the mechanistic details.[50,51] It was suggested that catalytic asymmetry could lead to a division of labor between the two NBSs, with the c-NBS energizing the transport cycle by ATP hydrolysis, and the d-NBS fulfilling another task. The d-NBS could, for example, act as an ATP sensor, although this task could also be done by a c-NBS.[52] Apart from this hypothesis, there is structural and biochemical evidence from various ABC systems, indicating that the c-NBS undergoes several cycles of ATP hydrolysis, while the d-NBS remains closed and ATP-bound.[53,54] The d-NBS could hence function as a molecular glue or hinge that keeps the NBDs in closer contact for more than one transport cycle, and allosterically regulate the c-NBS.[55] These hypotheses are, however, still under debate and the functional relevance of asymmetric NBSs remains elusive.[49]

1.2.4 Classification of ABC transporters

ABC transporters exhibit an impressive structural and functional diversity, with different transporters shuttling very distinct substrates, and some transporters specialize in cargo import, others in export, and others take on important regulatory tasks apart from substrate transport. The large number of systems in the ABC superfamily necessitates their classification based on shared characteristic features. Older systems of classification grouped transporters based on their function.[56] In recent years, however, a growing number of transporters did not fit into their designated ABC classes. The Cystic fibrosis transmembrane conductance regulator (CFTR), for example, was classified as a type I ABC exporter (of the outdated nomenclature), but as a gated chlorine channel has no exporting function.[57] Since the NBD region of ABC transporters is evolutionary highly conserved and only the TMD region shows a large structural diversity, a new system of nomenclature was established in the last years that focuses on the comparison of TMD folds of ABC transporters.[58]

Based on this classification, ABC transporters can be grouped into seven distinct types. All these types can be found in bacteria. The seven different folds of ABC systems fulfil different physiological functions[23]: ABC transporters of types I–III are

importers, while types IV and V transporters function mainly as exporters. Type VI transporters are extractors, while type VII transporters work as tripartite efflux pumps. These seven types are illustrated in **Figure 1.3** and the structural features of their TMD folds as well as their mechanistic details, if known, will be shortly introduced in the following paragraphs.

Type I transporters, such as the maltose importer $MalFGK_2$ from *Escherichia coli* (*E.coli*)[59] (**Figure 1.3a**) are commonly responsible for the uptake of metabolites (e.g., sugars, amino acids, and peptides).[60] They require a substrate-binding protein (SBP) or a soluble substrate-binding domain (SBD) that delivers the substrate to its TMDs.[61] The substrate-loaded SBP docks with its lobes onto the TMDs of the importer in the IF conformation. This enables the ATP-induced dimerization of the NBDs and the conformational change of the TMDs from the IF to the OF state. The rearrangement of the TMDs opens the lobes of the bound SBP that now releases the substrate into the translocation pathway, where it specifically binds to a binding site. ATP hydrolysis induces the conformational change to the IF state, and the substrate is released on the other side of the membrane.[62]

Type II transporters, as represented by the vitamin B_{12} importer $BtuC_2D_2$ from *E.coli*[63] (**Figure 1.3b**), function similarly to type I transporters. They typically import micronutrients, such as vitamin B_{12} (cobalamin), metal chelates, and heme.[60] They also require substrate delivery by SBPs. However, type II importers exhibit a higher basal ATPase activity and ATP-induced dimerization of the NBDs can occur without the necessity for bound SBP. The substrate-loaded SBP binds to the transporter in the OF conformation and releases the substrate, where the high hydrophobicity of the translocation pathway does not allow for substrate binding.[64] ATP hydrolysis again leads to substrate release and dissociation of the SBP, and the transporter enters into a collapsed state until the next transport cycle is initiated by ATP binding.[65]

Type III transporters shuttle vitamins, as well as tryptophane and certain metal cations across the membrane.[66] An example for a type III importer is the folate-specific energy-coupling factor (ECF) importer from *Levilactobacillus brevis*[67] (**Figure 1.3c**). Their architecture differs from other types of ABC transporters. Instead of two structurally and functionally related TMDs, type III importers have one transmembrane component (EcfT subunit) and one membrane-embedded substrate-binding protein (EcfS), where the transporter core of the transmembrane component and two NBDs, EcfAA'T, can interact with more than one EcfS subunit.[64] Due to this particular structure, their transport mechanism, although not yet conclusively clarified, differs from other importers. ATP-induced dimerization of the NBDs results in a rearrangement of EcfT, which can now accommodate EcfS. This binding restores the binding cavity of EcfS, enables substrate binding and could lead to the dissociation

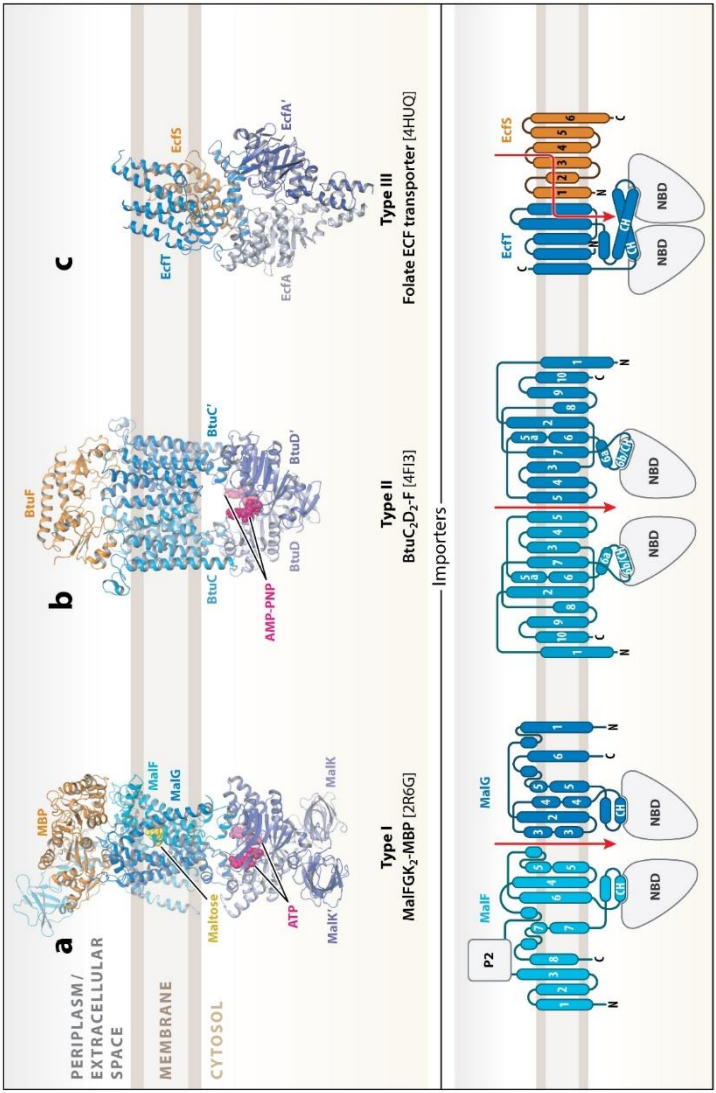
a
b
c
PERIPLASM/
EXTRACELLULAR
SPACE
MEMBRANE
CYTOSOL
MBP
MalF
MalG
Maltose
ATP
MalK'
MalK
BtuF
BtuC'
BtuC
AMP-PNP
BtuD'
BtuD
EcfT
EcfS
EcfA'
EcfA
Type I
MalFGK2-MBP [2R6G]
Type II
BtuC2D2-F [4FI3]
Type III
Folate ECF transporter [4HUQ]
Importers
P2
MalF
MalG
NBD
NBD
EcfT
EcfS
NBD
NBD

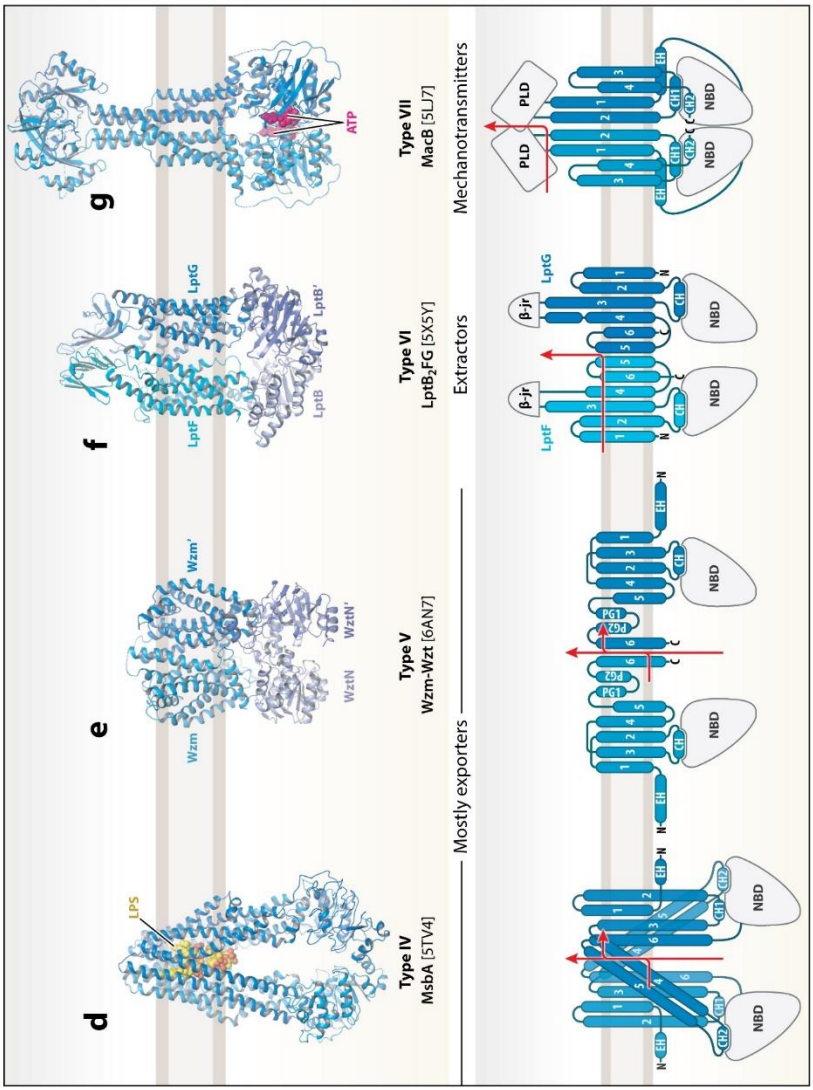

(Figure caption overleaf)

[p. 10-11] Figure 1.3. Overview of the different ABC transport systems. Illustrated by representative structures and their corresponding TMD topology. The primary direction of substrate transport is shown with red arrows. (a) Crystal structure of a type I ABC transporter, the maltose importer $MalFGK_2$ from *E. coli* (PDB code 2R6G). (b) Crystal structure of a type II ABC transporter, the vitamin B12 importer $BtuC_2D_2$ from *E. coli* (PDB code 4FI3). (c) Crystal structure of a type III ABC transporter, the folate-specific energy-coupling factor (ECF) importer from *Levilactobacillus brevis* (PDB code 4HUQ). (d) Cryo–electron microscopy reconstruction of a type IV ABC transporter, the LPS translocase MsbA from *E. coli* (PDB code 5TV4). (e) Crystal structure of a type V ABC transporter, the channel-forming O-antigen-flipping Wzm-Wzt from *Aquifex aeolicus* (PDB code 6IOH). (f) Crystal structure of a type VI ABC transporter, the LPS-extracting transporter $LptB_2FG$ from *Pseudomonas aeruginosa* (PDB code 5X5Y). (g) X-ray structure of the type VII ABC transporter MacB from *Aggregatibacter actinomycetemcomitans* (PDB code 5LJ7). Figure adapted and modified from[23].

of substrate-loaded EcfS. One mechanism, the thermal ratchet model, suggests that ATP hydrolysis and phosphate release once again trigger interaction of EcfAA'T with EcfS, which results in EcfS toppling over and the release of the substrate into the cytosol.[68] The power stroke model, on the other hand, proposes that EcfS can bind to the ATP-bound EcfAA'T complex. Subsequent ATP hydrolysis and phosphate release then induce the toppling over of EcfS and lead to substrate release.[69]

The diverse group of type IV transporters is represented by the lipopolysaccharide (LPS) flippase MsbA from *E. coli*[70] (**Figure 1.3d**). We often find multidrug efflux transporters – exporters – with a broad range of substrates among type IV transporters.[71] Their TMD architecture is characterized by a so-called elbow helix at the N-terminal end that interacts with the membrane and stabilizes the transporter.[72] The transmembrane helices reach far into the cytoplasm, the NBD-membrane distance is larger than in other types of ABC transporters. In addition, two types of coupling helices are found: coupling helix 1 (CH1) interacts with the NBD of the same half-transporter in the IF conformation, and with both NBDs in the OF conformation. Structural studies showed that CH1, as was explained in chapter 1.2.2, interacts with that region of the NBD that is responsible for ATP binding.[72] The coupling helix 2 (CH2) only interacts with the NBD of the opposite half-transporter in a domain swapped arrangement. It is fascinating how evolutionary changes could accommodate a different directionality of transport in ABC transporters. Here, the exporting mechanism differs from importers, while still relying on the same processes at the NBDs. In the absence of ATP, the transporter exists in an IF conformation, with the TMDs forming an open cytosolic gate that grants access to the translocation pathway from the cytoplasm, while the periplasmic gate (prokaryotes) or extracellular gate (eukaryotes) is closed and the translocation pathway towards the extracellular space

is collapsed.[18] In this IF conformation, substrate can enter and bind at the inner cavity of the transporter. Binding of ATP again induces dimerization of the NBDs, which is coupled to the rearrangements of the TMDs to the OF conformation. The cytosolic gate closes, and the periplasmic gate or extracellular gate opens.[23] The substrate has a reduced affinity for the binding site in the OF conformation and dissociates out of the cavity. It is generally accepted that ATP binding is the power stroke that provides the mechanochemical energy to enable this conformational transition.[73] ATP hydrolysis and phosphate release induces dissociation of the NBDs and the return of the transporter to the IF conformation. This hydrolysis-powered return, as was mentioned before, remains to be fully understood.

Type V transporters, such as the O-antigen translocator Wzm-Wzt from *Aquifex aeolicus*[74] (**Figure 1.3e**), include various channel-forming biopolymer secretion systems in prokaryotes on the one hand, and importers such as the retinal importer ABCA4 in eukaryotes on the other hand.[75] In contrast to type IV transporters, the TMDs of type V transporters do not adopt a domain swapped arrangement. Therefore, conformational changes of one NBD are only directly coupled to the TMD of the same half-transporter, not to both. The mechanistic or functional implications of this distinction are, however, not well understood.[76] As a result of their functional diversity, the mechanistic details vary considerably between members of this subgroup, with some relying on an alternating-access type of translocation[77], while others employ different mechanisms. In Wzm-Wzt, for instance, several rounds of ATP binding and hydrolysis are likely necessary to transport the polysaccharide substrate through the inner membrane of gram-negative bacteria, where it serves as an important building block of mature LPS (which, itself, was translocated through the inner membrane by the flippase MsbA).[78]

In addition, the LPS-extracting transporter $LptB_2FG$[79] (**Figure 1.3f**) as type VI transporter is involved in the transport of mature LPS to its destination, the extracellular leaflet of the outer membrane.[80] It consists of the ABC transporter itself and four additional subunits, LptA, LptC, LptD and LptE. While two homodimers of LptB constitute the NBDs, the TMDs are formed by LptF and LptG with distinct folds and additional periplasmic β-jellyrolls that are necessary for LPS transport.[79] Flipped and mature LPS laterally enters the translocation cavity. ATP-induced NBD dimerization and TMD rearrangement leads to the collapse of the translocation cavity, ejecting the LPS into the periplasmic β-jellyroll complex.[81] LPS is subsequently pushed into and along the transperiplasmic LptA filament and reaches the LptD–LptE complex in the outer membrane, where it is inserted into the extracellular leaflet.[80]

The group of type VII transporters is exemplified by MacB from *Aggregatibacter actinomycetemcomitans*[82] (**Figure 1.3g**). It is part of the MacAB-TolC pump that

extrudes macrolide antibiotics and virulence factors out of the cell.[83] MacB has large periplasmic domains (PLDs) attached to their TMDs, where MacB interacts with the hexameric MacA. MacA constitutes, together with the trimeric TolC, the transperiplasmic channel.[82] Notably, even in the open NBD conformation in absence of ATP, the MacB dimer leaves no space for substrate to enter. Instead, it is suggested that substrate enters laterally through an opening at the periplasmic side of the membrane. Its translocation mechanism differs from other transporters, and ATP binding and hydrolysis does not power an alternating access, but rather a cycle of compression and expansion that pushes the substrate through the channel.[84]

1.2.5 Human ABC transporters

While in prokaryotes, all seven types of ABC transporters can be found, only types IV and V exist in higher eukaryotic cells. In humans, 48 ABC transporter genes are present.[85] Based on the structure of the TMDs, sequence homology and the presence of accessory domains, they are classified into seven distinct subfamilies, ABCA-G.[86] The subfamilies ABC-E and ABC-F contain proteins without TMDs that are not involved in transport processes, but instead in the biogenesis and recycling of ribosomes.[87,88] The subfamilies ABC-B, ABC-C and ABC-D are type IV transporters, while the subfamilies ABC-A and ABC-G are type V transporters. As such, their structural and mechanistic details have been outlined in chapter 1.2.4. The majority of human ABC transporters are exporters, but there are noteworthy exceptions. The beforementioned CFTR (categorized nomenclature ABCC7) is a gated chloride channel, while the also mentioned retinal-phosphatidylethanolamine flippase ABCA4 functions as an importer. Furthermore, the vitamin B_{12} transporter PXMP1L (categorized nomenclature ABCD4) is a lysosomal importer[89], and the sulfonylurea receptor subunits SUR1 and SUR2 are the regulatory element in ATP-sensitive potassium (K_{ATP}) channels[90]. Notably, catalytic asymmetry is a widespread feature among human ABC systems, with more than half of the 48 transporters from all subfamilies except ABCD having nonidentical NBDs. In full-length transporters, the d-NBS is always NBS1, the c-NBS is NBS2.[91]

The exporters among the human ABC transporters are found in almost all organs and tissues, and within the plasma membrane as well as most intracellular membranes.[86] They are involved in a variety of cellular tasks, such as lipid, peptide, and metabolite trafficking, peroxisomal transport, and the general excretion of a broad range of dietary cytotoxins, fungal and bacterial toxins – as well as therapeutic drugs.[92] As a result, they are often associated with MDR in cancer cells (s. chapter 1.2).

But ABC exporters also play an important role in the immune response of humans and other vertebrates. If the innate immune system, which is programmed to react unspecifically to broader categories of pathogens, fails at eliminating a pathogenic threat to its organism, the highly specific adaptive immune system is activated just days after the infection.[93] One of its major pathways is the cell-mediated immune response, where cytotoxic $CD8^+$ T cells recognize specific pathogenic antigens that are loaded onto the major histocompatibility complex class I (MHC I) and eliminate infected or dysfunctional cells via apoptosis.[94] As one of the firsts steps, antigen-representing cells (APCs) are recruited that fragment ubiquitinylated proteins of pathogenic origin into antigens, short peptides with a length of 3 to 22 residues.[95] These antigens are transported from the cytosol to the lumen of the endoplasmic reticulum (ER), where they are loaded onto MHC I molecules and subsequently transported to the cell surface for representation.[96] The translocation from the cytosol to the ER is performed by the transporter associated with antigen processing (TAP), a type IV ABC transporter. It is a heterodimer formed by the two half transporters TAP1 (ABCB2) and TAP2 (ABCB3).[92] TAP can shuttle a broad range of peptides, and only the N- and C-terminal peptide ends are relevant for binding.[97] In addition, studies suggest that high ER-lumenal peptide concentrations could arrest further substrate translocation by saturating the low-affinity peptide binding site of TAP, leading to a negative feedback called trans-inhibition.[26]

TAP is an essential element of the adaptive immune response, and a deficiency of one of the TAP subunits was shown to result in an increase in infectious diseases and tumor development.[98] Furthermore, due to its importance, TAP is a prominent target of viruses in order to evade an immune response, and almost any step in the translocation cycle can be targeted. The herpes simplex virus (HSV), for instance, encodes for the infected cell protein 47 (ICP-47) that inhibits TAP transport by competing for the peptide binding site.[99] Other evasion mechanisms involve TAP degradation[100], inhibition of ATP binding[101], and arresting TAP in an inactive conformation[102]. All these examples show, how the precise knowledge of the molecular mechanisms for the function of TAP are vital in the fight against serious diseases and pathogens.

1.2.6 The heterodimeric ABC exporter TmrAB

Another ABC exporter was identified in the thermophilic organism *Thermus thermophilus*, an extremophile living in hot springs in Japan with a physiological temperature of 68 °C.[48] Due to homology to other ABC transporters associated with MDR, it was named *Thermus thermophilus* multidrug resistance protein AB (TmrAB),

and it is the only known ABC exporter in *Thermus thermophilus*. It is a heterodimeric type IV transporter that is assembled from the two subunits TmrA and TmrB, where TmrA conserved the canonical walker B motif and TmrB contains a degenerate walker B motif that leads to catalytically asymmetric NBSs.[48] Interestingly, TmrAB shares structural and functional homology with TAP, and it was found that it can restore antigen processing in TAP-deficient cells.[103] Analogous to TAP, TmrAB exhibits a very broad substrate specificity. This polyspecificity includes peptides, dyes, and lipids, and is linked to the heterogeneous nature of its substrate binding cavity, with differently charged residues distributed over the cavity.[103] Furthermore, several shared residues between TmrAB and TAP could be identified that are known to be involved in substrate recognition in TAP.[103] TmrAB can be expressed in *E. coli*, with the two half transporters forming a stable complex. Because of the similarity to TAP and the accessibility of TmrAB via bacterial expression, TmrAB can serve as a model system for TAP, and research on TmrAB can serve as a vital tool for elucidating the molecular mechanism of the transport cycle of human ABC transporters with asymmetric NBSs.

A significant contribution to the investigation of ABC exporters was made with a cryogenic electron microscopy (cryo-EM) study that provided eight high-resolution structures (up to 3.5 Å) of TmrAB in different conformational stages of its transport cycle.[104] To break the pseudo-twofold symmetry and thus enhance the resolution, a high-affinity nanobody was attached to TmrB. When TmrAB was incubated with ATP-Mg^{2+} (denoted as turnover conditions, as the transporter can hydrolyze ATP) and a fluorescent peptide as substrate, several conformations were observed. First, two different IF conformations were found, IF^{narrow} and IF^{wide}, where the cytosolic gate shows a wider opening in IF^{wide}, leading to an increase in the volume of the binding cavity. This is mainly the result of a movement of transmembrane helix six (TM6) to accommodate the substrate in the cavity and suggests that TmrAB can adapt its cytosolic gate width in the IF conformation depending on substrate size. Furthermore, two new conformations were observed, the asymmetric unlocked return states UR^{asym} and UR^{asym*}. Here, the d-NBS contains ATP, while the c-NBS contains ADP and is slightly wider. While the two UR conformations were abundantly present under turnover conditions, no OF conformation was found. This could suggest that the OF conformation is more transient, whereas the UR state accumulates, because the opening of the ATP-bound d-NBS could be the rate-limiting step for the return to the IF conformation.[104] However, the bound nanobody may considerably modify the energy landscape of the conformational transitions.

These insights, together with the knowledge summarized in chapters 1.2.1 - 1.2.5, lead to the postulation of a detailed model for the substrate transport cycle in heterodimeric ABC exporters (**Figure 1.4**). TmrAB alternates between IF^{narrow} and IF^{wide}

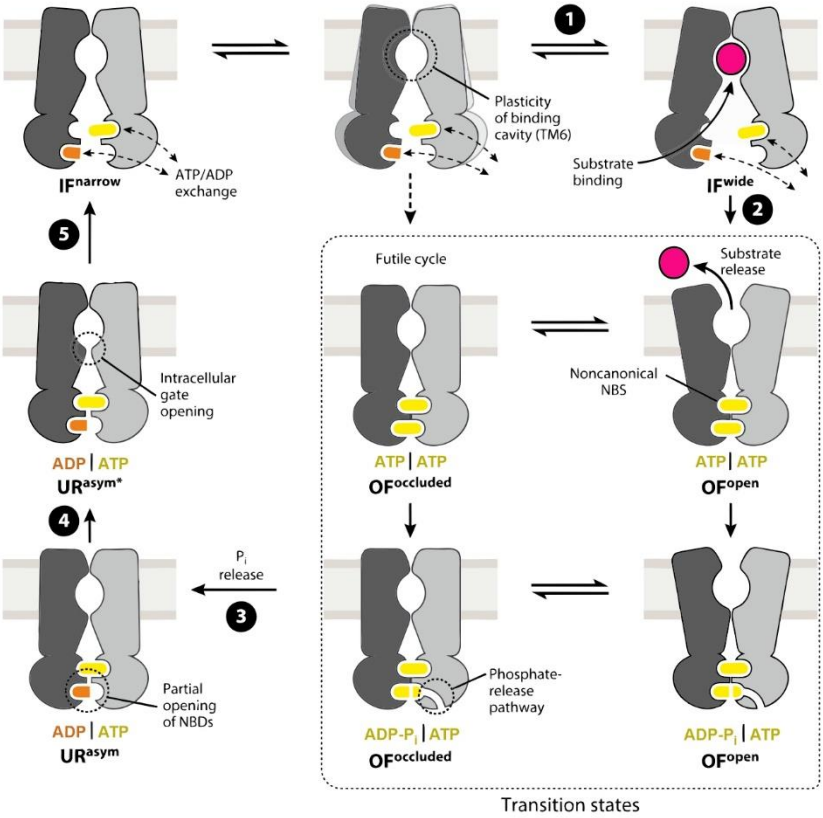

Figure 1.4. Model of the transport cycle in TmrAB. In the substrate-receptive state, the exporter adopts IF conformations with different opening angles (IF^{narrow} and IF^{wide}). Access of substrate (magenta) to the binding cavity (1). ATP (yellow) binding to both NBDs and subsequent dimerization leads to closure of the cytosolic gate and opening of the periplasmic gate (2). Following substrate release and before Pi release, the exporter can change between OF^{open} and $OF^{occluded}$ conformations. Once P_i dissociates from the canonical site via a phosphate/water channel, the transporter assumes asymmetric UR^{asym} conformations (3 and 4), which are characterized by progressively opening NBDs and cytosolic gate, to finally advance toward the IF conformation (5). NBD separation after P_i dissociation is the rate-limiting step of the cycle. ATP binding in the IF^{narrow} conformation can also directly lead to the $OF^{occluded}$ conformation. This path results in a futile cycle or translocation of only small substrates. TmrA in dark grey, TmrB in light grey (names assigned arbitrarily). Figure adapted and modified from[23].

to accommodate the substrate in its binding cavity (step 1). ATP binding to both NBDs induces dimerization, this conformational change is transmitted via the coupling helices to the TMDs, which undergo a conformational transition to the OF state with the periplasmic gate opened and the cytosolic gate closed (step 2). Subsequently, the substrate is released in the OF state and TmrAB can switch between conformations with an open (OF^{open}) and closed ($OF^{occluded}$) periplasmic gate. If no substrate is bound to the IF state of TmrAB, ATP binding at both NBDs results in a futile transport cycle, in which ATP binding and hydrolysis are not coupled to substrate transport and ATP is consumed without successful substrate translocation. ATP hydrolysis at the c-NBS and P_i dissociation weakens the NBD dimer and leads to an asymmetric conformation UR^{asym} (step 3), which finally results in a return to the IF conformation (steps 4 + 5).[104] However, it remains unclear, whether d-NBS opening is a prerequisite for the return to the IF state. In general, the discussed questions regarding the mechanistic details of ATP hydrolysis and the role of catalytic asymmetry remain open.

1.3 Investigation of ABC transporters

1.3.1 Structural & dynamic methods

Approximately 30 % of all genes encode for membrane proteins, and their localization at the cellular interface makes them lucrative targets for drug research.[105] To fully understand the function of a membrane protein, we need to understand their structural and dynamic properties. For ABC transporters, as was shown in the previous chapter, many of these aspects remain to be elucidated. However, studying ABC transporters and other membrane proteins poses unique challenges compared to soluble proteins due to their hydrophobic nature and the difficulty in isolating them from the membrane environment without disrupting their structure and function.[106] These problems become apparent, when we see that membrane proteins constitute only a few percent of the structures in the Protein Data Bank.[107] Significant advancements in biochemical, biophysical, and structural techniques have enabled researchers to focus on the investigation of membrane proteins, but these techniques all have their limitations. A selected number of important techniques is shortly introduced in the following paragraphs.

X-ray crystallography is an important technique used to determine the 3D structure of membrane proteins in high resolution.[108] For this, a highly concentrated, purified sample is crystallized. These crystals are subjected to X-ray radiation, and the resulting diffraction pattern is analyzed to yield an electron density map, from which a highly resolved protein structure can be inferred.[109] Due to the process of

crystallization, it is difficult to obtain dynamic information from X-ray crystallography of most membrane proteins. In addition, it is difficult to crystallize membrane proteins, since they have to be solubilized in detergent and have a high hydrophobicity.[110] This gives rise to more challenges for X-ray crystallography for studying membrane proteins.[111]

Nuclear magnetic resonance (NMR) spectroscopy, on the other hand, is used to obtain both structural and dynamic information of a broad range of membrane proteins in a non-crystal environment.[112] It is a non-invasive method, and the highly resolved 3D structure of proteins can be measured in solution, which can be employed to study intramolecular interactions, as well.[113] However, the analysis of large systems is difficult, limiting the application of NMR spectroscopy to biomolecules with a molecular weight of approximately 50 kDa.[114] Solid state NMR (ssNMR) can circumvent the limitation of molecular weight and thus make large biomolecules accessible for structure determination. To obtain well-resolved spectra, anisotropic contributions need to be removed, which is very often achieved by physically spinning the sample around an axis that is tilted by 54.7° from the static magnetic field – so-called magic-angle spinning (MAS).[115] Further, to obtain high spectral sensitivity, the biomolecules may need to be isotopically labelled to detect e.g. ^{13}C NMR signals.[115] Broad lines are to be expected, and sensitivity enhancements from dynamic nuclear polarization (DNP), and thus sample temperatures of around 30 K are required.[116] Nevertheless, this ss-NMR setup was employed to gain structural insights on ABS transporters such as MsbA[117] and BmrA[118].

There are various important applications of microscopy techniques for structure determination. Cryo-EM is one such powerful technique that has been used in recent years to investigate the structure of membrane proteins. Due to technical developments in instrumentation and sample preparation, this technique is rapidly advancing, and the number of yearly deposited structures using cryo-EM has already outperformed NMR, with X-ray crystallography soon to follow.[119] A vitrified sample is imaged by transmission electron microscopy (TEM) in two-dimensional space, and with the help of advanced computational methods high resolution three-dimensional reconstructions are obtained.[120] However, analyzing small proteins is challenging due to low resolution.[121] In addition, the requirements for sample quality are still relatively high, limiting the flexibility in sample preparation and, thus, in investigating the structural dynamics of membrane proteins.[122]

Förster resonance energy transfer (FRET) is a mechanism that describes the energy transfer between two fluorescent molecules, known as donor and acceptor, when they are in close proximity.[123] In the context of membrane protein research, techniques involving a FRET pair allow to probe protein-protein interactions, protein

conformational changes, and protein-lipid interactions.[124] By labelling specific regions of a membrane protein with fluorescent dyes, FRET can provide insights into the dynamic rearrangements and structural changes that occur upon ligand binding, protein activation, or protein-protein interactions.[125] FRET is a suitable technique to monitor the conformational changes for membrane protein systems, even in a single molecule approach and at physiological temperatures. However, this technique may cause high structural perturbation due to the requirement of relatively large probe sizes and may compromise the identification of conformational states and their changes.[126] In addition, labelling a biomolecule with different dyes is challenging.

1.3.2 Investigation using EPR spectroscopy

Electron paramagnetic resonance (EPR) spectroscopy is a powerful biophysical technique that evades or minimizes many of the above limitations and provides structural as well as dynamic information about membrane proteins. Dipolar EPR spectroscopy in particular yields, due to the use of significantly smaller probe sizes and the requirement of only one type of spin label, more reliable distance distributions with significantly less effort in labelling and data analysis, in comparison to FRET measurements.[127] EPR is valuable for the structural characterization of macromolecules, especially where diffraction and NMR approaches fail due to structural disorder, size, or high complexity of the system.[128] Without a demanding sample preparation necessary, and with its high sensitivity and non-destructive application, pulsed EPR spectroscopy is an ideal method to investigate the otherwise already demanding families of membrane proteins and ABC transporters.[129]

In recent years, pulsed EPR spectroscopy has become a widely used technique in the repertoire of methods to investigate membrane proteins by determining distance distributions between intrinsic or artificially introduced spin centers within macromolecules. With such data, structural models can be validated in various environments, conformational flexibility of macromolecules can be detected, or macromolecular complexes can be reconstructed from their components.[130]

As a structural biology tool, it can be employed to study the secondary, tertiary, and quaternary structures of biomolecules, as well as follow their conformational changes.[131] Apart from that, it can also be used to determine the relative orientations between interacting spin labels and the connected structures.[132] While nitroxide spin label based pulsed EPR experiments are the most widely used application, a continuously increasing number of available spin labels provides new possibilities for structural studies.[133]

Despite the wide application of pulse EPR techniques in structure biology, it is essential to study structure and function of membrane proteins in their native environment. Excellent work has been done in recent years and preparations for the reconstitution of membrane proteins have been optimized in the presence of unlabeled proteins, liposomes and nanodsics. Apart from that, several promising approaches for in-cell applications have emerged. Biomolecules can be labelled *in vitro* and subsequently delivered to the target in the cells, for example by microinjection[134], or measured with the use of a tailored spin labelled nanobody that is delivered via microinjections[135]. Target molecules can also be directly labelled in cells[136], or synthesized using genetically encoded paramagnetic labels[137]. Especially for the investigation of outer *E. coli* cell membrane proteins, remarkable work was done to unravel both structure and mechanistic details, as demonstrated for the cobalamin transporter BtuB[138] and the β-barrel assembly machinery (BAM) complex[139]. However, all these applications hold their challenges and limitations, and pulse EPR experiments on detergent-solubilized membrane proteins give us important information about both structure and function.

1.3.3 Kinetic information on ABC transporters

Apart from structural elucidation, understanding the function of ABC transporters requires information about their dynamic properties. Using biochemical assays, researchers can investigate and quantify the hydrolysis of ATP[140], the binding of SBPs[141], the transport of substrates[142], or the effect of inhibition[143], while the role of key amino acid residues can be studied with the help of specific mutations[144]. In addition, for ligand-gated ion channels (including CFTR, an exception among ABC transporters), single-channel recording methods, such as the patch clamp technique, are available.[145]

The direct kinetic investigation of conformational transitions in ABC transporters, however, poses an especially challenging endeavor because most of the techniques discussed in chapter 1.3.1 that allow for the structural elucidation of a system can only provide limited or no time resolution. As a result, until now, only few studies focused on the kinetic aspects of conformational changes in ABC transporters. Nevertheless, technical advances provide new tools to approach these challenges.

Time-resolved ssNMR (TR-ssNMR) is based on ssNMR. However, by quickly initiating the desired reaction (such as a conformational transition) followed by very fast freezing, a series of structural snapshots is obtained with a time resolution depending on the speed of sample freezing. To investigate conformational changes in proteins, a rapid freeze-quench (RFQ) approach was developed that can freeze

samples in 100 µs, and thus provides a time resolution in the milliseconds range.[146] Biomolecular processes, such as the complex formation between the calcium regulator calmodulin and a peptide substrate were studied and yielded quantitative kinetic information on the observed structural rearrangements that helped elucidate the complex formation pathway.[147,148] So far, TR-ssNMR was not applied to large systems such as ABC transporters.

Time-resolved Fourier transform infrared spectroscopy (TR-FTIR) can be employed to indirectly investigate and quantify conformational change. In a study, the dimerization kinetics of the soluble NBDs from MsbA were investigated after photoinduced release of caged ATP. It revealed two apparent rate constants, 1 s^{-1} and 0.01 s^{-1}, which were assigned to dimer formation and hydrolysis, suggesting that ATP hydrolysis has to be the rate-limiting step in the transport cycle.[149] Recently, TR-FTIR was used to follow the conformational changes during ATP binding and hydrolysis in full-length MsbA and yielded comparable rate constants.[150]

Another method to investigate ultrafast dynamics of proteins, even down to sub-picosecond time scales, is time-resolved X-ray solution scattering (TR-XSS).[151] Here, in contrast to X-ray crystallography, not the diffraction pattern of a crystal is measured, but the time evolution of X-ray scattering by a biomolecule solution is monitored. Conformational changes lead to changes in the scattering pattern. For this, the reaction needs to be triggered faster than the timescale of the conformational change itself. One popular trigger method is stopped-flow mixing, where the conformational change is induced by quick mixing of the biomolecule and a ligand, with time resolution in the milliseconds or even microseconds range possible. The combination of a stopped-flow mixing setup with small-angle X-ray scattering (SF-TR-SAXS), where the small-angle region of the scattering pattern is analyzed, was used to investigate the kinetics and accompanying structural changes of ATP-induced NBD dimerization and subsequent hydrolysis-induced dissociation in full-length MsbA in lipid nanodiscs. The dimer species increased over a period of 1 second, persisting up to 10 seconds, and decayed slowly over 120 s, resulting in rate constants for dimer formation and dissociation of 2 s^{-1} and 0.02 s^{-1}, respectively.[152] A second trigger method is the photoinduced release of caged ATP, with a possible time resolution up to picoseconds. Using this photocage-initiated TR-XXS approach, similar observations were made, where dimer formation proceeds over 1.5 seconds and comparable rate constant for the dimer formation were obtained.[153]

Single-molecule FRET (smFRET) provides direct information on the rate and lifetime for the conformational states in a single-molecule detection and thus without ensemble averaging.[154] It has been used to investigate several ABC transporters. In one of these studies, a smFRET approach was used to calculate the rate constants for

the SBD closure and opening in the type I ABC transporter GlnPQ.[155] Several smFRET studies, either on the antibacterial peptide exporter McjD or on $BtuC_2D_2$, localized the conformational changes within one molecule in the timescale of seconds to tens of seconds.[156–158] In another study on the multidrug resistance protein 1 (MRP1), the OF state was shown to have a lifetime of more than 20 s.[159] Furthermore, a study on MsbA investigated the conformational dynamics at the NBDs and TMDs by smFRET, and the rate constant for the conformational cycle in presence of ATP was found to be <0.25 s^{-1}.[160]

Also, FRET self-quenching of a fluorescent probe can be employed to detect NBD dimerization. In a study, a tryptophane strategically located at the center of the dimer interface was used as a dimerization probe in the prototypical NBD MJ0796.[161] The kinetics were quantified, indicating that dimer formation takes minutes.

As an ensemble technique, pulsed EPR spectroscopy can unravel the entire conformational space occupied by the molecules within a sample. Analogously to ssNMR, pulsed EPR techniques can be combined with a time-resolved sample preparation setup to follow a conformational transition over time. To observe fast processes in the milliseconds timescale, a RFQ-EPR setup was devised.[162] With this setup, the refolding of the integral membrane protein light-harvesting complex II (LHC II) was monitored in a time-resolved manner, leading to new insights into the sequence of events during assembly.[163] In another study, the isolated carboxy-terminal cyclic-nucleotide binding domain (CNBD) of the HCN2 ion channel was investigated upon binding of 3',5'-cyclic adenosine monophosphate (cAMP) using microfluidic rapid freeze quench (μRFQ) in combination with pulsed electron–electron double resonance (PELDOR) spectroscopy to obtain the rate and equilibrium constants of the conformational change.[164] Recently, a time-resolved PELDOR approach using microsecond freeze-hyperquenching (MHQ) was employed to quantitatively determine the conformational kinetics of an isolated cyclic nucleotide-binding domain (CNBD) of the potassium channel MloK1.[165] While time-resolved pulsed EPR methods have not yet been applied to complex biological systems like full length membrane proteins, they hold great promise for the quantitative kinetic investigation of ABC transporters.

1.4 Electron paramagnetic resonance spectroscopy

On the following pages, EPR spectroscopy is introduced as the method to determine structural and dynamic, and as a result functional information in this work. Although in a condensed form, the next subchapters will serve to explain the necessary concepts and techniques to understand the results and their interpretation. The theoretical background was adapted from comprehensive textbooks.[166–168]

1.4.1 The electron spin

Electrons possess, apart from an orbital angular momentum, an intrinsic angular momentum $\boldsymbol{S}$, the so-called spin. Unlike in classical mechanics, this angular momentum should not be understood as a rotation of the electron around its own axis. The electron spin is rather a quantum mechanical angular momentum without an analogue in classical physics. The magnitude of $\boldsymbol{S}$ is quantized:

$$|\boldsymbol{S}| = \sqrt{S(S+1)}\hbar \tag{1.1}$$

with the electron spin quantum number S and the reduced Planck constant $\hbar$. The component of $\boldsymbol{S}$ along one axis – conventionally labelled the z-axis and defined as the direction of an external magnetic field $\boldsymbol{B}_0$ - is given by the spin projection quantum number m_S in units of $\hbar$. It can take values ranging from $-S$ to $+S$ in integer increments, resulting in $2s+1$ values for m_S. For an electron, S has the value $1/2$, and m_S can thus have the values $\pm 1/2$, with the $m_S = +1/2$ state denoted as α-spin state and the $m_S = -1/2$ state denoted as β-spin state. Like in the classical view, this intrinsic angular momentum gives rise to a magnetic moment

$$\boldsymbol{\mu}_S = -g_e \beta_e \boldsymbol{S} \tag{1.2}$$

with the Bohr magneton β_e, and the g factor of the free electron g_e as a correction factor to account for deviations between the classical mechanical behavior of a charged particle and the quantum mechanical behavior. Again, the component of $\boldsymbol{\mu}_S$ along the z-axis, μ_z, can be related to the spin projection quantum number m_S

$$\mu_z = -g_e \beta_e m_S \tag{1.3}$$

and results in two opposing magnetic dipole moments. In the absence of an external magnetic field $\boldsymbol{B}_0$, the two spin states are energetically degenerate. Since two paired electrons in the same orbital cannot have the same spin quantum number m_S, one must have the spin projection number $+1/2$ and the other $-1/2$, and their opposing magnetic moments cancel each other. In a system with one or more unpaired

electrons however, the magnetic moment persists, and such a system is called paramagnetic.

1.4.2 Static spin Hamiltonian

In a paramagnetic species that consists of an effective electron spin S and nuclei with nuclear spin I, the energy states are described by the static spin Hamiltonian $\mathcal{H}_0$. It consists of terms that describe the interaction of the electron and nuclear spins with an external magnetic field $\boldsymbol{B}_0$, as well as coupling interactions between different spins. For our considerations, the most relevant terms are:

$$\mathcal{H}_0 = \mathcal{H}_{EZ} + \mathcal{H}_{ZFS} + \mathcal{H}_{HF} + \mathcal{H}_{NZ} + \mathcal{H}_{NQ} \tag{1.4}$$

The terms in eq 1.4 refer to the electron Zeeman interaction $\mathcal{H}_{EZ}$, the zero-field splitting $\mathcal{H}_{ZFS}$, the hyperfine interaction $\mathcal{H}_{HF}$, the nuclear Zeeman interaction $\mathcal{H}_{NZ}$, and the nuclear quadrupole interactions $\mathcal{H}_{NQ}$. $\mathcal{H}_0$ is called the static spin Hamiltonian, because it only contains electron and nuclear spin vector operators ($\boldsymbol{S}$ and $\boldsymbol{I}$, respectively) and, in contrast to the oscillatory Hamiltonian, no time-dependent oscillatory microwave (MW) field.

1.4.2.1 Electron Zeeman interaction

The electron Zeeman (EZ) interaction describes the interaction of the magnetic moment μ_S of the electron spin, as described in chapter 1.4.1, with an external magnetic field $\boldsymbol{B}_0$, and is given by

$$\mathcal{H}_{EZ} = \beta_e \boldsymbol{B}_0 \boldsymbol{g}\, \boldsymbol{S}/\hbar \tag{1.5}$$

Often, $\mathcal{H}_{EZ}$ is the dominating term of $\mathcal{H}_0$. In a free electron with $S = 1/2$, the external magnetic field lifts the energetic degeneracy of the spin sates and results in a splitting into two energy levels that correspond to the parallel or antiparallel orientation of the spin projection to the magnetic field vector $\boldsymbol{B}_0$. The energy of the spin states is thus given by

$$E_{\alpha,\beta} = m_S \beta_e \boldsymbol{B}_0 g_e = \pm\frac{1}{2}\beta_e \boldsymbol{B}_0 g_e \tag{1.6}$$

and the energy difference follows as

$$\Delta \mathrm{E} = h\nu = \beta_e \boldsymbol{B}_0 g_e \tag{1.7}$$

and increases linearly with $\boldsymbol{B}_0$. In eq 1.5, the $\boldsymbol{g}$ tensor can be written in its principal axis system (PAS) as a diagonalized 3x3 matrix:

$$\boldsymbol{g} = \begin{bmatrix} g_x & & \\ & g_y & \\ & & g_z \end{bmatrix} \tag{1.8}$$

where g_x, g_y, and g_z are the principal values of $\boldsymbol{g}$. In the case that the magnetic field is aligned with one of the principal axes, insertion of the respective principal value into eq 1.7 gives the resonant field. For an arbitrary orientation of $\boldsymbol{B}_0$, the magnetic field vector can be expressed within the PAS with the polar angles θ and ϕ, from which the effective g value follows as

$$g_{eff} = \left[sin^2(\theta)cos^2(\phi)g_x^2 + sin^2(\theta)sin^2(\phi)g_y^2 + cos^2(\theta)g_z^2\right]^{1/2} \tag{1.9}$$

The principal values can deviate from the g_e value of the free electron spin because of spin orbit coupling (SOC) that leads to the interaction of the electronic ground state and excited states, and orbital angular momentum $\boldsymbol{L}$ is admixed from the excited sates into the ground state. Usually, this deviation is small for organic radicals.

1.4.2.2 Nuclear Zeeman interaction

In analogy to $\mathcal{H}_{EZ}$, $\mathcal{H}_{NZ}$ describes the interaction of the nuclear spin I with an external magnetic field $\boldsymbol{B}_0$, and the Hamiltonian is

$$\mathcal{H}_{NZ} = -\beta_n \boldsymbol{B}_0 g_n \boldsymbol{I}/\hbar \tag{1.10}$$

with the nuclear magneton β_n and the nuclear g factor g_n. The nuclear g_n factor is an inherent property of a nucleus and can be positive or negative. For a proton, $\mathcal{H}_{NZ}$ is only $1/658$ of $\mathcal{H}_{EZ}$, for other nuclei less. As such, the nuclear Zeeman (NZ) interaction usually has little influence on an EPR spectrum.

1.4.2.3 Hyperfine interaction

In a paramagnetic species, the unpaired electron is in close vicinity ($r < 1\,nm$) to nuclei, whose nuclear spins induce an additional magnetic field apart from the external one. The hyperfine (HF) interaction describes this coupling of the electron and nuclear spins and is an important source of information for various EPR experiments to gain insight into the ligand sphere of paramagnetic centers. For a system with an unpaired electron with the electron spin $\boldsymbol{S}$ and m nuclei with the nuclear spins $\boldsymbol{I}_k$, the hyperfine interaction is described by the term

$$\mathcal{H}_{HF} = \sum_{k=1}^{m} \boldsymbol{S}\boldsymbol{A}_k\boldsymbol{I}_k \tag{1.11}$$

where $\boldsymbol{A}_k$ is the hyperfine tensor and can be written in its PAS with its three principal values A_x, A_y and A_z:

$$\boldsymbol{A} = \begin{bmatrix} A_x & & \\ & A_y & \\ & & A_z \end{bmatrix} \tag{1.12}$$

The hyperfine interaction can be separated into the isotropic or Fermi contact interaction $\mathcal{H}_{FC}$ and the anisotropic electron-nuclear dipole-dipole coupling $\mathcal{H}_{DD}$. The Hamiltonian for the Fermi contact interaction is

$$\mathcal{H}_{FC} = \mathrm{a}_{iso}\boldsymbol{S}\boldsymbol{I} \tag{1.13}$$

with the hyperfine coupling constant a_{iso}:

$$\mathrm{a}_{iso} = \left(\frac{2}{3}\right)\frac{\mu_0}{\hbar} g_e\beta_e g_n\beta_n |\psi_0(0)|^2 \tag{1.14}$$

In eq 1.14, μ_0 is the permeability of vacuum, and $|\psi_0(0)|^2$ is the probability density of the unpaired electron at the nucleus. Since finite electron spin density at the nucleus is a requirement, only electron spins localized in an s orbital or an orbital with partial s character (such as sp^2 and sp^3) show Fermi contact interaction. However, spin density can also be transferred to the nucleus through spin polarization of the inner $2s$ and $3s$ orbitals, leading to Fermi contact interaction in systems with unpaired electrons in other orbitals than s. This is often the case for transition metal ions such as Mn^{2+}, Fe^{3+}, or Cr^{+}.

The electron-nuclear dipole-dipole coupling has the Hamiltonian term

$$\mathcal{H}_{DD} = \frac{\mu_0}{4\pi\hbar} g_e\beta_e g_n\beta_n \left[\frac{(3\boldsymbol{S}\boldsymbol{r})(\boldsymbol{r}\boldsymbol{I})}{r^5} - \frac{\boldsymbol{S}\boldsymbol{I}}{r^3}\right] = \boldsymbol{S}\boldsymbol{T}\boldsymbol{I} \tag{1.15}$$

with the vector $\boldsymbol{r}$ as the distance between the electron and nuclear spin and the dipolar coupling tensor $\boldsymbol{T}$. If $r \geq 0.25\,nm$, the spin densities can be assumed to be localized at single points in the so-called point dipole approximation (PDA). Within the PDA, $\boldsymbol{T}$ is a traceless and symmetric tensor with

$$\boldsymbol{T} = \frac{\mu_0}{4\pi\hbar}\frac{g_e\beta_e g_n\beta_n}{r^3}\begin{bmatrix}-1 & & \\ & -1 & \\ & & 2\end{bmatrix} = \begin{bmatrix}-T & & \\ & -T & \\ & & 2T\end{bmatrix} \tag{1.16}$$

If the $\boldsymbol{g}$ tensor is isotropic or anisotropy is small, $\boldsymbol{A}$ can be written as the sum of the isotropic and anisotropic contribution as

$$\boldsymbol{A} = \begin{bmatrix}A_\perp & & \\ & A_\perp & \\ & & A_\parallel\end{bmatrix} = a_{iso}\mathbf{1} + \boldsymbol{T} \tag{1.17}$$

where $\mathbf{1}$ is the unit matrix. This is the case for nitroxide radicals and Mn^{2+}. In the case of a spin system with fast rotational motion in solution, the anisotropic part of the hyperfine interaction is averaged, and only isotropic hyperfine interactions are detected.

1.4.2.4 Nuclear quadrupole interaction

For nuclear high spin systems ($I \geq 1$), e.g., ^{14}N or ^{55}Mn, the charge distribution of its nuclear spins is non-spherical. This deviation is described by the nuclear quadrupole moment Q. The interaction of Q with the electric field gradient (EFG) is called the nuclear quadrupole (NQ) interaction. In its principal axes representation, the Hamiltonian is given by

$$\mathcal{H}_{NQ} = \boldsymbol{I}\widetilde{\boldsymbol{P}}\boldsymbol{I} = \frac{e^2qQ}{4I(2I-1)\hbar}\left[(3I_z^2 - I(I+1)^2) + \eta\left(I_x^2 - I_y^2\right)\right] \tag{1.18}$$

with the traceless nuclear quadrupole tensor $\widetilde{\boldsymbol{P}}$, the electric field gradient parameter $e\boldsymbol{q}$, and the asymmetry parameter $\eta = (P_x - P_y)/P_z$ with $|P_z| \geq |P_y| \geq |P_x|$ and $0 \leq \eta \leq 1$. In an EPR spectrum, nuclear quadrupole interaction is visible as a shift in the allowed resonance frequencies. As small second-order effects, these shifts are difficult to observe.

1.4.2.5 Zero-field splitting

In systems with non-cubic symmetry and multiple unpaired electrons, i.e., a group spin $S > 1/2$, such as Mn^{2+} ($S = 5/2$) the $(2S+1)$-fold degeneracy of the ground state is lifted due to dipole-dipole coupling between the electron spins. As a result, line splitting can be observed even without an external magnetic field, hence the name zero-field splitting (ZFS) for this interaction. In its principal axes representation, the Hamiltonian is given by

$$\mathcal{H}_{ZFS} = \mathbf{SDS} = \mathrm{D}\left[S_z^2 - \left(\frac{1}{3}\right)S(S+1)\right] + E\left(S_x^2 - S_y^2\right) \tag{1.19}$$

with the traceless zero-field tensor **D**, the axial zero-field parameter $D = 3D_z/2$, and the rhombic zero-field parameter $E = \left(D_x - D_y\right)/2$. Thus, the degree of splitting depends on the symmetry of the spin system. For spin systems with $S > 2$ or higher, additional higher-order terms for the ZFS must be taken into account. In general, zero-field interactions lead to line broadening and an additional splitting of signals due to lifted degeneracy.

1.4.2.6 Weak coupling between electron spins

In 1.4.2.5, strongly interacting electron spins were discussed and characterized by their resulting group spin. On the other hand, weakly coupled electron spins, such as two unpaired electrons A and B on two different paramagnetic spin centers, are described by their individual spins S_A and S_B. This weak coupling between electrons can be divided into the isotropic Heisenberg exchange coupling $\mathcal{H}_{exch}$ and the anisotropic electron dipole-dipole coupling $\mathcal{H}_{dd}$. The complete Hamiltonian for such a system is thus given as the sum of the individual spin Hamiltonians for both spins according to eq 1.4 and the two coupling terms:

$$\mathcal{H}_0(S_A, S_B) = \mathcal{H}_0(S_A) + \mathcal{H}_0(S_B) + \mathcal{H}_{exch} + \mathcal{H}_{dd} \tag{1.20}$$

The term for the Heisenberg exchange coupling is given by

$$\mathcal{H}_{exch} = \boldsymbol{S}_A \boldsymbol{J} \boldsymbol{S}_B \tag{1.21}$$

with the exchange coupling tensor $\boldsymbol{J}$. Exchange coupling has to be considered when there is a significant overlap of the two spin orbitals and the unpaired electrons can be exchanged. This is observed in solids with short inter spin distances $r_{AB} < 1.5\ nm$ or strong electron delocalization. In solution, such exchange can occur in biradicals or during species collision and the resulting transient orbital overlap. Otherwise, the exchange coupling term can usually be neglected.

The electron dipole-dipole coupling can be described analogously to the electron-nuclear dipole-dipole coupling term $\mathcal{H}_{DD}$ of the hyperfine interaction (see chapter 1.4.2.3). It can be written as

$$\mathcal{H}_{dd} = \boldsymbol{S}_A \boldsymbol{D} \boldsymbol{S}_B = \frac{\mu_0}{4\pi\hbar r_{AB}^3} g_A g_B \beta_e^2 \left[\boldsymbol{S}_A \boldsymbol{S}_B - \frac{3(\boldsymbol{S}_A \boldsymbol{r}_{AB})(\boldsymbol{S}_B \boldsymbol{r}_{AB})}{r_{AB}^2}\right] \tag{1.22}$$

with the dipole-dipole coupling tensor $\boldsymbol{D}$ the g values of the two electron spins g_A and g_B, and the vector $\boldsymbol{r}_{AB}$ connecting the two electron spins, with $r_{AB} = |\boldsymbol{r}_{AB}|$. The matrix

elements of $\boldsymbol{D}$ not only depend on r_{AB}^3, but also the orientation of $\boldsymbol{r}_{AB}$. In nitroxide radicals, both electron spins are quantized along the direction of the magnetic field and the anisotropy of the $\boldsymbol{g}$ tensors can be neglected, i.e., $g_A \approx g_B \approx g_e$. Further, if the electron Zeeman interaction is much larger than the other couplings, the high-field approximation applies and $\boldsymbol{D}$ can be written in its principal axes representation

$$\boldsymbol{D} = \frac{\mu_0}{4\pi\hbar}\frac{g_A g_B \beta_e^2}{r_{AB}^3}\begin{bmatrix}-1 & & \\ & -1 & \\ & & 2\end{bmatrix} = \begin{bmatrix}-\omega_{AB} & & \\ & -\omega_{AB} & \\ & & 2\omega_{AB}\end{bmatrix} \tag{1.23}$$

where ω_{AB} is the dipolar coupling frequency. Since ω_{AB} is inversely proportional to r_{AB}^3, the distance between the electron spins can be experimentally assessed. If $r_{AB} < 2\ nm$, ω_{AB} is large enough and can be directly extracted from continuous wave (cw) EPR spectra. If the distances are larger, pulsed dipolar spectroscopy (PDS) techniques have to be employed (see chapter 1.4.5). The measurement of dipolar couplings is a powerful tool to determine the distances between paramagnetic species in biomolecules.

1.4.3 EPR measurements on biomolecules

Most biological macromolecules are diamagnetic and contain no unpaired electrons. These biological systems are therefore not directly accessible by EPR techniques, and only intrinsically paramagnetic molecules, such as metalloproteins or radicals in photosynthetic proteins, could be studied.[169,170]

However, biotechnological advances of the last decades made it possible to introduce artificial paramagnetic species into biomolecules. The most commonly employed class of spin labels are stable nitroxide (NO) radicals $R_2NO\cdot$ based on piperidine, pyrroline or pyrrolidine rings, with the (1-Oxyl-2,2,5,5-tetramethyl-3-pyrroline-3-methyl)methanethiosulfonate spin label (MTSL) being the preferred NO spin label for proteins (**Figure 1.5a**). They are reasonably resilient against both physical and chemical impacts and their small size minimizes structural perturbations. Recently, spin labels based on trityl, Gd^{3+} and Cu^{2+} are increasingly being used for EPR measurements.[171–173] The use of Mn^{2+} for the determination of interspin distances will be covered separately in chapter 1.4.7.

To incorporate spin labels into the biomolecule, the approach of site-directed spin labelling (SDSL) has become an important and widely used technique.[174] In the case of MTSL, the sulfonate functional group reacts highly specifically with the thiol functional

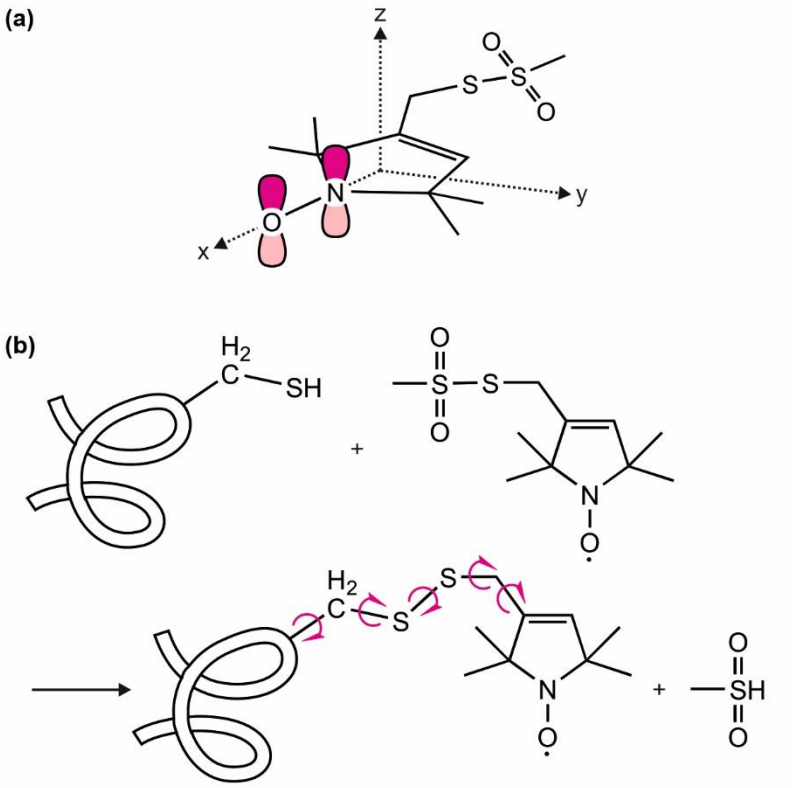

Figure 1.5. The nitroxide spin label MTSL. (a) MTSL aligned with the molecular coordinate system. (b) Side-directed spin labelling rection at the cysteine residue of a protein with MTSL. The five rotatable bonds of the resulting R1 sidechain are shown as pink arrows.

group of a cysteine residue in the protein of interest to create a disulfide-linked NO sidechain, referred to as R1 (**Figure 1.5b**). This cysteine can either be a native cysteine, or it can replace an amino acid in the protein using site-directed mutagenesis (SDM). The R1 sidechain possesses five rotatable bonds that give MTSL a high degree of flexibility and makes it an adaptable spin label for most protein sites. In addition, the free software package MMM can calculate rotamer populations for MTSL bound to proteins, if a structure exists for that protein.[175] MMM can predict experimental

observations such as NO-NO distances (see chapter 1.4.6) and helps in choosing suitable labelling positions. A too low number of rotamers indicates a protein site with low accessibility for the spin label, while a high number of rotamers signifies low steric restriction at a label site.

1.4.4 Continuous wave EPR spectroscopy

Based on the interactions and couplings described in chapter 1.4.2, the energetic eigenvalues of a paramagnetic system can be determined. A transition between two eigenstates $|k\rangle$ and $|l\rangle$ of the relevant static spin Hamiltonian $\mathcal{H}_0$ occurs, when resonant electromagnetic radiation is absorbed. In the case of an isolated free electron with the spin states α and β (see chapter 1.4.1), this switch from the $|\alpha\rangle$ to the $|\beta\rangle$ eigenstate leads to a change in the orientation towards the external magnetic field from parallel to antiparallel. In general, it is described as a transition $|m_S, m_I\rangle \leftrightarrow |m_S \pm 1, m_I\rangle$. EPR spectroscopy studies the interaction of electromagnetic radiation with matter and can provide crucial information on various aspects of its constitution, as the surroundings of a paramagnetic center affect these transitions and thus the absorption of photons.

One fundamental EPR technique is continuous wave (cw) EPR spectroscopy. In cw EPR, spectra are recorded by subjecting a sample to MW irradiation of constant frequency ν. The external magnetic field $\boldsymbol{B}_0$ is then swept until fulfilment of the resonance condition leads to absorption of irradiation. Experimentally, the sample is introduced into a resonator, in which the MW field is built up. The resonator is critically coupled, resulting in full absorption of the incident power by the resonator. By absorbing additional MW irradiation during resonance, the resonator is detuned and MW power is reflected. This reflected MW power as a function of the magnetic field is recorded as the cw EPR spectrum. In addition, the magnetic field amplitude is modulated (with a frequency of typically 100 kHz for nitroxides). Via phase-sensitive detection, only output signals with the same modulation are detected, suppressing unmodulated signals arising from noise and thereby increasing the signa-to-noise (s/n) ratio. This detection method is responsible for the derivative shape of cw EPR spectra. The excitation bandwidth of the MW irradiation is small ($\approx 2\ MHz$), and irradiation is of low power ($\approx 0.2\ W$ at X-band frequencies of 9-10 GHz).

1.4.4.1 Nitroxide cw EPR spectra

A nitroxide radical can be described as a spin system consisting of an electron spin $S = 1/2$ coupled to a nuclear spin $I = 1$ from the ^{14}N atom. The terms of the spin Hamiltonian that need to be considered are the electron Zeeman, nuclear Zeeman,

hyperfine interactions and nuclear quadrupole interactions. The hyperfine interaction between the electron and nuclear spins leads to $(2I + 1)$ energy levels and thus to the characteristic three-line spectrum (see **Figure 1.6a**). In the molecular coordinate system of a nitroxide radical, the principal z axis is defined as parallel to the $2p_z$ orbital of the nitrogen atom (see **Figure 1.5a**). The x axis is aligned with the N-O bond and the y axis is defined as perpendicular to the resulting xz plane. The unpaired electron is located primarily in the π bond formed by the p_z orbitals of nitrogen and oxygen atom. Due to sp hybridisation of the N-O bond, s orbital spin density is observed, but only little further delocalization onto the carbon atoms takes place. However, this slight delocalization leads to hyperfine interaction with naturally abundant ^{13}C (with $I = 1/2$) in the carbon atoms and can result in low-intensity doublets around each spectral line.

Apart from that, the features of the nitroxide EPR spectrum are determined by the anisotropy of the $\boldsymbol{g}$ and $\boldsymbol{A}$ tensors. The $\boldsymbol{g}$ tensor differs slightly from g_e because of SOC of low-lying excited states of the oxygen atom that have unquenched orbital angular momenta (see chapter 1.4.2.1). The largest deviation is seen for g_x, where the field is parallel to the N–O bond (the x axis of the molecular coordinate system), lesser in g_y and almost none in g_z along the lobes of the $2p_z$ orbitals. For the hyperfine tensor $\boldsymbol{A}$, the greatest hyperfine coupling - and thus, the largest splitting - is seen when the external magnetic field is aligned parallel with the $2p_z$ lobes, while the hyperfine coupling in the x and y directions is small. For MTSL, the principal values of the $\boldsymbol{g}$ and $\boldsymbol{A}$ tensors are $g_x \approx 2.0083 - 2.0091$, $g_y \approx 2.0061$, $g_z \approx 2.0022$, $A_x/h = A_y/h \approx 12 - 13\ MHz$ and $A_z/h \approx 92 - 103\ MHz$.[127]

1.4.4.2 Spectral shape of nitroxide cw EPR spectra

The molecular motion of nitroxide radicals, in particular the rotational diffusion or tumbling, significantly modulates their spectral shape by partial averaging of the anisotropies of $\boldsymbol{g}$ and $\boldsymbol{A}$. The rotational correlation time τ_c characterizes this tumbling. As such, the molecular motion can be classified into four different regimes that are defined by the ratio of τ_c and the frequency width of the spectrum $\Delta\omega$ as a measure for the difference in resonance frequency for different molecular orientations. The isotropic limit is defined as $\tau_c^{-1}/\Delta\omega \gg 1$, where the anisotropic interactions are averaged out and only the isotropic average is observed. The center line is then at the field corresponding to the isotropic g value ($g_{iso} = g_x + g_y + g_z/3$) and the splitting between the outer lines is equal to the isotropic A tensor $A_{iso} = (A_x + A_y + A_z)/3$. As an example serves the EPR spectrum of MTSL freely tumbling in solution (**Figure 1.6b**). The fast-motion regime with $\tau_c^{-1}/\Delta\omega > 1$ is characterized by the high-field line of the

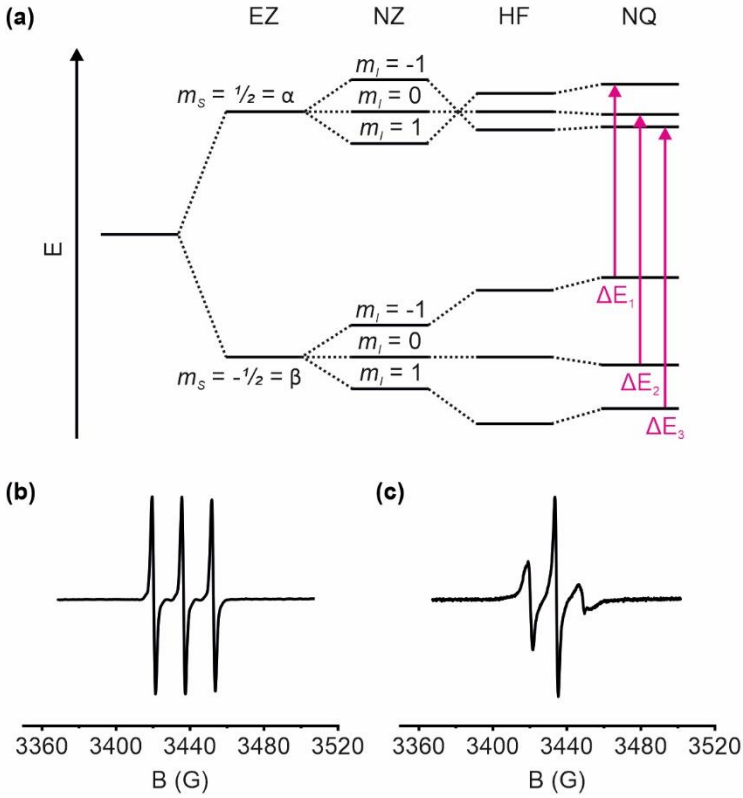

Figure 1.6. Continuous wave EPR spectroscopy on nitroxide radicals. (a) Energy-level diagram for a nitroxide-like spin system with $S = 1/2$ and $I = 1$. The splitting caused by the electron Zeeman (EZ), nuclear Zeeman (NZ) hyperfine (HF) and nuclear quadrupole (NQ) interactions are shown, leading to three EPR transitions indicated in pink. (b) Continuous wave EPR spectrum of 100 µM MTSL in H_2O. (c) Continuous wave EPR spectrum of a 65 µM sample of MTSL labelled TmrAB variant A416R1^A . Spectra recorded as described in chapter 3.2.6.

spectrum being very sensitive to changes in τ_c due to largest anisotropy from the combined influence of $\boldsymbol{g}$ and $\boldsymbol{A}$. In the slow-motion regime with $\tau_c^{-1}/\Delta\omega \approx 1$, the effect of $\boldsymbol{g}$ and $\boldsymbol{A}$ anisotropy is further increased, while some motional averaging still

occurs. For nitroxide radicals at X-band frequencies, the transition from fast-motion to slow-motion regime starts at $\tau_c > 1 - 2\ ns$. This can be the case for a nitroxide label attached to a large protein that reduces its mobility. In the case of very long correlation times with $\tau_c^{-1}/\Delta\omega \ll 1$, the rigid limit is reached, and no averaging of the anisotropy occurs. This regime is observed for power spectra and frozen solutions. These spectra can be described as a superposition of the EPR spectra of radicals that are randomly immobilized with respect to the external magnetic field. This leads to an inhomogeneously broadened line with an approximately Gaussian shape.

In addition, the choice of the magnetic field strength and the resulting resonance frequencies affects the influence of $\boldsymbol{g}$ and $\boldsymbol{A}$ anisotropy on the spectral shape. At X-band frequencies, the hyperfine anisotropy is the dominating contribution and the especially large A_z value determines the spectral breadth. At Q-band frequencies and higher, the anisotropy of the $\boldsymbol{g}$ tensor becomes increasingly important.

In a real sample of a nitroxide spin label such as MTSL attached to a biomolecule, the spectral shape is complicated by radicals with different degrees of mobility: the presence of residual free spin label will affect the spectrum by adding the characteristic three-line spectrum with small linewidth. The choice of the labelling position itself influences the spectral shape, as well. Depending on the surroundings of the MTSL radical, the rotational bonds (see chapter 1.4.3) can be hindered in their mobility to a greater or lesser extent, and several distinguishable spectral fractions can emerge. As such, MTSL attached at different positions of TmrAB displays a characteristic EPR spectrum (**Figure 1.6c** and **Supplementary Figure S1**). The analysis and interpretation of these aspects of EPR spectra can thus yield important information about the structure of biomolecules, such as the effect of the surrounding secondary structure components and amino acid side chains, while their dynamic properties can be inferred by determining τ_c.[176]

1.4.5 Pulse EPR

Small interactions, whose splittings are not resolved in the EPR spectrum, are not fully accessible by cw EPR approaches. Pulse EPR serves as a powerful tool to disentangle these overlapping signals and coupling contributions by spreading the spectrum into an additional dimension. In pulse EPR, short but high-power MW irradiation pulses ($\approx 50\ W$ at Q-band frequencies) are applied to a sample to induce spin transitions, in contrast to continuous irradiation applied in cw EPR experiments. Instrumentally, amplification of the MW field at the sample is achieved by a resonator, as for cw EPR. Opposed to the instrumentation of cw EPR experiments, the resonators employed in pulse EPR setups need to have a higher bandwidth ($\approx 100\ MHz$ or more)

to allow for the excitation of more spins. To achieve this, the resonator is not critically coupled but can be overcoupled, which further increases the bandwidth. However, overcoupling reduces the detection efficiency, and a balance between excitation and detection has to be maintained. In pulse EPR, the emission from the spins is detected that is caused by the precessing magnetic moments (see chapter 1.4.5.1). The detector has to be protected from the high MW power that is in the resonator during a MW pulse and directly after, when the built up MW power dissipates exponentially in the so-called ringdown. Therefore, signal recording is not possible during that time, which is called the deadtime t_d of the spectrometer.

1.4.5.1 Classical dynamics and rotating frame

Although the theory of EPR is based on the quantum mechanical descriptions of chapter 1.4.1, it can be helpful to visualize spin dynamics based on a classical description. All spins in an ensemble of spins that have an identical or almost identical resonance frequency are called a spin packet. In a spin packet, the individual magnetic moment vectors $\boldsymbol{\mu}_i$ (introduced in eq 1.2) add up to a total magnetic moment vector $\boldsymbol{M}$. In the presence of a static external magnetic field $\boldsymbol{B}_0$ that is directed along the z axis, and at thermal equilibrium, $\boldsymbol{M}$ is invariant and aligned parallel to $\boldsymbol{B}_0$. The application of a MW pulse at the frequency $\omega_{MW} = 2\pi\nu$ introduces a second, linearly oscillating magnetic field component $\boldsymbol{B}_1$. If the field is set along the x axis and perpendicular to $\boldsymbol{B}_0$, the effect of the oscillating field on $\boldsymbol{M}$ is maximized, with

$$\boldsymbol{B}_1 = 2B_1 \cos(\omega_{MW} t)\, \boldsymbol{x} \tag{1.24}$$

This additional field perturbs $\boldsymbol{M}$ and tilts it away from the z axis with an effective torque. As a result of this torque, $\boldsymbol{M}$ starts to precess around the z axis in a counterclockwise direction with the Larmor frequency

$$\omega_S = \frac{g_e \beta_e \boldsymbol{B}_0}{\hbar} \tag{1.25}$$

Since $\boldsymbol{B}_1$ is time-dependent, it is helpful to introduce a rotating laboratory frame. This rotating frame rotates counterclockwise around the z axis with $\omega_{rot} = \omega_{MW}$. As a result, $\boldsymbol{B}_1$ becomes time-independent. In this rotating frame and in the absence of $\boldsymbol{B}_1$, $\boldsymbol{M}$ precesses around the z axis with a resonance offset frequency

$$\Omega_S = \omega_S - \omega_{MW} \tag{1.26}$$

In the case that the spin packet is in resonance with the MW frequency ($\omega_S = \omega_{MW}$), the resonance offset is zero, and $\boldsymbol{M}$ is invariant to the rotating frame in the

absence of MW irradiation. If MW irradiation is present, $\boldsymbol{M}$ starts to precess around the x axis with the Rabi frequency ω_{nut};

$$\omega_{nut} = \frac{g_e \beta_e \boldsymbol{B}_1}{\hbar} \tag{1.27}$$

By limiting the duration of the MW irradiation to a short pulse with the duration t_p, $\boldsymbol{M}$ is rotated by the flip angle

$$\theta = \omega_{nut} t_p \tag{1.28}$$

As can be seen in eq 1.28, adjusting the pulse length can be used to obtain specific flip angles. The most common flip angles are $\pi/2$ (90°) and π (180°). Often the effective MW field is so strong that during the pulse, Ω_S can be neglected and not only exactly resonant spin packets are flipped according to eq 1.28.

1.4.5.2 Relaxation

In pulse EPR, the component of $\boldsymbol{M}$ precessing in the transverse xy plane is detected and measured. In the simplest experiment, a $\pi/2$ pulse is applied along the x axis, rotating a set of spin packets that are on resonance by 90° onto the y axis. This total magnetic moment in xy plane leads to an immediate transient signal called free induction decay (FID). Subsequently, the FID loses intensity due to relaxation processes, this relaxation can be described in terms of two time constants T_1 and T_2. The longitudinal or spin-lattice relaxation time constant T_1 describes the return of the magnetization back towards thermal equilibrium M_0 along the z axis:

$$\frac{dM_z}{dt} = \frac{-(M_z - M_0)}{T_1} \tag{1.29}$$

After flipping $\boldsymbol{M}$ into the xy plane, the individual spin packets begin to precess with their individual Ω_S around the z axis. Due to their different precession frequencies, the magnetic moments spread out in the xy plane. This dephasing or loss of coherence decreases the effective $\boldsymbol{M}$ in the xy plane. The transverse or spin-spin relaxation time constant describes the exponential decay of phase coherence between spin packets:

$$\frac{dM_{x,y}}{dt} = \frac{-M_{x,y}}{T_2} \tag{1.30}$$

The coherence in the xy plane is lost much faster than $\boldsymbol{M}$ relaxes back onto the z axis. Therefore, T_2 is always shorter than T_1. Experimentally, the phase memory relaxation time constant T_m is more easily determined using a two-pulse echo (see

chapter 1.4.5.3) with an incremented delay τ. The resulting echo decay can be fitted with an exponential or stretched exponential $\exp(-(2\tau/T_m)^d)$ where d assumes values between 1 and 2. T_m contains T_2 as well as other processes and is thus shorter than T_2. The main source of phase memory relaxation is dephasing due to hyperfine couplings between the electron spins and its surrounding protons in the solvent or within the molecule.[177] For spin labels attached to buried residues in a protein, T_m is usually in the range of 0.6 and 2.0 µs because of protons in rotating methyl groups. In the case of solvent-exposed residues, T_m is longer with a range of 2 to 3 µs, mainly due to nuclear spin diffusion in a protonated solvent.[178] Knowledge about the timescale on which the magnetic moments dephase determines the possible length of interpulse delays and is important for advanced pulse EPR experiments (see chapter 1.4.6.1). In order to optimize T_1 and T_m, measurements are usually conducted in the temperature range of 10 to 80 K.

1.4.5.3 The spin echo

In the primary echo or Hahn echo sequence, a $\pi/2$ pulse is applied that results in an FID and the magnetic moments undergo dephasing. After a time τ, a π pulse is applied, flipping the spin packets by 180° in the transverse plane. However, now the spin packets that precessed faster due to a higher precession frequency lag behind the ones with a lower precession frequency. At time τ after the second pulse, they refocus into a primary or Hahn echo, before dephasing again. The echo amplitude is proportional to the number of excited spins. This Hahn echo sequence is fundamental for other pulse sequences and serves as the detection sequence.

In addition, an echo-detected field-swept (EDFS) spectrum can be obtained by recording the Hahn echo as a function of the magnetic field. Due to the different detection methods, an EDFS spectrum is not detected as the first derivate as is the case for a field-swept cw EPR spectrum.

1.4.5.4 Pulse shapes

Different pulse shapes can be employed for the manipulation of spins. A rectangular pulse is obtained by turning on the MW field at a time $t = 0$ and turning if off at a time $t = t_p$. By Fourier transformation (FT) of the pulse shape in the time domain, the excitation profile $P(\Omega_S)$ of the pulse in the frequency domain can be approximated. For a rectangular pulse, this corresponds to a sinc function

$$P(\Omega_S) = \left| \frac{\sin(\Omega_S t_p)/2}{\Omega_S/2} \right| \tag{1.31}$$

and thus, the excitation profile has side lobes that can interfere with a selective excitation of specific spin packets. As an alternative, shaped pulses can be generated with an arbitrary waveform generator (AWG).[179] Gaussian pulses are characterized by a Gaussian shape in the time domain and a roughly Gaussian shape of the excitation profile with fast decaying wings. Furthermore, so-called chirp pulses can be generated, where the frequency is changed linearly. With such a pulse, lower available power can be sufficient to excite transitions in a larger frequency range.[180]

1.4.6 Pulse electron-electron double resonance

As mentioned in chapter 1.4.2.6, weak couplings between electron spins can be employed to determine the distances between the respective paramagnetic centers, for instance on biomolecules with two covalently attached spin labels (see chapter 1.4.3), and thus two electron spins A and B. The refocusing of an echo is affected by electron-electron coupling and can hence be manipulated. However, this modulation is usually small and obscured by more prominent effects, such as nuclear modulations or spin-spin relaxation. By applying a pulse sequence, the electron-electron coupling can be separated from other contributions. One of such experiments is known as double electron-electron resonance (DEER) or pulse electron-electron double resonance (PELDOR) – for the remainder of this work, the latter name will be used. In proteins, interspin distances between $r_{AB,min} \approx 2\ nm$ and $r_{AB,max} = 10\ nm$ can usually be determined.[181]

At X- or Q-band frequencies, EPR spectra of nitroxides are rather broad, and many pulse EPR experiments would require a large excitation bandwidth. To solve this problem, a second pulse at a different MW frequency affecting the spin system can be introduced: in the three-pulse PELDOR experiment, a Hahn echo sequence with a fixed interpulse delay τ is applied at the observer frequency ω_A, where the A spins are excited and refocussed (**Figure 1.7a**). In addition, a π flip pulse is applied at the pump frequency ω_B (that does not overlap with the pulses at ω_A) to the B spins with a variable delay t after the $\pi/2$ pulse of the observer sequence.[182] Without the pump pulse, the electron-electron couplings between the A and B spins would be refocussed and would not affect the echo amplitude. By applying the pump pulse and inverting the B spins, the local field that affects the A spins is changed, leading to a shift in the precession frequency of the A spins. Since the position of the pump pulse is varied by t, the detected magnetisation of the A spins at the time 2τ of echo formation will be shifted out of phase by an angle $\Delta\phi_{ee} = \omega_{ee}t$ with the electron-electron coupling frequency given by ω_{ee}. Since the Heisenberg exchange coupling is negligible above $2\ nm$, this modulation of the echo amplitude $V(t)$ as a function of t is determined by

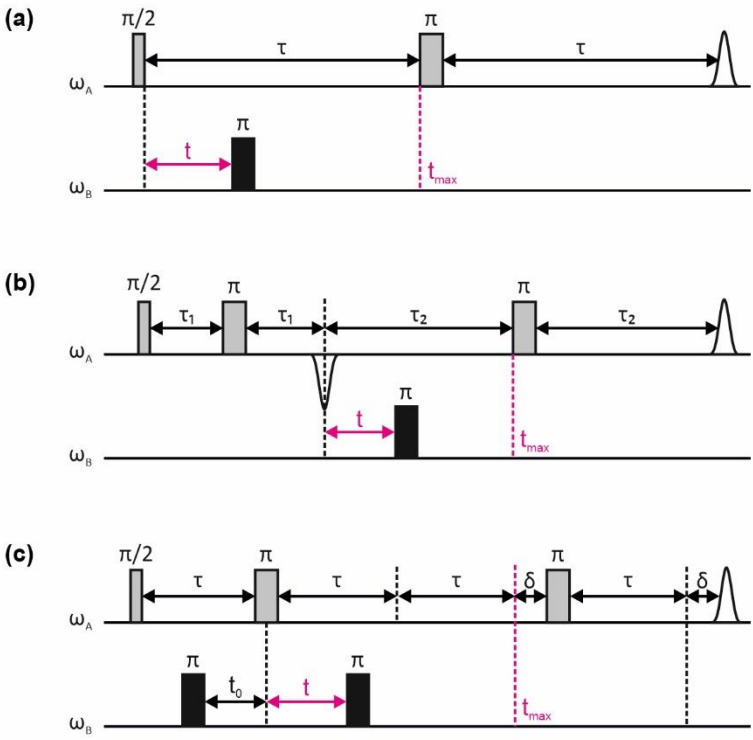

Figure 1.7. Pulse sequences for PELDOR spectroscopy. The non-stationary π pump pulse is varied with a time t up to t_{max}. (a) Three-pulse PELDOR sequence as explained in chapter 1.4.6. (b) Four-pulse PELDOR sequence as explained in chapter 1.4.6.1. (c) Five-pulse PELDOR sequence as explained in chapter 1.4.6.2.

the dipole-dipole coupling ω_{AB}. The dipole-dipole coupling depends on the angle θ_{AB} between the spin-spin vector $\boldsymbol{r}_{AB}$ and $\boldsymbol{B}_0$, where θ_{AB} is distributed between 0 and $\pi/2$. In the absence of orientation selection and for an isolated spin pair, FT of $V(t)$ gives the dipolar spectrum (Pake pattern). For a rigid system, the interspin distance can be determined directly from the frequency corresponding to the singularities ($\theta_{AB} = 0\ or\ 90°$). In reality, however, the dipole-dipole coupling can feature some distribution, e.g., when two spin labels are attached to a biomolecule that exists in a conformational distribution. In such a case, the singularities are not defined anymore

and the distance distribution $P(r)$ needs to be computed. Different approaches to obtain the distance distribution from $V(t)$ are discussed in chapter 1.4.8.

The spatial distribution of spins B that are further away from an A spin than $r_{AB,max}$ cannot be determined from $V(t)$, but they nevertheless contribute to the decay of $V(t)$. To obtain $P(r)$, $V(t)$ needs to be suitable to be separated into an intramolecular contribution $F(t)$ and an intermolecular contribution $B(t)$ that accounts for the above-mentioned additional decay:

$$V(t) = F(t)B(t) \tag{1.32}$$

The $F(t)$ is a function of ω_{AB} and the modulation depth Δ, and contains thus information about the number of spins interacting (through Δ) and the distance distribution (through ω_{AB}). Within a decay time t_{dec}, $F(t)$ becomes constant, depending on the longest distance in $P(r)$. If $V(t)$ is observed for a sufficient amount of time $t_{max} \gg t_{dec}$, $B(t)$ can be obtained by fitting an appropriate function to $V(t)$. For a homogeneous spin distribution in three dimensions, as is the case for a frozen solution of soluble or solubilized protein, $B(t)$ can be described by an exponential decay

$$B(t) = exp\left[-(kt)^{d/3}\right] \tag{1.33}$$

with d as a fractal dimension that assumes the value 3 for the above-mentioned case. In two-dimensional lipid bilayers or membranes, the intermolecular distribution is not homogeneously distributed in three dimensions, and d can approach values of 2. The decay rate constant k also takes into account the spin concentration and the angle of spin rotation by the pumping pulse.[183]

1.4.6.1 Four-Pulse PELDOR

In the three-pulse PELDOR setup, the $\pi/2$ observer pulse and π pump pulse overlap at $t = 0$. This results in a dead time t_d that is two to three times the length of the pulse. This leads to distortions that make it impossible to determine short distances of about $r_{AB} < 3\ nm$ or broad distance distributions.

To remedy this problem, the four-pulse PELDOR sequence with zero dead time can be employed.[184,185] While in the three-pulse PELDOR experiment, the effect of the pump pulse on the Hahn echo is observed, the four-pulse PELDOR sequence probes the influence of the pump pulse on a refocused echo. First, a Hahn echo sequence at ω_A induces a primary echo at time $2\tau_1$. The observer sequence is then extended by another π pulse after a time τ_2, leading to a refocussed echo at time $2\tau_2$ (**Figure 1.7b**). The π pump pulse at ω_B is applied after the first π pulse of the observer sequence, so

that $t_0 = 2\tau_1$ and $t_{max} < \tau_2$. The inversion of the B spins therefore now modulates the refocussed echo intensity.

The application of three pulses at the observer frequency (and the pump pulse, depending on excitation band overlap and coherence), generates coherence also for pulse combinations other than the stimulated or refocused echo at different evolution times. These unwanted echoes can overlap with the detected echo and hence lead to artifacts, which increases considerably with the number of additional pulses. These background signals can be removed by phase cycling.[184] The phases of the excitation pulses are alternated, and the detected signals are either added up or subtracted to select for the wanted coherence-transfer pathway.

Four-pulse PELDOR is widely employed for the investigation of distances between spin labels in biomolecules, and is the main technique used in this work. However, relaxation - mainly phase memory relaxation - is a major factor and T_m limits the possible distance range that can be measured. The effect of nuclear spin diffusion (see chapter 1.4.5.2) can be reduced by using deuterated solvent or adding deuterated glycerol to a sample. Nevertheless, precise determination of a distance distribution is usually restricted to $< 5\ nm$.[178]

1.4.6.2 Five-Pulse PELDOR

The effect of nuclear spin diffusion on the transversal relaxation time can be reduced by choosing identical interpulse delay times $\tau_1 = \tau_2 = \tau$, thus prolonging the lifetime of the transversal spin coherence and improving sensitivity. However, in this scenario and with only one pump pulse, refocussing occurs in the centre of the second interval, effectively limiting the maximum time trace evolution t_{max} that can be recorded. The accessible distance range can nevertheless be extended by applying a second, stationary pump pulse at frequency ω_B before the first observer π pulse (**Figure 1.7c**).[178] This fixed pump pulse inverts the dipole-dipole coupling and shifts the phase of the dipolar coupling to virtually double the effective length of the measured PELDOR time trace. Thus, a longer dipolar evolution time can be exploited and larger interspin distances are accessible. There is a fraction of B spins that is inverted by the time-variable pump pulse but not by the stationary one, opening additional coherence transfer pathways that lead to artifact contributions. These contributions can be corrected with the use of dedicated algorithms.[186] Furthermore, as for four-pulse PELDOR, extensive phase-cycling needs to be applied to remove additional echoes, e.g., from the incomplete coherence transfer of the two observer π pulses that would otherwise exactly superimpose with the refocussed echo. By additionally shifting the position of the second observer π pulse by the small time delay δ, one unwanted,

stimulated echo can be separated from the wanted, refocused PELDOR echo and phase cycling becomes less complex.

1.4.7 Divalent manganese in EPR spectroscopy

As explained in chapter 1.2.1, magnesium ions are necessary for the hydrolysis of ATP to ADP and P_i to be catalyzed by ABC exporters. This implies that Mg^{2+} ions are present in the NBSs during the transport cycle and is in alignment with cryo-EM structures, where Mg^{2+} ions are localized in the active sites of both c-NBS and d-NBS of TmrAB in samples prepared with excess of ATP and Mg^{2+}.[104]

Divalent manganese (Mn^{2+}) has an ionic radius of approximately 0.75 Å, while Mg^{2+} has a radius of 0.65 Å. Because of this similarity in size and charge, Mn^{2+} can substitute Mg^{2+} in biological systems and biochemical reactions.[187] It was shown that the catalytic activity of an enzyme is maintained if Mg^{2+} is replaced by Mn^{2+} in the active site of a magnesium-dependent enzyme.[188] ATP hydrolysis could be retained in an ABC transporter for maltose with Mn^{2+} substitution.[189] Unlike Mg^{2+}, however, divalent manganese is paramagnetic, and can thus serve as a spectroscopically active replacement for magnesium.[190]

EPR spectra of Mn^{2+} are dominated by the large hyperfine interaction between the Mn^{2+} electron spin and the ^{55}Mn nucleus which can reach values of approximately 260 MHz for octahedral complexes.[191] Due to its electron spin of $S = 5/2$, Mn^{2+} has six electron spin states. Hyperfine coupling to the ^{55}Mn nucleus with $I = 5/2$ leads to a splitting of each of the six electron spin levels into six further states, leading to 36 energy states with 30 allowed transitions. Since the electronic $\boldsymbol{g}$ tensor and the hyperfine tensor $\boldsymbol{A}$ are almost isotropic for Mn^{2+}, an angular dependence of the spectrum is mainly arising from ZFS. For a perfectly symmetrical complex that undergoes fast molecular tumbling, the $|m_S, m_I\rangle$ states are nearly degenerate, which gives rise to six sharp lines of five superimposed transitions. In a frozen solution or powder, however, the ZFS is no longer averaged and has an impact on the spectral shape. For different m_s values, the transitions $|m_S, m_I\rangle \leftrightarrow |m_S \pm 1, m_I\rangle$ depend differently on the zero-field interaction. While the central transition $|\pm 1/2\,, m_I\rangle \leftrightarrow |\mp 1/2, m_I\rangle$ contains no zero-field interaction in its first-order term, the four outer transitions $|\pm 3/2\,, m_I\rangle \leftrightarrow |\pm 1/2, m_I\rangle$ and $|\pm 5/2\,, m_I\rangle \leftrightarrow |\pm 3/2, m_I\rangle$ show an anisotropic dependency of the ZFS on the axial and rhombic zero-field parameter D

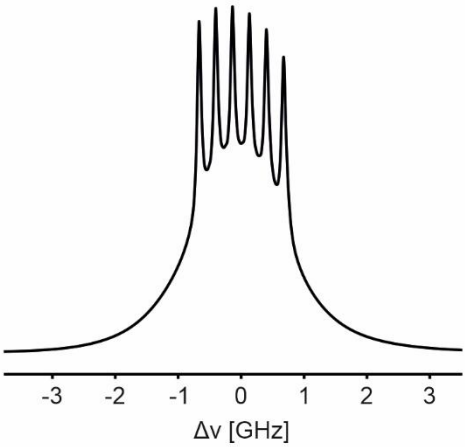

Figure 1.8. Simulated EPR spectrum of a Mn^{2+} complex at 5 K and at Q-band frequencies. An isotropic g value g_{iso} = 2.00388, a hyperfine coupling constant a_{iso} = -269 MHz, an axial zero-field parameter D = 500 MHz and a D-strain = 1000 MHz were chosen. Spectrum simulated using the Matlab toolbox EasySpin 5.2.35.

and E. Therefore, only the central transition is characterized by the six sharp signals of the hyperfine coupling, while the outer transitions are broad, leading to the characteristic spectrum of Mn^{2+}-complexes in frozen solution (**Figure 1.8**). Because of small structural variations between the paramagnetic centers, the zero-field parameters are distributed (so-called D and E strains), which results in the outer electron transitions being further broadened. However, higher-order terms for the ZFS have to be considered as well, and the precise spectral shape is strongly affected by the surrounding ligands and the resulting electron distribution.

Often, pulsed Mn^{2+} experiments are performed with the pump or observer frequency positioned on one of the central six hyperfine transitions to obtain a good s/n ratio. As Mn^{2+} exhibits a very broad spectrum, chirp pulses (see chapter 1.4.5.4) can be employed to excite more spins and obtain a better dipolar modulation depth. Typically, experiments are conducted at 5 K to achieve a longer transversal relaxation time T_2. When combining Mn^{2+} with another paramagnetic species, such as a nitroxide spin label with longer T_1 and T_2 times, too high Mn^{2+} concentrations can induce fast relaxation of the nitroxide spins, thus rendering distance measurements difficult or impossible.

In recent years, PELDOR spectroscopy was utilized to determine the distance distribution between a nitroxide spin label and Mn^{2+} in synthetic model compounds.[192,193] Furthermore, Mg^{2+}-to-Mn^{2+} exchange was applied to study ABC transporters by pulse electron-nuclear double resonance (ENDOR).[194] The same substitution was used in the ABC transporters MsbA[195] and BmrA[196] to measure distances between the metal ion centers using PELDOR spectroscopy. However, Mn^{2+}-NO distance measurements have not yet been performed in complex biomolecules such as ABC transporters to further our structural and functional understanding. Such orthogonal spin label approaches are advantageous, as different inter spin distances have different spectroscopic access and can thus be correlated within one sample. A remarkable application of orthogonal spin labelling was the Gd^{3+}-Trityl-Nitroxide triple labelling of the cobalamin transport system.[197]

1.4.8 Data analysis

1.4.8.1 Basic considerations

In this subchapter, the theoretical background for the analysis of PELDOR data is explained, based on the following literature.[181,198,199] As explained in chapter 1.4.6, PELDOR experiments measure the modulation of the amplitude $V(t)$ of spin echoes as a function of the position of the pump pulse(s), and thus give information about the dipole-dipole couplings between the spins. The echo amplitude $V(t)$ can be given as

$$V(t) = V_0 \cdot V_{intra}(t) \cdot V_{inter}(t) \tag{1.34}$$

with V_0 as the amplitude in absence of pump pulses, V_{intra} as modulations of the amplitude from intra-molecualr spin couplings, and V_{inter} as modulations of the amplitude from inter-molecular spin couplings. It can also be written as

$$V(t) = \int_0^\infty K(t,r)P(r)dr \tag{1.35}$$

with the distance distribution $P(r)$ and the kernel $K(t,r)$ that describes how the distance distribution determines the modulation of the amplitude. For a four-pulse PELDOR experiment, the kernel is given by

$$K(t,r) = [(1-\Delta) + \Delta K_0(t,r)]V_{inter}(t,\Delta) \tag{1.36}$$

and contains the modulation depth Δ and the elementary kernel K_0:

$$K_0(t,r) = \int_0^1 cos[(1-3\cos^2\Theta)\mathrm{Dr}^{-3}\mathrm{t}]\, dcos\,\Theta \tag{1.37}$$

In $K_0(t,r)$, D is the dipolar coupling constant

$$D = \frac{\mu_0}{4\pi}\frac{g_e^2\mu_B^2}{\hbar} \tag{1.38}$$

Experimentally, the modulation of the amplitude $V(t)$ is acquired as a dipolar signal vector $\boldsymbol{V}$, consisting of n data points with equally spaced time points t_i. Likewise, the distance distribution $P(r)$ can be given as a vector $\boldsymbol{P}$ with m elements at equally spaced distances r_j, and the physical model for such data can be written by a matrix equation as

$$\boldsymbol{V} = \boldsymbol{K}\boldsymbol{P} \tag{1.39}$$

with $\boldsymbol{K}$ as the $n \times m$ kernel matrix with the elements $(K)_{ij} = K(t_i r_j)\Delta r$ where Δr is the increment in the distance domain. However, the experimentally measured signal is corrupted by noise. It was shown that this noise can be approximated by a Gaussian distribution that is uncorrelated and of constant variance σ^2,[200] and can be written as

$$\boldsymbol{V}_{exp} = \boldsymbol{V} + \mathcal{N}\,(0,\sigma^2) \tag{1.40}$$

Since the distance distribution is to be inferred from the dipolar signal, the kernel matrix has to be inverted:

$$\boldsymbol{P} = \boldsymbol{K}^{-1}\boldsymbol{V}_{exp} \tag{1.41}$$

However, the kernel matrix has a very large condition number (the ratio of its largest versus its smallest singular value), which results in an ill-posed inverted problem that is unstable and prone to errors. Small changes in the data, e.g. through noise, will result in a large error in $\boldsymbol{P}$. To stabilize the solutions, two methods currently see the widest application. The difference between these methods lies in the distance distribution either being represented as a non-parametric model or as a parametric model. In this work, the Python-based open-source software DeerLab[199] was used for the determination of distance distributions from PELDOR experiments. Both parametric and non-parametric stabilization approaches are implemented in DeerLab and can be fit directly to the primary data $V(t)$ in a one-step analysis that also fits a parametric background model to the data.

1.4.8.2 Regularization strategies

In the first approach, a non-parametrized model is used to represent $\boldsymbol{P}$, and regularisation methods are necessary to calculate the solution. The most common regularisation method for PELDOR data is Tikhonov regularisation[201]:

$$\boldsymbol{P}_{\boldsymbol{fit}} = \left\|\boldsymbol{V}_{exp} - \boldsymbol{K}\boldsymbol{P}\right\|^2 + \alpha\left\|\hat{\boldsymbol{L}}\boldsymbol{P}\right\|^2 \tag{1.42}$$

The first term represents a least-squares term and quantifies the quality of the model fitting to the data. The second term represents a penalty term, where $\hat{\boldsymbol{L}}$ is a second-order difference matrix to impose smoothness on the fit, and α is the Tikhonov regularization parameter that weighs the penalty term and thus balances data agreement and regularization. A non-negativity constraint $\boldsymbol{P} \geq 0$ is applied to obtain physically meaningful results, this constraint and the penalty term stabilize the solution. Therefore, $\left\|\boldsymbol{V}_{exp} - \boldsymbol{K}\boldsymbol{P}\right\|^2$ will minimize the misfit between data and model, while $\alpha\left\|\hat{\boldsymbol{L}}\boldsymbol{P}\right\|^2$ will penalize overfitting and jagged distance distributions. Small values for α result in a spiky distance distribution, large values for α lead to an overly smooth distance distribution. Thus, $\boldsymbol{G}(\alpha)$ is minimized for every α to obtain the best solution for $\boldsymbol{P}$, and a good choice of α is crucial. Different methods exist for the selection of α. Traditionally, the L-curve criterion was employed.[202] However, studies showed that other selection methods such as the Akaike information criterion (AIC) can provide better results.[203] The default criterion in DeerLab, which is also the criterion of choice in this work, is the AIC.

Employing regularization, one common approach is two-step analysis. First, a parametric background model is fit to the time-domain signal, which is corrected by the fitted background. Then, the above explained regularization is applied to the background-corrected signal. The background fit in this approach assumes that the total signal length is much longer than the oscillation periods of the signal in the time-domain. However, this is not always the case, and two-step analysis is not optimal to process such signals. To remedy this problem, DeerLab implemented a one-step analysis approach that simultaneously fits the parameters of the time domain $\boldsymbol{\theta}$ and the non-parametric distance distribution $\boldsymbol{P}$ to the signal $\boldsymbol{V}_{exp}$ by minimizing eq 1.43:

$$F(\boldsymbol{\theta}, \boldsymbol{P}) = \left\|\boldsymbol{V}_{exp} - \boldsymbol{K}[\boldsymbol{\theta}]\boldsymbol{P}\right\|^2 + \alpha\left\|\hat{\boldsymbol{L}}\boldsymbol{P}\right\|^2 \tag{1.43}$$

DeerLab solves eq 1.43 with a nested subspace optimization algorithm that is based on separable non-linear least squares, as demonstrated in previous publications.[204,205] In this algorithm, the $\boldsymbol{\theta}$ and $\boldsymbol{P}$ spaces are separated and solved by a non-linear least-squares algorithm. Then $\boldsymbol{P}$ is determined as $\boldsymbol{P}[\boldsymbol{\theta}]$ for a given $\boldsymbol{\theta}$, calculated by

(Tikhonov) regularization. This algorithm procedure is iterative. It guesses a starting value for $\boldsymbol{\theta}$ to determine $\boldsymbol{P}[\boldsymbol{\theta}]$, which is then again used to determine the next $\boldsymbol{\theta}$ until the resulting values converge. Since $\boldsymbol{P}[\boldsymbol{\theta}]$ now depends on $\boldsymbol{\theta}$, it is a parametric model, but it only contains the background parameters and modulation depth.

1.4.8.3 Parametric models

In the second approach, $\boldsymbol{P}$ is represented by a parametrized model and requires the distance distribution to have an underlying shape. Often, a small number of Gaussian peaks is chosen for this, given as a linear combination of normalized Gaussian functions[206]:

$$\boldsymbol{P}[\boldsymbol{\theta}] = \sum_{i=1}^{N} a_i \boldsymbol{p}_i[\bar{r}_i \sigma_i] \tag{1.43}$$

with a_i as the amplitudes, $\boldsymbol{p_i}$ as the normalized Gaussian functions, $\bar{r}_i$ as the center distances of the Gaussians, and σ_i as the full widths at half maximum. Furthermore, DeerLab allows both modulation depth and background (as a stretched exponential) to be included in the analysis of the signal, resulting in the following parametric model for the time domain:

$$\boldsymbol{V}[\boldsymbol{\theta}] = \mathbf{V}[\Delta, \boldsymbol{\Theta}_P \boldsymbol{\Theta}_B] = \mathbf{K}[\Delta, \boldsymbol{\Theta}_B] \boldsymbol{P}[\boldsymbol{\Theta}_P] \tag{1.44}$$

In eq 1.44, the parameter vector $\boldsymbol{\theta}$ contains the parameters for the distance distribution $\boldsymbol{\Theta}_P$, as well as the parameters for the background $\boldsymbol{\Theta}_B$ and the modulation depth. By minimizing the equation

$$\boldsymbol{\Theta}_{fit} = \left\| \boldsymbol{V}_{\boldsymbol{exp}} - \boldsymbol{V}[\boldsymbol{\theta}] \right\|^2 \tag{1.44}$$

the experimental data can then be fitted with a parametrized time-domain model.

However, methods based on parametrized models can suffer from selection bias. It is generally a good practice to use this approach only when there is sufficient reason to assume a good fit of the data, for example by examination with a non-parametrized model based on Tikhonov regularization.

In the context of biological systems, the dynamic switch between conformational states is of interest, for example the transition between an IF and an OF conformation in ABC transporters described in chapter 1.2. In such a case, a non-parametrized analysis approach must first prove that the conformational states of an investigated

system can be sufficiently described by a parametrized model with a fixed number of Gaussians of constant distance $\bar{r}_i$ and width ω_i. If it can be further shown that various sample conditions only lead to differences in the relative populations of said conformational states, then the variation of the Gaussian amplitudes a_i of the fixed number of Gaussians is enough to fit the time-domain data. Data analysis will thus give values for a_i that quantify the relative populations of the conformational states. This approach has been used to quantify the underlying thermodynamics of the conformational transition in TmrAB.[207]

1.4.8.4 Global analysis

Global or simultaneous analysis refers to a single model being fit simultaneously to multiple data sets $\boldsymbol{V}_{exp,i}$ from different experiments that have been collected under different conditions. In dipolar EPR, this was first used for fitting a multi-Gauss distribution model to several DEER datasets[208] but was expanded to non-parametrized analysis[209], too. Global data analysis provides a more profound test of the used model and a more accurate determination of the model parameters. In DeerLab, global analysis can be employed for both parametric and non-parametric distance distribution models. In this work, global analysis of PELDOR traces has been applied for two scenarios.

In the first scenario, all signals $\boldsymbol{V}_{exp,i}$ originate from the same distance distribution, here from one single sample that was measured with a 4-pulse and a 5-pulse PELDOR sequence. The resulting 4-pulse PELDOR signal and 5-pulse PELDOR signal can be simultaneously fit using a non-parametrized model to better recover the underlying ground truth of the distance distribution, especially for samples that contain both shorter and longer distances.

In the second scenario, the signals $\boldsymbol{V}_{exp,i}$ originate from different but related samples with distinct distance distributions. Here, otherwise identical protein samples undergo a conformational transition between different states, as described under 1.5.3. Using one parametrized model to analyse all samples yields a good set of distance distributions with a robust quantification of the investigated relative populations of the conformational states.

2 MOTIVATION

In order to effectively fight multidrug resistance, both in microbes and in cancer cells, and to understand the complex field of cellular transport, the function of ABC transporters must be fully elucidated. While we see an ever-growing number of studies from complementary fields of research that contribute to this topic, there are several facets of ABC transporter function that are not yet understood. The heterodimeric prokaryotic ABC exporter TmrAB represents a remarkable system through its functional homology with TAP and can serve as a blueprint to investigate other ABC exporters with asymmetric NBSs. The fact that many biochemical properties are well investigated, as well as the existence of several high-resolution cryo-EM structures of TmrAB in key conformational states make it an ideal model for the investigation of open questions. In this work, I expanded our understanding of ABC transporters by investigating different aspects of the function of TmrAB. This thesis can be divided into two connected parts.

One of the open questions is to what extent the dimerization of the NBSs is coupled to the conformational change of the TMDs and substrate translocation: while it is generally agreed that the binding of ATP at the NBSs provides the power stroke for the conformational transition of an ABC exporter from the IF to the OF conformation that enables substrate transport, the role of hydrolysis remains elusive. The exact mechanistic details on the conformational level need to be solved, and the dynamic behavior of the protein regions must be investigated. Until now, only few studies have been performed to quantify the conformational kinetics of ABC transporters. The combination of SDSL with pulse EPR measurements such as PELDOR gives us the opportunity to observe the distance distribution of a protein over the sample ensemble and can yield both structural and dynamic information at the same time. In the last years, the thermodynamics of the conformational transitions was uncovered for TmrAB by incubating the transporter with ATP at different temperatures until the equilibrium was reached.[207] A direct kinetic investigation of conformational transitions in an ABC transporter by PELDOR spectroscopy is the next step to elucidate the transport cycle. It can be used to correlate the timescales of conformational transitions in key regions of ABC transporters. As explained in chapter 1.3.3, this is a challenging task. The objective of the first part of this thesis can be defined as: to characterize and compare the underlying kinetic parameters of the conformational transitions in the ABC transporter TmrAB by PELDOR spectroscopy. For this, a time-resolved PELDOR (TR-PELDOR) approach was developed. The results

for these questions will be presented in chapter 4.2. These results will be discussed in chapter 5.1.

For transporters with catalytic asymmetry, the roles of both consensus and degenerate NBS and their coupling to conformational changes of the TMDs during the transport cycle remain another open question. In particular, the role of ATP hydrolysis in the transport cycle is again of central importance. To answer these questions, the conformational changes of the two asymmetric NBSs and the transitions of the TMDs must be simultaneously observed and correlated. This is a challenging task, and not many techniques exist that can concomitantly yield high resolution structural and dynamical information, while also being flexible enough to study a broad range of biochemical conditions. Due to the similarity of paramagnetic Mn^{2+} to Mg^{2+} that is necessary for a functional transport cycle, a Mg^{2+}-to-Mn^{2+} substitution can be used to access the NBDs by EPR techniques such as PELDOR spectroscopy. By strategically positioning the cysteine point substitutions for SDSL, a concomitant probing of the conformational states of NBSs and TMDs could become possible. For the second part of this thesis, the objectives are hence defined as: To distinguish between c-NBS and d-NBS, while concomitantly observing the conformational state of the TMDs using PELDOR spectroscopy, and to assess the asymmetric role of ATP hydrolysis in TmrAB. The results regarding these questions are presented in chapter 4.3 and 4.4 and discussed in chapter 5.2 and 5.3.

3 MATERIAL & METHODS

3.1 Material

3.1.1 Plasmids

For the protein expression in *E. coli*, the TmrAB coding sequence was introduced into the plasmid vector pET22 (**Figure 3.1**). TmrAB contains one native cysteine, $C416^{A}$ (where the superscript A signifies TmrA). To generate double cysteine pairs, this cysteine was removed before other cysteine mutations could be implemented. The cysteine-free variant of TmrAB is denoted as WT*. A decahistidine (10xHis)-tag is coupled to the end of TmrA for purification of the protein via immobilized metal affinity chromatography (IMAC). Apart from the TmrAB gene, the vector carries an ampicillin resistance gene for selection of bacteria. The Lac repressor gene is included to inhibit expression of TmrAB, until IPTG is added during protein expression. The vector contains the T7 promoter for the T7 RNA polymerase, whose gene was incorporated into the chromosomal DNA of the used *E.coli* strain BL21(DE3).

The WT* vector as well as the vectors with the used double-cysteine variants $V288C^{A}$-$E272C^{B}$, $A416C^{A}$-$L458C^{B}$, and $V461C^{A}$-$D349C^{B}$ were prepared by Dr. Katja Barth and are described in literature.[207]

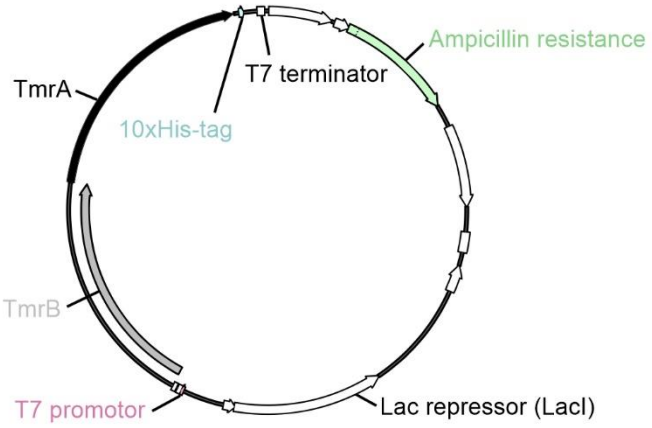

Figure 3.1. Plasmid map of the used pET22 vector with the gene for TmrAB. Only important sequence elements described in the text are highlighted.

3.1.2 Cell lines

For plasmid amplification, the *E. coli* cell line DH5α with a high transformation efficiency was used, acquired from Thermo Fisher. For protein expression, the *E. coli* cell line BL21(DE3) was used that was designed for a controlled expression, obtained from the laboratory of Prof. Dr. Robert Tampé. Cells were made competent for plasmid uptake by treatment with RbCl (see chapter 3.2.1).

3.1.3 Peptide substrate

To investigate the effect of substrate presence on the conformational transition in TmrAB, a short fluorescent peptide (denoted as K5F) with the amino acid sequence RRYCK^{FL}STEL and a fluorescein (FL)-labelled lysine residue was employed. A study investigating the transport activity showed that TmrAB efficiently translocates K5F.[103] K5F was obtained from JPT Peptide Technologies GmbH.

3.1.4 Chemicals and reagents

Table 3.1. List of chemicals and reagents used in this work.

Reagent	Manufacturer
3-(N-morpholino)propanesulfonic acid (MOPS)	Sigma-Aldrich
4-(2-hydroxyethyl)-1-piperazineethanesulfonic acid (HEPES)	Merck
ADP	Merck
Agar	Carl Roth
Ampicillin sodium salt	Carl Roth
ATP	Merck
ATPγS	Merck
Bromophenol blue	Sigma-Aldrich
$CaCl_2$	Merck
CH_3COOK (Potassium acetate)	Sigma-Aldrich
Deuterated glycerol (glycerol-d_8)	Sigma-Aldrich
Dodecyl-β-D-maltosid (β-DDM)	Carl Roth
Dithiothreitol (DTT)	Sigma-Aldrich

Table 3.1. Continuation

Reagent	Manufacturer
EDTA	Merck
Ethanol	Sigma-Aldrich
Glycerol	Carl Roth
H_2SO_4	Carl Roth
Hydrochloric acid	Sigma-Aldrich
Imidazole	Alfa Aesar
IPTG	Carl Roth
K_2HPO_4	Merck
KH_2PO_4	Merck
Lysozyme	Carl Roth
Malachite green chloride	Carl Roth
$MgCl_2$	Carl Roth
$MgSO_4$	Merck
$MnCl_2$	Carl Roth
MTSL	Toronto Research Chemicals
Na_2MoO_4	Carl Roth
Na_3VO_4	Carl Roth
NaCl	Carl Roth
Ni Sepharose High Performance Media	Cytiva
PageRuler Plus prestained protein ladder	Thermo Fisher
RbCl	Carl Roth
S.O.C. (super optimal broth with catabolite repression) medium	Thermo Fisher
SimplyBlue SafeStain Coomassie staining solution	Thermo Fisher
Sodium dodecyl sulfate (SDS)	Sigma-Aldrich
Tris HCl	Sigma-Aldrich

Table 3.1. Continuation

Reagent	Manufacturer
TruPAGE TEA-Tricine SDS Running Buffer	Sigma-Aldrich
Tryptone/Pepton ex casein	Carl Roth
Tween	Carl Roth
Yeast extract	Carl Roth
β-mercaptoethanol (β-ME)	Carl Roth

3.1.5 Kits and consumables

Table 3.2. List of kits and consumables used in this work.

Item	Manufacturer
Bacterial cell spreader	Carl Roth
Desalting Columns PD-10	Cytivia
Disposable cuvettes	Fisherbrand
Disposable petri dishes	Fisher Scientific
Micro Bio-Spin P-6 Gel Column	Bio-Rad
Micropipette 20 µl	Blaubrand
Micropipette controller	Blaubrand
TruPAGE Precast Gels 4 – 12%	Thermo Fisher
Q5 Site-Directed Mutagenesis Kit	New England BioLabs
Q-band EPR tubes Suprasil, 1.6 mm	Wilmad LabGlass
QIAprep Spin Miniprep Kit	QIAGEN
Syringe filters Rotilabo, sterile, 0.22 µm	Carl Roth
Vivaspin 6 filter concentrators	Merck

3.1.6 Equipment

Table 3.3. List of equipment used in this work.

Equipment	Manufacturer
ProFlex PCR System	Applied Biosystems
Gel Doc EZ Imager	Bio-Rad
Analytical Balance Model FAS224	Fisherbrand
Digtal thermometer for PELDOR samples	Thermapen
Nanodrop	Sigma-Aldrich
ClarioStar Plus Microplate Reader	BMG Labtech
MultiTherm Shaker Model H5000-H-E	Thermo Fisher
Incubation shaker Multitron Standard	Infors HT
Incubation shaker Ecotron Small	Infors HT
Microcentrifuge Fresco 21	Heraeus
Centrifuge Megafuge 40R with TX-1000 rotor	Heraeus
Centrifuge RC-5B with GS-3 rotor	Sorvall
Cell density meter model 40	Fisher Scientific
pH meter Accumet AE150	Fisher Scientific
Water purification system Barnstead GenPure	Thermo Fisher
Ultrasonics Sonifier Modell 250	Branson
Elexsys E580 Q-Band Pulsed Spectrometer	Bruker
EMXNano Benchtop Spectrometer	Bruker
Microbiological incubator Heratherm	Thermo Fisher
Electrophoresis chamber Mini Gel Tank	Thermo Fisher
Spectrophotometer NanoDrop	Thermo Fisher
Balance PM4800 DeltaRange	Mettler
Ultracentrifuge L7-65	Beckman

3.1.7 Buffers and solutions

Table 3.4. List of buffers and stock solutions used in this work.

Solution	Composition
Competent cell solution I	100 mM RbCl 50 mM $MnCl_2$ 30 mM potassium acetate 10 mM $CaCl_2$ 15 % (w/v) glycerol
Competent cell solution II	10 mM MOPS 10 mM RbCl 75 M $CaCl_2$ 15 % (w/v) glycerol
LB medium	10 g/l tryptone 10 g/l NaCl 5 g/l yeast extract
HEPES buffer	20 mM HEPES 300 mM NaCl pH 7.5
TSK buffer	20 mM HEPES 150 mM NaCl pH 7.2
Purification buffer	HEPES buffer 1 % (w/v) β-DDM
Washing buffer	HEPES buffer 50 mM imidazole: 0.05 % (w/v) β-DDM 2.2 µl β-ME
Elution buffer	HEPES buffer 300 mM imidazole: 0.05 % (w/v) β-DDM
Sample buffer	TSK buffer 0.05 % (w/v) β-DDM
Malachite green solution	2.6 mM malachite green chloride 0.17 % (w/v) Tween 1.5 % (w/v) Na_2MoO_4

Table 3.4. Continuation

Solution	Composition
5x SDS loading dye	250 mM Tris HCl pH 8.0 10 % (w/v) SDS 30 % (w/v) glycerol 10 mM DTT 0.05 % (w/v) bromophenol blue

3.1.8 Primers for side-directed mutagenesis

Table 3.5. List of primers for SDM used in this work.

Product	Substrate	Primer	Primer Sequence
L458C^{B}	A416C^{A}-L458C^{B}	C416A^{A} forward	GAGGGGGGCCGTCTTCTTGGAC
		C416A^{A} reverse	TGGGGGTCGTAGAAGCGGG
V288C^{A} -V461C^{A} -E272C^{B}	V288C^{A}-E272C^{B}	V461C^{B} forward	TTTGACCCCAGCTGTCCCCC
		V461C^{B} reverse	GAGGCGCAGGTTGTCCAGG
TmrA^{EQ}B mutations	V288C^{A}-E272C^{B}, V288C^{A} -V461C^{A} -E272C^{B}	E523Q^{A} forward	TCCTGGACCAGGCCACG
		E523Q^{A} reverse	TGAGGAGGATGTCGGGGC

3.1.9 Primers for sequencing of TmrAB

Table 3.6. List of primers for sequencing used in this work.

Primer	Sequence
Sequence Primer TmrA	TGGAGATCATCCGCTGGTTC
Sequence Primer TmrB	GGCCTGGTTCCAGGACCTGA

3.2 Methods

3.2.1 Competent cells

To generate chemocompetent cells, either from cell lines DH5α or BL21(DE3), the glycerol stock of the respective cells was cultivated in 50 mL LB medium at 37 °C overnight. Subsequently, 250 mL LB medium were inoculated with the primary culture to an optical density of OD_{600} < 0.1 and 10 mM $MgCl_2$ and 10 mM $MgSO_4$ were added. The secondary culture was incubated at 37 °C to an OD_{600} between 0.4 and 0.6 and transferred to ice for 15 min. Cells were harvested (5,000 × g, 10 min, 4 °C), resuspended in 100 ml competent cell solution I and equilibrated on ice for 10 min. Cells were pelleted (5,000 × g, 10 min, 4 °C), resuspended in 10 ml competent cell solution II and kept on ice for 30 min. Cells were aliquoted at 100 µl, frozen in liquid nitrogen, and stored at -80 °C.

3.2.2 Cloning of TmrAB variants and plasmid isolation

TmrAB cysteine variants and the E-to-Q mutant were prepared by site-directed mutagenesis using the Q5 Site-Directed Mutagenesis Kit according to manual. Forward and reverse primers for the respective mutations are listed in **Table 3.5**. After phosphorylation and ligation using the KLD enzyme mix included in the kit, SDM samples were added to chemically competent aliquots of *E. coli* DH5α for transformation. Samples were incubated for 1 h on ice and subsequently subjected to a heat shock at 42 °C for 90 s. After equilibration on ice for 10 min, 150 µl SOC medium was added and samples were incubated at 37 °C for 1 h. Samples were plated onto LB-agar plates with 100 µg/ml ampicillin added for selection and plates were incubated at 37 °C overnight. Colonies were separately picked and added into 5 ml LB medium with 100 µg/ml ampicillin added and incubated at 37 °C overnight. Plasmids were isolated from cells using the QIAprep Spin Miniprep Kit according to manual. Concentration of isolated plasmids was determined spectroscopically (Nanodrop) against a blank of H_2O. Plasmids were stored at -20 °C.

3.2.3 Expression of TmrAB

For expression of TmrAB variants, 2-4 µl isolated plasmid (according to plasmid concentration) was added to an aliquot of chemocompetent BL21(DE3) cells and incubated for 5 min on ice. Cells were subjected to heat shock at 42 °C for 30 s and equilibrated for 5 min on ice. Subsequently, 150 µl of LB medium was added and samples were incubated for 1 h at 37 °C. Samples were plated onto LB-agar plates with

100 µg/ml ampicillin added for selection and plates were incubated at 37 °C overnight. Colonies were separately picked and added into 150 ml LB medium with 100 µg/ml ampicillin added and incubated at 37 °C overnight. Precultured cells were added to 12 l of LB medium with 100 µg/ml ampicillin added and incubated at 37 °C. At an OD_{600} between 0.6 and 0.8, protein expression was induced by the addition of 0.5 mM isopropyl β-D-thiogalactopyranoside (IPTG). Expression was maintained for 4 h at 37 °C and cells were subsequently harvested by centrifugation.

3.2.4 Purification of TmrAB

Harvested cells were resuspended in HEPES buffer with 50 µg/ml lysozyme, disrupted by sonication and cell debris was removed by centrifugation at 13,500 × g for 15 min at 4 °C. Membranes were pelleted at 200,000 × g for 1 h at 4 °C and solubilized in 100 ml purification buffer for 1 h at 4°C. Insoluble components were removed by centrifugation at 200,000 × g for 30 min at 4 °C. Solubilized TmrAB was incubated with Ni-NTA Sepharose, 1 mM β-mercaptoethanol (β-ME) and 30 mM imidazole for 1 h at 4 °C. After washing with 25 ml of washing buffer, bound TmrAB was eluted with elution buffer in 12 fractions of 0.5 ml. The five fractions with the highest concentration were pooled and the buffer was exchanged to 3.5 ml sample buffer using an equilibrated PD-10 desalting column.

3.2.5 Spin-labeling of TmrAB and cw EPR spectroscopy

Single, double, and triple cysteine variants of TmrAB were labelled with a 40-fold molar excess of MTSL in sample buffer for 30 min at rt. The protein was concentrated using Vivaspin 6 filter concentrators with a cutoff of 50 kDa, free MTSL was removed by Micro Bio-Spin (Biorad). Labelling efficiency was determined by cw EPR measurements at X-band frequencies on a Bruker EMX Nano benchtop spectrometer with the following experimental parameters: 100 kHz modulation frequency, 1.5 G modulation amplitude, 1000 mW microwave power, 5.12 ms time constant, 22.5 ms conversion time and 150 G sweep width. The spin concentration was determined using the EMX Nano software.

3.2.6 SDS-Page

The quality of protein purification and the purity of protein samples were monitored by sodium dodecyl sulfate polyacrylamide gel electrophoresis (SDS-PAGE). Samples were prepared by mixing with SDS sample buffer and boiling at 99°C for 10 min. Subsequently, samples were applied on a 4-12% polyacrylamide gel in a

electrophoresis chamber filled with TEA-Tricine SDS Running Buffer at 180 V. SDS-PAGE gels were stained with Coomassie brilliant blue and imaged using a gel imager.

3.2.7 ATPase assay

ATPase activity of TmrAB was determined colorimetrically using a malachite green phosphate assay. All samples were prepared in sample buffer. Measurements were performed at final ATP concentrations of 0 mM, 0.0125 mM, 0.25 mM, 0.5 mM, 0.75 mM, 1 mM and 3 mM, and at a final concentration of 3 mM $MgCl_2$ and 600 nM TmrAB in a volume of 25 µl and carried out for 5 min at 37 °C. Reactions were stopped by adding 175 µl of an ice-cold aqueous solution of 20 mM H_2SO_4 and transferred to ice. For detection, 175 µl of a stopped reaction sample was transferred into a 96-well microtiter plate and incubated for 15 min with 50 µl of malachite green solution at room temperature. The absorbance change at 620 nm was measured on a microplate reader. As negative control, ATP auto hydrolysis was recorded in the absence of TmrAB und subtracted as background. P_i release was calculated from the absorbance using a standard curve of K_2HPO_4 (0 nmol, 0.4 nmol, 0.8 nmol, 2 nmol, 3.2 nmol, 4.8 nmol, 6 nmol) that was incubated with malachite green solution in an identical manner. All data are presented as mean ± s.d. (n = 3).

3.2.8 Sample preparation

All samples were prepared in sample buffer.

3.2.8.1 Samples to establish distance restraints

To obtain the distance restraints for the analysis of PELDOR signals with a bimodal Gaussian parametric distribution, 50 µM TmrAB was prepared either under apo-conditions (15 % deuterated glycerol), or as ADP-VO_4^{3-}-Mg^{2+} trapped state (10 mM ATP, 10 mM Na_3VO_4, 10 mM $MgCl_2$, 15 % deuterated glycerol, 50 °C, 5 min), and frozen in liquid nitrogen.

3.2.8.2 Time-resolved PELDOR samples

For the kinetic investigation of TmrAB, samples were prepared in a time-resolved manner. To exclude ATP hydrolysis from the considerations, samples were prepared under ATP-EDTA conditions (50 µM TmrAB, 50 mM ATP, 0.5 mM EDTA), and aliquoted. To time-resolve the conformational transitions with ATP hydrolysis taking place, samples were prepared under ATP-Mn^{2+} conditions (50 µM TmrAB, 50 mM ATP or ATPγS, 50 mM $MgCl_2$), and aliquoted. Aliquots were kept at 10 °C for up to 10 min.

Aliquots were transferred to preheated quartz tubes and incubated at increasing temperatures (30 °C, 40 °C, 50 °C) for increasing periods of time (10 s, 20 s, 40 s, 80 s, 160 s, 300 s) and frozen immediately in liquid nitrogen.

3.2.8.3 NO-Mn^{2+} PELDOR samples

For the NO-Mn^{2+} experiments, samples were prepared under ATP-Mn^{2+} conditions (65 µM TmrAB, 10 mM ATP, 10 mM $MnCl_2$, 15 % glycerol) or ADP-VO_4^{3-}-Mn^{2+} conditions (65 µM TmrAB, 10 mM ATP,10 mM Na_3VO_4, 10 mM $MnCl_2$, 15 % glycerol) and incubated at 50 °C for 5 min. Free Mn^{2+} was removed by Micro Bio-Spin equilibrated with TSK buffer and 10 mM ATP. After buffer exchange, samples were prepared by adding 15 % deuterated glycerol and frozen in liquid nitrogen.

3.2.8.4 Time-resolved NO-Mn^{2+} PELDOR samples

For the time-resolved NO-Mn^{2+} experiments, samples were prepared under ATP-Mn^{2+} conditions (65 µM TmrAB, 10 mM ATP, 10 mM $MnCl_2$, 15 % glycerol) and incubated at 50 °C for 5 min. Free Mn^{2+} and ATP was removed by Micro Bio-Spin equilibrated with TSK and 0.5 mM EDTA. After buffer exchange, samples were prepared by adding 15 % deuterated glycerol and frozen immediately in liquid nitrogen or transferred to preheated quartz tubes, incubated at 50 °C for 80 s or 300 s and frozen.

3.2.8.5 Reverse transition samples

For the time-resolved reverse transition PELDOR experiments, samples were prepared under ATP-EDTA conditions (50 µM TmrAB, 50 mM ATP, 0.5 mM EDTA), and incubated at 50 °C for 5 min. ATP was removed by Micro Bio-Spin equilibrated with TSK buffer and either 0.5 mM EDTA, 50 mM $MgCl_2$, 10 mM ADP or 50 µM K5F. Samples were prepared by adding 15 % deuterated glycerol, transferred to preheated quartz tubes, incubated at 50 °C for 80 s, 160 s or 5 min, and frozen in liquid nitrogen.

3.2.9 PELDOR spectroscopy

For PELDOR measurements, two spectrometer systems were employed: (1) a Bruker Elexsys E580 Q-Band pulsed EPR spectrometer equipped with an arbitrary waveform generator (SpinJet-AWG), a continuous-flow helium cryostat, a temperature control system (Oxford Instruments), a 50 W solid state amplifier, and a Bruker EN5107D2 dielectric resonator. (2) a Bruker Elexsys E580 Q-band pulsed EPR spectrometer equipped with an arbitrary waveform generator (SpinJet-AWG), a

continuous-flow helium cryostat, a temperature control system (Oxford Instruments), a 150 W TWT amplifier (Applied Systems Engineering Inc.) and a Bruker EN5107D2 cavity.

3.2.9.1 NO-NO PELDOR

Depending on the spectrometer system, different measurement setups were chosen. In (1), EDFS spectra and T_M measurements were performed at 50 K for nitroxide using the two pulse Hahn echo sequence as described in chapter 1.4.5.3 employing Gaussian pulses (32 ns or 48 ns) with an inter-pulse delay τ of 200 ns. The four-pulse PELDOR experiments were recorded using Gaussian pulses and a dead-time free sequence employing a 16-step phase cycling (x[x][xp]x). NO-NO measurements were acquired at 50 K using a 38 ns pump pulse and 48 ns observer pulses. The pump pulse was set to the maximum of the EDFS spectrum, while the observer pulses were set at 80 MHz lower (see **Figure 3.2a**), and the shot repetition time (SRT) was kept at 2 ms. In (2), EDFS spectra and T_M measurements were performed at 50 K using the two pulse Hahn echo sequence employing rectangular pulses (16 ns and 32 ns for $\pi/2$ and π pulse, respectively) with an inter-pulse delay τ of 200 ns. A rectangular 12 ns pump, and a 16 ns $\pi/2$ and 32 ns π observer pulse were employed with 80 MHz separation, which gave a similar modulation depth in comparison to the Gaussian pulses employed in spectrometer system (1).

The five-pulse PELDOR/DEER experiments were performed according to the pulse sequence described in chapter 1.4.6.2 with δ set to 200 ns. Experiments were performed at 50 K using 48 ns Gaussian observer pulses and 16-step phase cycling (xxp[x][xp]x). A 36 ns standing and a 48 ns moving Gaussian pump pulse was used.

3.2.9.2 Mn^{2+}-NO and Mn^{2+}-Mn^{2+} PELDOR

For Mn^{2+}-NO and Mn^{2+}-Mn^{2+} PELDOR measurements, spectrometer setup (1) was used. Echo-detected ESR spectrum and T_M measurements were performed at 5 K for Mn^{2+} using the two pulse Hahn echo sequence as described in chapter 1.4.5.3 employing Gaussian pulses (32 ns or 48 ns) and an inter-pulse delay τ of 200 ns. The four-pulse PELDOR experiments were recorded using a dead-time free sequence employing Gaussian or Chirped pump and observer pulses and a 16-step phase cycling (x[x][xp]x). Mn^{2+}-NO PELDOR experiments were recorded at 5 K while pumping the nitroxide and observing the Mn^{2+}, with the observer pulses set at 248.4 MHz lower than the pump pulses (see **Figure 3.2b**), the pulse length and shapes are listed in **Supplementary Table S1**. The SRT was kept at 1 ms. Mn^{2+}-Mn^{2+} PELDOR experiments

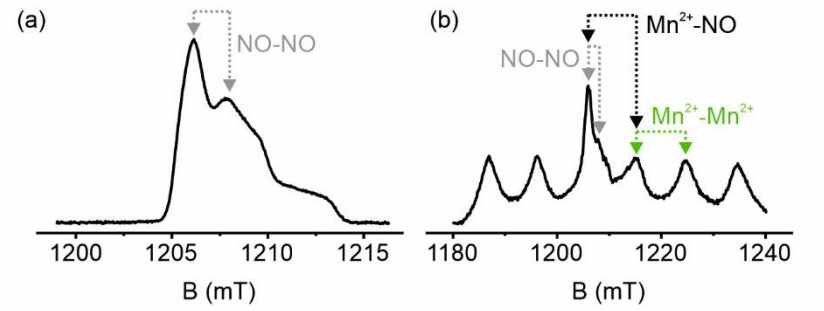

Figure 3.2. EDFS spectra of TmrAB. (a) EDFS spectrum of TmrAB with two MTSL spin labels attached at positions V288C^{A} – E272C^{B}. Sample prepared under apo conditions and measured with a Hahn echo sequence as described in the text. (b) EDFS spectrum of TmrAB with one MTSL spin label attached at position A416C^{A}. Sample prepared with ATP-Mn^{2+} as described under 3.2.9.3 and measured with a Hahn echo sequence as described in the text. The arrows indicate the positions of the pump pulse at the pump frequency ω_B (left end of the arrow) and the observer pulse at the observer frequency ω_A (right end of the arrow).

were recorded at 5 K using a 20 ns pump and a 24 ns observer gaussian pulse. The observer pulses were set at 259 MHz lower than the pump pulses (see **Figure 3.2b**).

3.2.10 Data analysis and simulations

Distance distributions were determined using DeerLab, see chapter 1.4.8. The primary data were simultaneously fitted for the distances and the background function using a non-parametrized model with Tikhonov regularization or a Gaussian model-based approach as indicated. For the non-parametrized analysis, the extracted distance distribution is shown with a 95 % confidence interval. The distances (mean and width) of the model Gaussians were determined by measuring the samples prepared according to chapter 3.2.8.1 and analyzing them using a non-parametrized model with Tikhonov regularization. For the Gaussian model-based analysis, linear combination of the Gaussian peaks to fit the original data yields the probabilities of the respective distances and thus conformational states. A 95 % confidence interval is given to show the goodness of the fit, likewise the values for the distance probabilities are given with a 95 % confidence interval as error. For related data sets, a global analysis was performed using DeerLab. For the NO-NO 5-pulse analysis, DeerLab was

used, and the primary data were simultaneously fitted for the distances and the background function using a non-parametrized Tikhonov regularization approach in a global analysis together with the time trace of a four-pulse PELDOR measurement of the same sample.

Simulations of the NO-NO distance distributions between MTSL spin labels were obtained on the structures of TmrAB in its IF conformation (PDB 5MKK and 6RAG), in its OF conformation (PDB 6RAJ and RAH), OF-occluded (PDB 6RAI) using the rotamer libraries for MTSL as implemented in the MATLAB-based software package MMM2022.2. For simulations of Mn^{2+}-NO distance distributions, rotamer libraries for MTSL were calculated for single MTSL labelled variants of TmrAB in the IF and OF conformation. The distances between these simulated rotamer libraries and the Mg^{2+} ions resolved in the respective cryo-EM structures were measured using PyMOL 2.4.1 and plotted as histograms to obtain the distance distributions.

3.2.11 Kinetic model and Arrhenius plot fitting

The fitting of data points, either according to a kinetic model as explained, or by linear regression, was performed in OriginPro 2023b 10.0.5.157. The equation of the kinetic model was fitted using the Levenberg-Marquardt algorithm to solve non-linear least squares problems with an instrumental weighing of the input errors. Linear regression was performed with an instrumental weighing of the input error.

4 RESULTS

4.1 Biochemical characterization of TmrAB

4.1.1 Protein purification and yield

The TmrAB variants carrying the respective cysteine point mutations for SDSL were expressed and purified consistently according to the methods described in chapter 3.2. Protein purity was monitored over the course of the protein purification procedure by SDS-PAGE, as exemplified by the purification of TmrAB WT*(see chapter 3.1.1) in **Figure 4.1**. Impurities could be largely removed, and TmrAB was eluted in few fractions of elution buffer. During SDS-PAGE, the majority of TmrAB dissociated into monomers of TmrA and TmrB, with only a small fraction remaining as intact TmrAB heterodimer. This leads to the characteristic three bands in the stained SDS-PAGE gel.

The yield of pure protein depended slightly on the position of cysteine substitutions and varied between expressions. Usually, 15 to 20 nmol of TmrAB were obtained from one expression in 12 l LB medium. Since samples are prepared with a final TmrAB concentration of 50 µM and a sample volume of up to 20 µM, several expressions were necessary to purify a sufficient amount of protein for the large number of time-resolved samples (see chapter 4.2).

4.1.2 Spin labelling

Purified TmrAB variants were labelled with MTSL, and the quality of spin labelling was assessed by cw EPR spectroscopy. As explained in chapter 1.4.4.2, the characteristic degree of mobility of the MTSL spin label that corresponds to the position of MTSL in TmrAB resulted in distinct spectral shapes for each labelled variant. Furthermore, free, unbound MTSL would lead to a superposition of the spectral contributions of TmrAB-bound and free MTSL, i.e. the appearance of the narrow lines corresponding to the isotropic limit of a nitroxide radical. Since free MTSL is unwanted because it contributes to the background decay, its absence was monitored. For all spin-labelled variants of TmrAB used in this work, free MTSL could be completely removed, as seen from the respective spectra in **Supplementary Figure S1**.

The spin concentration of MTSL labelled variants of TmrAB was calculated from the area of the integral of the cw EPR spectra. The spin concentration divided by the number of attached spin labels was divided by the protein concentration to obtain the labelling efficiency, which was usually between 80-100 %.

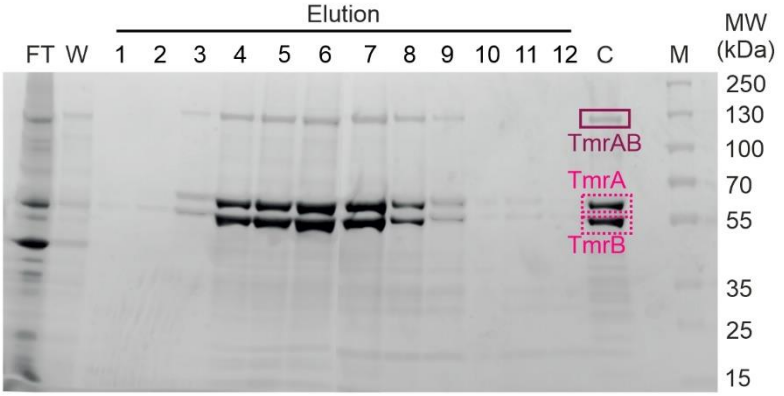

Figure 4.1. SDS-PAGE analysis of TmrAB WT* over the course of its purification. Samples were taken after the DDM-solubilized membrane fraction was subjected to IMAC: the flow-through (FT); wash with washing buffer (W); elution with elution buffer in 12 fractions, from which five fractions (4 – 8) were combined, desalted, labelled, and concentrated (C). The marker (M) with the respective bands for reference is indicated.

4.2 Kinetic analysis of TmrAB using time-resolved PELDOR spectroscopy

4.2.1 Design and spin labelling of TmrAB cysteine variants

Based on the available biochemical, biophysical, and structural data, ATP binding itself was identified to be the power stroke for the IF-to-OF transition and substrate translocation in TmrAB.[210] To independently monitor the kinetics of the NBSs and the TMDs, pairs of cysteine substitutions were engineered at strategic positions. These pairs monitor the TMDs (V288C^{A}–E272C^{B}), the consensus NBS (c-NBS, A416C^{A}–L458C^{B}), and the degenerate NBS (d-NBS, V461C^{A}–D349C^{B}), respectively (**Figure 4.2**). All these variants actively hydrolyzed ATP, as was recently shown.[207] These cysteines were labelled using MTSL and the interspin distances were determined using four-pulse PELDOR spectroscopy. Simulations showed that these positions have well resolved distances between the IF and OF conformations. In order to quantify the fractions of IF and OF conformation in the time-resolved TmrAB samples, a two Gaussian parametrized fitting approach with the interspin distances of the respective spin pairs in the IF and OF conformation as distance restraints was used. For the IF conformation, a sample of TmrAB under apo conditions was prepared and measured. TmrAB was trapped in the OF conformation by preparing a vanadate-trapped sample (50 µM TmrAB, 10 mM ATP, 10 mM Na_3VO_4, 10 mM $MgCl_2$) and incubating at 50 °C for 5 min. After hydrolysis of the γ-phosphate of ATP in presence of magnesium ions, the VO_4^{3-} anion replaces this terminal phosphate and mimics the transition state during ATP hydrolysis, thus trapping ADP at the NBS and retaining the transporter in the OF conformation.[211] For the TMDs, the apo sample was measured by four-pulse PELDOR and analyzed using a model-free Tikhonov regularization approach, and the interspin distance of the IF state was determined as $r_{IF} = 3.6 \pm 0.3$ nm. Since for the OF state a longer distance is to be expected, the vanadate-trapped sample was measured by four- and five-pulse PELDOR and analyzed with Tikhonov regularization using the global analysis approach as described in chapter 1.4.8.4 to obtain a more accurate distance distribution. The long distance corresponding to the OF state was determined as $r_{OF} = 5.6 \pm 0.3$ nm. Both distances largely agree with the simulated interspin distances (**Figure 4.3a,b**). For the c-NBS and d-NBS, the distance restraints were determined in the same manner in an earlier publication.[207] The open conformation of the c-NBS spin pair was determined as $r_{open} = 5.7 \pm 0.3$ nm and the closed conformation as $r_{closed} = 3.8 \pm 0.4$ nm. At the d-NBS, the distance of the open conformation was determined as $r_{open} = 3.9 \pm 0.5$ nm and the closed conformation

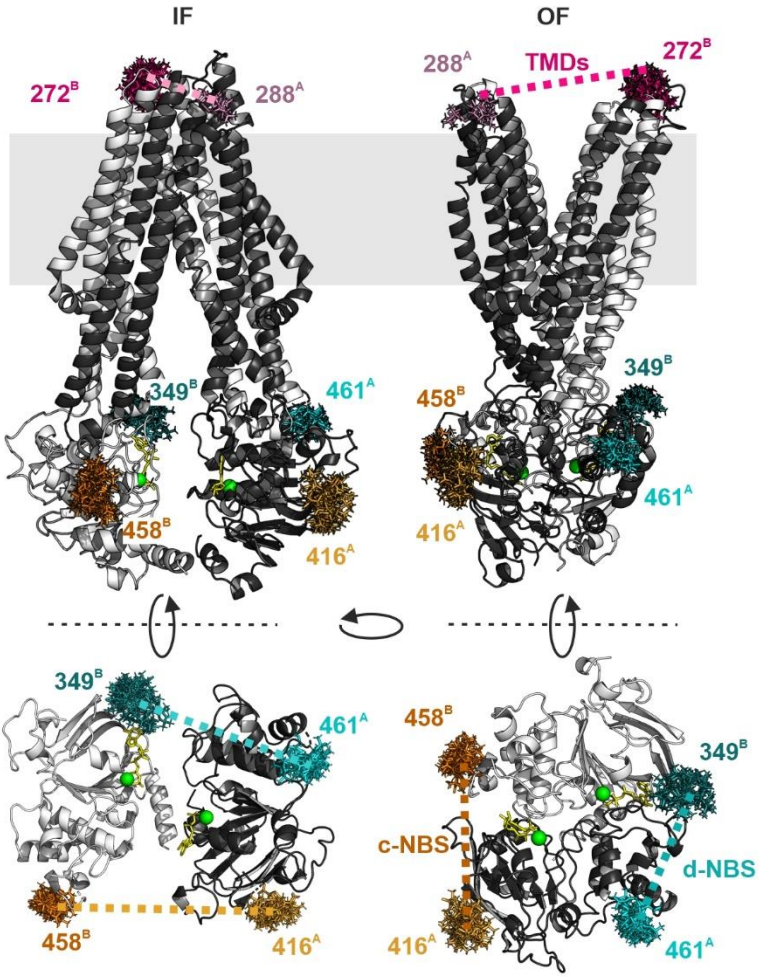

Figure 4.2. MTSL double-labelled variants of TmrAB. MTSL labeled positions are indicated at the NBDs and TMDs in the IF (PDB: 6RAG) or OF (PDB: 6RAJ) conformation in the full-length transporter (top) and in the isolated NBDs in a view from the membrane towards the cytoplasm (bottom). The Mg^{2+} ion at the NBSs (green) as well as ATP (yellow) are highlighted. TmrA (black), TmrB (grey). For better visibility, the OF conformation is rotated by 90° clockwise along the vertical axis.

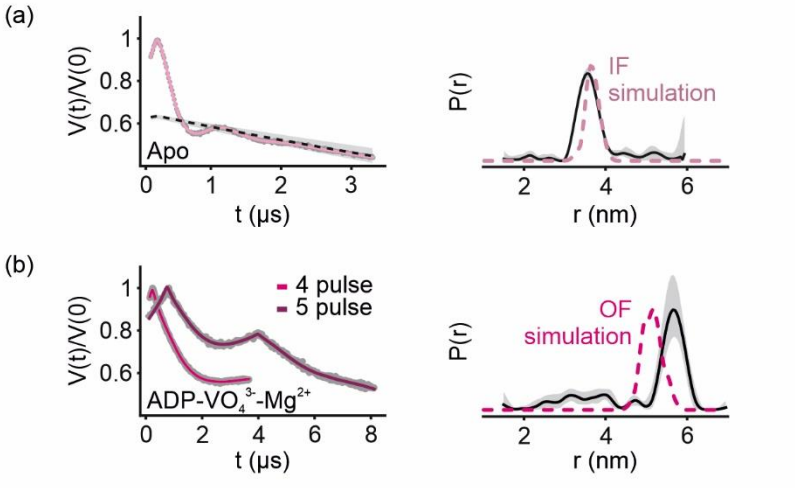

Figure 4.3. Determination of distance restraints for the TMDs. To investigate the conformational transitions at the TMDs, the MTSL labelled variant V288R1^{A}–E272R1^{B} was chosen. PELDOR time traces V(t) on the left, resulting distance distributions P(r) on the right. (a) To determine the interspin distance in the IF conformation, an apo sample of TmrAB was measured by four-pulse PELDOR and analyzed by Tikhonov regularization. (b) To determine the interspin distance in the OF conformation, a vanadate-trapped sample of TmrAB (10 mM ATP, 10 mM Na_3VO_4, 10 mM $MgCl_2$, 50 °C for 5 min) was measured by four- and five-pulse PELDOR and analyzed in a global manner by Tikhonov regularization. The simulated interspin distances based on cryo-EM structures are overlayed in pink dashed lines.

as r_{closed} = 3.1 ± 0.4 nm. In addition, an invariant contribution with a fraction of approximately 0.1 was present with r_{fix} = 6.0 ± 0.5 nm that could correspond to a small number of aggregates. The time-resolved PELDOR data were fitted using a linear combination of these two (or three, in the case of the d-NBS) Gaussian distances for each labelled variant. Data analysis was performed using the global analysis approach described in chapter 1.4.8.4. The amplitude of the Gaussian components could be biased and needs to be manually corrected when the transversal relaxation time (measured by the phase memory time T_m) of the spins is different between the conformational states. In the case of these three spin label pairs, the T_m was unaltered during the IF-to-OF transition. The thus obtained distance amplitudes correspond to the fractions of the two distances of the distance restraints and enabled precise quantification of the corresponding populations. Analyzing the time-resolved PELDOR

data in the above mentioned way hence gave us information about the time-dependent change in the respective populations.

4.2.2 Time-resolved sample preparation

TmrAB shows ATPase and transport activity over a broad temperature range (30 – 70 °C) with a maximum activity close to 68 °C.[212] From previous observations of other ABC transporters, we reasoned that at lower temperatures (30 – 50 °C), the IF-to-OF transition in TmrAB might take longer without changing the underlying thermodynamics of the system. This would allow for the preparation of time-resolved samples without an RFQ setup. Samples were prepared as a stock and equilibrated at 10 °C. Equilibrated aliquots were successively transferred into pre-heated EPR quartz tubes immersed in a water bath (at 30 °C, 40 °C, or 50 °C as required). The preincubation at 10 °C resulted in a fraction of the transporters ($P_{OF} = 0.15$) switching to the OF conformation (**Supplementary Figure S2**). This population was taken into account for the kinetic analysis. The sample was incubated for 10 s, 20 s, 40 s, 80 s, 160 s or 300 s at each of the temperatures. Calibration temperature measurements confirmed that the samples in the quartz tube reached the required temperature (30 – 50 °C) within 2 - 3 s. This was followed by immediate freezing in liquid nitrogen, which freezes the sample within 1 s. The sample transfer itself takes 1 s, which would have minimal effect on the observed transition which takes a few minutes to reach the equilibrium. A prolonged incubation at 4 °C or a second incubation at lower temperature does not affect the population of the IF and OF conformation (**Supplementary Figure S3**), revealing large enough energy barriers between the states and showing that transfer or freezing delays on the seconds timescale do not alter the populations significantly.

4.2.3 Time-resolved observation of the TMDs

First, we investigated the periplasmic gate at the TMDs with the variant V288R1^{A}–E272R1^{B}. We initially wanted to observe the change of the conformational equilibrium induced by the binding of ATP alone, prior to ATP hydrolysis taking place. Thus, we incubated the samples with ATP and EDTA (50 mM and 0.5 mM, respectively) for an incremental time at 30 °C. Our model-based analysis based on the two distances for the IF (peak at $r_{IF} = 3.6 \pm 0.3$ nm) and OF (peak at $r_{OF} = 5.6 \pm 0.3$ nm) conformation revealed a distance distribution between the IF and the OF states (**Figure 4.4a**), again proving that ATP binding is the key step for the IF-to-OF transition in ABC exporters. Notably, we observed a gradual increase of the OF population (P_{OF})

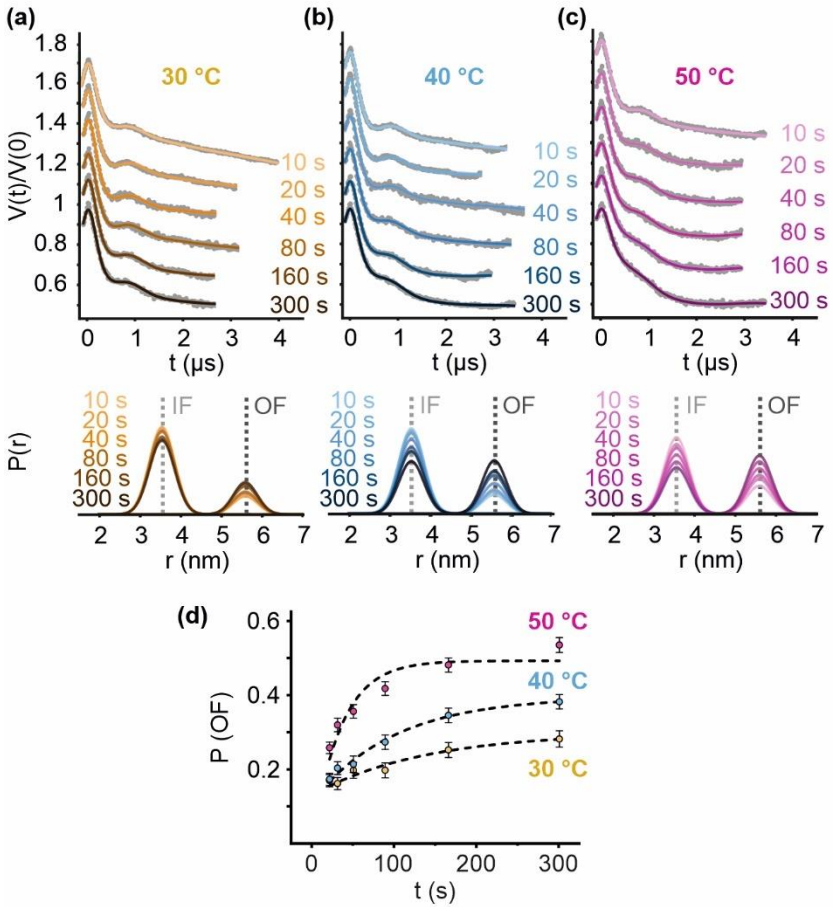

Figure 4.4. TR-PELDOR at the TMD double cysteine variant V288R1^{A}–E272R1^{B}. TmrAB was incubated with ATP-EDTA at (a) 30 °C, (b) 40 °C and (c) 50 °C for increasing time steps between 10 s and 300 s and immediately frozen in liquid nitrogen. Primary PELDOR data V(t)/V(0) overlaid with the fit are shown. Data were globally analyzed using DeerLab. An experimentally determined two Gaussian model corresponding to the IF and OF conformation was used for the analysis. The obtained distance distributions P(r) with a 95% confidence interval are shown. (d) The populations of the OF conformation are plotted as a function of time for different temperatures and fitted based on a first order reversible transition as explained in chapter 4.2.5 (dashed lines). Error bars are 95% confidence interval (CI).

with a corresponding decrease in the IF population ($1 - P_{OF}$) over time. We performed additional time-resolved measurements at 40 °C and 50 °C. The data sets were globally analyzed to observe the temperature dependence of the IF-to-OF transition. At higher temperatures, this time-resolved shift from the IF to the OF state is more pronounced (**Figure 4.4b,c**), and we see that with higher temperatures both the rate and the magnitude of this transition are enhanced. The model-based analysis resulted in good fitting of the primary data for all temperatures and time points. Biological replicates (i.e., repetitions of the sample preparation and measurement based on a different protein expression and purification) yielded very similar values and the fractions of IF and OF state for the results shown here as well as the replicates can be found in the appendix (**Supplementary Table 2**). The population of the OF state of each sample was plotted as a function of the incubation time (**Figure 4.4d**) to visualize the temperature and time dependence. These observations reveal that the IF-to-OF transition in presence of ATP is a thermically activated process.

4.2.4 Comparison of TMD opening and NBS closure

We repeated the time-resolved experiment in presence of ATP-EDTA with a focus on the NBSs. The variant that was chosen to observe the c-NBS (A416R1^{A}–L458R1^{B}) revealed a shift of the distance distribution from the longer distance that corresponds to the open conformation of the c-NBS ($r_{open} = 5.7 \pm 0.3$) to the short distance that corresponds to the closed, dimerized conformation of the c-NBS ($r_{closed} = 3.8 \pm 0.4$ nm) (**Figure 4.5a-c**). The closed population increased over time with a corresponding decrease in the open population. Analogously to the TMDs, this trend increased with an increase of the temperature. The model-based analysis could fit the PELDOR time traces well for all temperatures and time points. The fractions of open and closed conformations are shown in the appendix (**Supplementary Table 3**) and were reproducible. The populations of the closed conformation of the c-NBS are plotted as a function of time (**Figure 4.5d**).

For the spin pair reporting the d-NBS (V461R1^{A}–D349R1^{B}), the model-based analysis could fit the primary data well but gave larger errors for the resulting fractions of open and closed conformations. This is likely because the closed conformation with $r_{closed} = 3.1 \pm 0.4$ nm and the open conformation with $r_{open} = 3.9 \pm 0.5$ nm are closer than for the cases of TMDs and c-NBS, giving more uncertainty for the fitting. The results of the d-NBS should thus be taken with a grain of salt, but they shows a similar behavior to the c-NBS, with an increase of the short distance corresponding to the closed conformation and a decrease of the long distance corresponding to the open conformation over time (**Figure 4.6a,b**). However, the amplitude of NBS closure

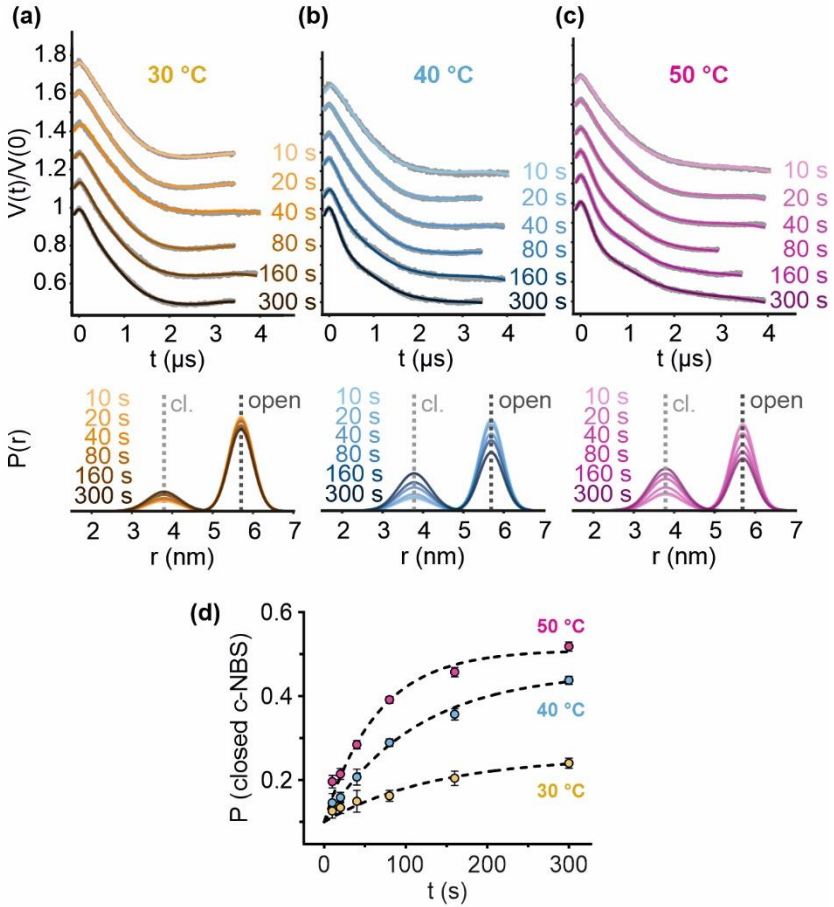

Figure 4.5. TR-PELDOR at the c-NBS double cysteine variant A416R1^{A}–L458R1^{B}. TmrAB was incubated with ATP-EDTA at (a) 30 °C, (b) 40 °C and (c) 50 °C for increasing time steps between 10 s and 300 s and immediately frozen in liquid nitrogen. Primary PELDOR data V(t)/V(0) overlaid with the fit are shown. Data were globally analyzed using DeerLab. An experimentally determined two Gaussian model corresponding to the open and closed (cl.) conformation was used for the analysis. The obtained distance distributions P(r) with a 95% confidence interval are shown. (d) The populations of the closed conformation at each temperature and time point are plotted as a function of time and fitted based on a first order reversible transition as explained in chapter 4.2.5 (dashed lines). Error bars are 95% CI.

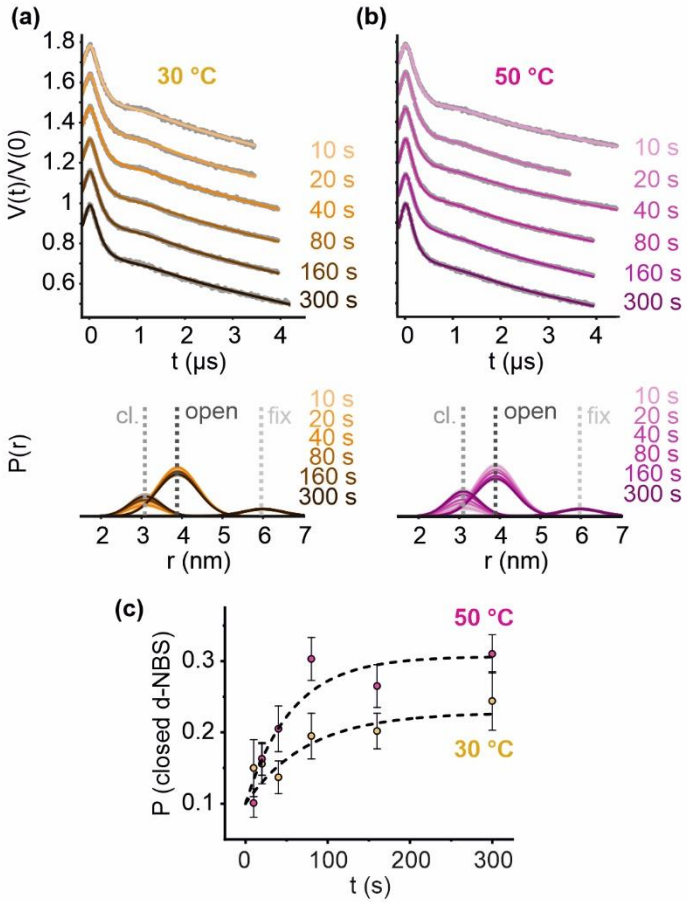

Figure 4.6. TR-PELDOR at the d-NBS double cysteine variant V461R1^{A}–D349R1^{B}. TmrAB was incubated with ATP-EDTA at (a) 30 °C and (b) 50 °C for increasing time steps between 10 s and 300 s and immediately frozen in liquid nitrogen. Primary PELDOR data V(t)/V(0) overlaid with the fit are shown. Data were globally analyzed using DeerLab. An experimentally determined three Gaussian model corresponding to the open and closed (cl.) conformation, as well as a minor invariable fraction (fix) was used for the analysis. The obtained distance distributions P(r) with a 95% confidence interval are shown. (c) The populations of the closed conformation at each temperature and time point are plotted as a function of time and fitted based on a first order reversible transition as explained in chapter 4.2.5 (dashed lines). Error bars are 95% CI.

is reduced, with a maximum fraction of the closed state of 0.32 ± 0.13 versus 0.51 ± 0.01 at the c-NBS. The fractions of open and closed conformations are shown in the appendix (**Supplementary Table 3**). The populations of the closed conformation of the c-NBS are plotted as a function of time (**Figure 4.6c**).

4.2.5 Kinetic model gives rate constants and activation energy

To quantitatively compare the rate constants for the conformational transition at different regions of TmrAB, we defined a four-state kinetic model (A-D in **Figure 4.7**). Under our experimental conditions (50 µM TmrAB, 50 mM ATP and 0.5 mM EDTA), ATP binding should be a fast process and TmrAB will exist predominantly in the ATP bound form. We did not observe the IF-to-OF transition in the absence of ATP, therefore the transitions between A and D, or C and D were excluded. With these assumptions, the IF-to-OF transition at the TMD variant becomes a first order reversible transition between the IF_{ATP} (B) and OF_{ATP} (C) states, and our experimentally determined populations P_{IF} and P_{OF} could be defined as the relative concentrations of IF_{ATP} and OF_{ATP}, respectively. The concentration balance equation for the OF_{ATP} state is then

$$\frac{dP_{OF}}{dt} = k_1 P_{IF} - k_{-1} P_{OF} \tag{4.1}$$

From the boundary condition that P_{IF} and P_{OF} at all times add up to 1 follows

$$P_{IF} + P_{OF} = P_{IF,0} + P_{OF,0} \tag{4.2}$$

and insertion into eq 4.1 leads to a differential equation with only one variable and the starting concentrations $P_{IF,0}$ and $P_{OF,0}$

$$\frac{dP_{OF}}{dt} = k_1(P_{IF,0} + P_{OF,0} - P_{OF}) - k_{-1} P_{OF} \tag{4.3}$$

As described in chapter 4.2.2, we saw a stable fraction of $P_{OF} = 0.15$ after sample equilibration at 10 °C, after which the incubation at the designated temperatures (30 °C, 40 °C, 50 °C) was initiated. We therefore set the starting populations of IF and OF as $P_{IF,0} = 0.85$ and $P_{OF,0} = 0.15$. By solving the differential equation from eq 4.3, the analytical solution for P_{OF} is obtained as

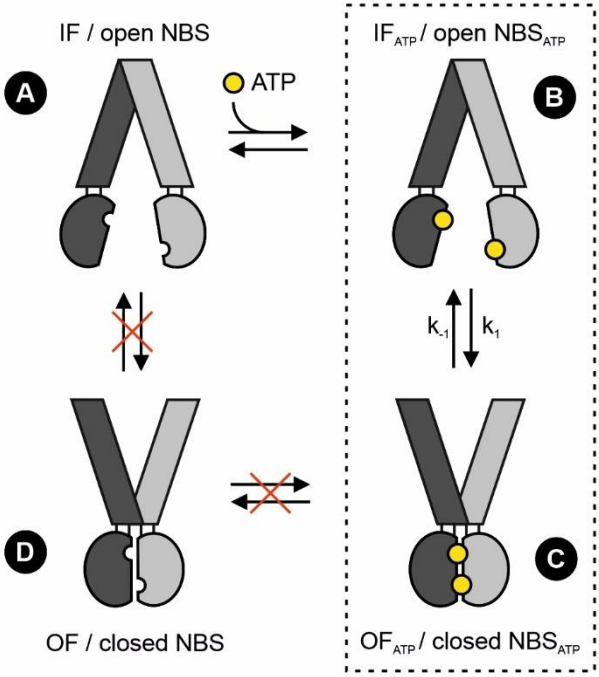

Figure 4.7. Kinetic model for the conformational transition in TmrAB. The transition from the ATP-bound transporter in the inward-facing conformation IF_{ATP} (B) to the ATP-bound transporter in the outward-facing conformation OF_{ATP} (C) is assumed to be the rate-limiting step with the rate constants k_1 and k_{-1} for the forward and reverse transition, respectively.

$$P_{OF}(t) = \frac{k_1}{k_1 + k_{-1}} P_{IF,0}\{1 - exp[-(k_1 + k_{-1})t]\} + \frac{1}{k_1 + k_{-1}} P_{OF,0}\{k_1 + k_{-1} exp[-(k_1 + k_{-1})t]\} \quad (4.4)$$

For the observation of the NBSs, the identical equation is used, with the experimentally determined populations of the open and closed conformation of the NBSs (P_{open} and P_{closed}, respectively)

$$P_{closed}(t) = \frac{k_1}{k_1 + k_{-1}} P_{open,0}\{1 - exp[-(k_1 + k_{-1})t]\} + \frac{1}{k_1 + k_{-1}} P_{closed,0}\{k_1 + k_{-1} exp[-(k_1 + k_{-1})t]\} \quad (4.5)$$

We fitted the time-resolved data points with our kinetic model from eq 4.4 and 4.5 (dashed lines in **Figure 4.4d, 4.5d, 4.6c**). The goodness-of-fit was characterized by good corrected R^2 values between 0.87 and 0.97 for the TMDs and c-NBS, and between 0.6 and 0.87 for the d-NBS. From these fits we obtained the rate constants and their temperature dependence for these transitions (**Table 4.1**). As expected for the TMDs, the rate constant for the forward transition increased with increasing temperature, as did the rate constant for the reverse transition k_{-1}. For the c-NBS, the same overall behavior can be seen. The values for the d-NBS have larger errors but

Table 4.1. Rate constants of the conformational transition in TmrAB. The rate constants for the forward (k_1) and reverse (k_{-1}) transition of TmrAB at the TMDs, c-NBS, d-NBS and at the TMDs in the catalytically impaired E-to-Q variant. Values given with 95% CI.

	T (°C)	k_1 ($\times 10^{-3}$ s^{-1})	k_{-1} ($\times 10^{-3}$ s^{-1})
TMDs	30	2.85 ± 0.87	6.73 ± 2.80
	40	4.43 ± 0.60	6.52 ± 1.23
	50	15.12 ± 3.16	14.55 ± 4.15
c-NBS	30	1.87 ± 0.39	5.44 ± 1.61
	40	4.11 ± 0.25	4.86 ± 0.49
	50	7.81 ± 0.63	7.5 ± 1.00
d-NBS	30	3.05 ± 1.30	10.34 ± 5.76
	50	5.49 ± 1.81	12.40 ± 5.20
TMDs E-to-Q	30	4.96 ± 0.27	5.01 ± 0.49
	40	40.70 ± 5.94	23.19 ± 4.82
	50	99.51 ± 11.05	52.22 ± 6.82

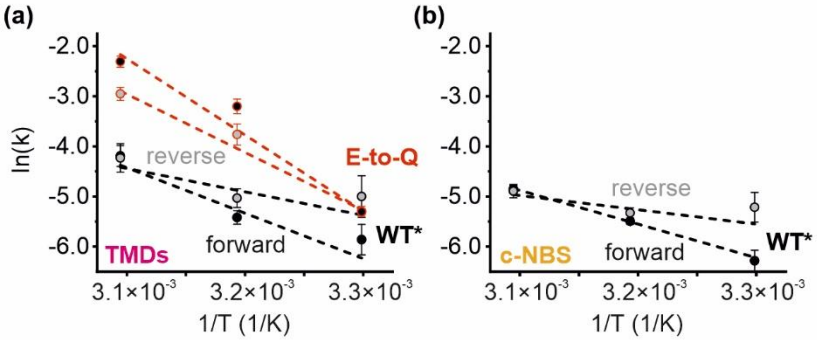

Figure 4.8. Arrhenius plots for the conformational transition in TmrAB. The time-resolved PELDOR data from the labelled variants in the Cys-less (WT*) background at the TMDs (a) and the c-NBS (b) were fitted with a two-state reversible model and the resulting rate constants for the forward and reverse transition (see **Table 4.1**) were analysed according to Arrhenius equation. In (a), the influence of the E-to-Q mutation on the kinetics is compared to the WT* background. Error bars are 95% CI.

are comparable within the margin of error. We next wanted to analyze the temperature dependence of these rate constants to obtain the activation energy of the conformational transition. Since only two temperatures were measured for the d-NBS, an Arrhenius analysis of the d-NBS was not performed. The temperature-dependent rate constants for the forward and reverse transition were plotted in an Arrhenius plot as $ln\,k$ as a function of $1/T$ (black circles in **Figure 4.8a,b**). The slope of a linear regression was used according to

$$E_a = -R\,\frac{d\,ln\,k\,(t)}{d\;1/T} \tag{4.6}$$

to calculate the activation energies (**Table 4.2**). For the TMD opening and closure, we obtained activation energies of 75.4 ± 26.9 kJ/mol and 38.9 ± 27.2 kJ/mol, respectively. The c-NBS gave values of 55.9 ± 2.8 kJ/mol and 23.7 ± 16.4 kJ/mol for the closure and opening. The Arrhenius plots of TMDs and c-NBS show similar trends and the obtained activation energies are comparable within the margin of error. In both cases, we obtained a higher activation energy for the forward transition than for the reverse transition. This results in an endothermic reaction profile, that would shift the transporter towards the OF conformation under the high physiological temperatures of TmrAB.

Table 4.2. Activation energy of the conformational transition in TmrAB. Activation energy for the forward ($E_{a,fw}$) and reverse ($E_{a,rev}$) transition of TmrAB at the TMDs and c-NBS, and at the TMDs in the catalytically impaired E-to-Q variant. Values given with 95% CI.

	$E_{a,fw}$ (kJ/mol)	$E_{a,rev}$ (kJ/mol)
TMDs	75.43 ± 26.85	38.88 ± 27.21
c-NBS	55.91 ± 2.82	23.71 ± 16.41
TMDs, E-to-Q	126.56 ± 17.10	96.56 ± 9.53

4.2.6 E-to-Q substitution stabilizes the OF conformation

We repeated the experiments after substituting the conserved Walker-B catalytic glutamate to glutamine (E523Q^{A}, E-to-Q) at the c-NBS, yielding TmrA^{EQ}B. As explained in chapter 1.2.2, this substitution significantly reduces the ATPase activity and thereby stabilizes the NBSs in its closed state. Again, samples were incubated with ATP-EDTA. Time-resolved PELDOR analysis of TMD opening in the E-to-Q background revealed a markedly different response in comparison to the catalytically functional transporter. The rate and extent of the IF-to-OF transition was significantly increased (**Figure 4.9a-c**). The time-resolved data points were fitted with eq 4.4 to obtain the rate constants (**Table 4.1**). At 30 °C, the rate constants are comparable between catalytically active and inactive variant. With rising temperature, however, the rate constants for both forward and reverse transition increase significantly. We compared the rate constants of the TmrA^{EQ}B variant in an Arrhenius plot with the functional protein (red circles in **Figure 4.8a**). Notably, the linear fit of the TmrA^{EQ}B data have a much steeper slope, resulting in a 50 kJ/mol higher activation energy for the forward transition and a 60 kJ/mol higher activation energy for the reverse transition. This relative increase of $E_{a,rev}$ causes the faster transition to the OF conformation and stabilizes the OF conformation by further decreasing the reverse transition. Thus, in addition to its essential role for ATP hydrolysis, the catalytic glutamate plays a key role in regulating the kinetics of the IF-to-OF transition.

4.2.7 Turnover conditions enhance the OF conformation

Based on the observed effect of the loss of ATPase function at the c-NBS, we wanted to further investigate the influence of ATP hydrolysis on the transition kinetics. We thus prepared samples of TmrAB with the described spin label pairs to probe the TMDs and NBDs, but this time under hydrolyzing conditions (50 mM ATP + 50 mM

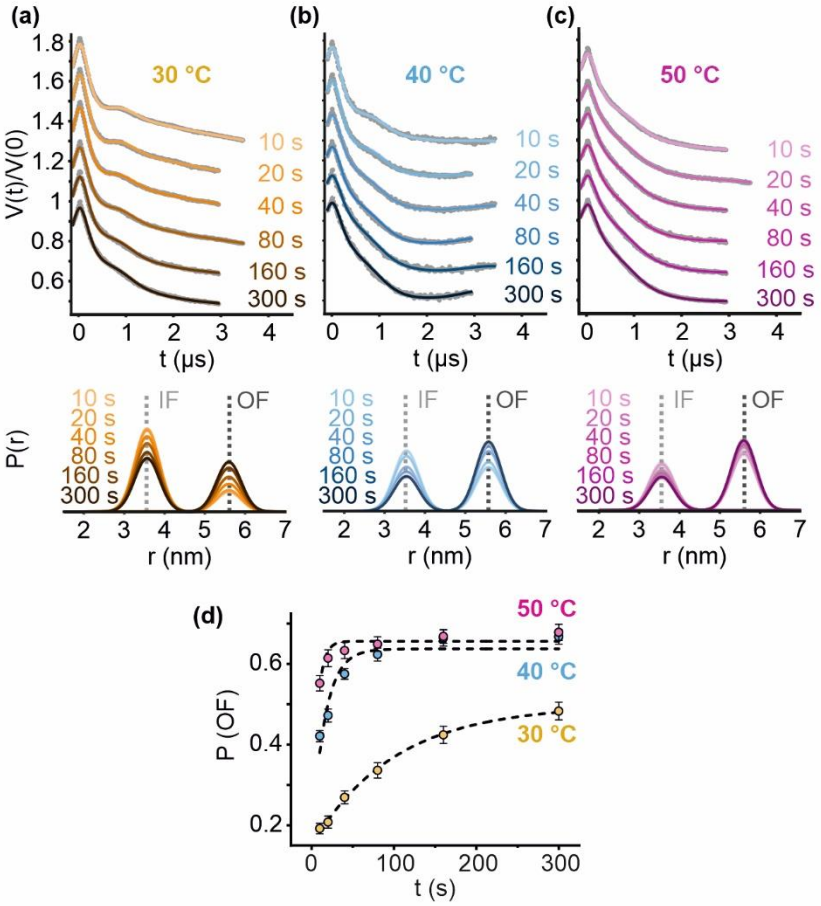

Figure 4.9. TR-PELDOR at the TMD variant V288R1^{A}–E272R1^{B} of TmrA^{EQ}B. TmrAB with a catalytically impaired c-NBS because of the E-to-Q substitution was incubated with ATP-EDTA at (a) 30 °C, (b) 40 °C and (c) 50 °C for increasing time steps between 10 s and 300 s and immediately frozen in liquid nitrogen. Primary PELDOR data V(t)/V(0) overlaid with the fit are shown. Data were globally analyzed using DeerLab. An experimentally determined two Gaussian model corresponding to the IF and OF conformation was used for the analysis. The obtained distance distributions P(r) with a 95% confidence interval are shown. (d) The populations of the OF conformation at each temperature and time point are plotted as a function of time and fitted based on a first order reversible transition as explained in chapter 4.2.5 (dashed lines).

$MgCl_2$) at 40 °C. The obtained values can be found in the appendix (**Supplementary Table 4**). For the TMDs, this resulted in a rapid increase in the OF conformation (**Figure 4.10a**). The populations shifted to the OF conformation within 10 s, revealing a significantly accelerated kinetics occurring in the upper millisecond timescale in comparison to the transition under non-hydrolyzing conditions (**Figure 4.10e**). The population further increased and reached the maximum value around 160 s. In the cellular environment, most of the ATP and Mg^{2+} is assumed to form Mg^{2+}-ATP complexes. To test whether the presence of Mg^{2+} per se affects the IF-to-OF transition, we used the non-hydrolysable ATP analogue ATPγS in combination with Mg^{2+}. This molecule has been used in several structural and biochemical studies to stabilize ABC transporters in the pre-hydrolytic state. Interestingly, in presence of ATPγS-Mg^{2+}, TmrAB showed an IF-to-OF transition identical to that observed with ATP-EDTA (compare **Figure 4.4b** with **Figure 4.10b**).

Both NBSs showed a similar response under turnover conditions, with an identical fraction of the population shifting into the closed conformation withing the first 10 s (**Figure 4.10c,d,f**). Interestingly, while the TMD opening increased over time, for both the NBSs, the closed population slightly decreased over 300 s.

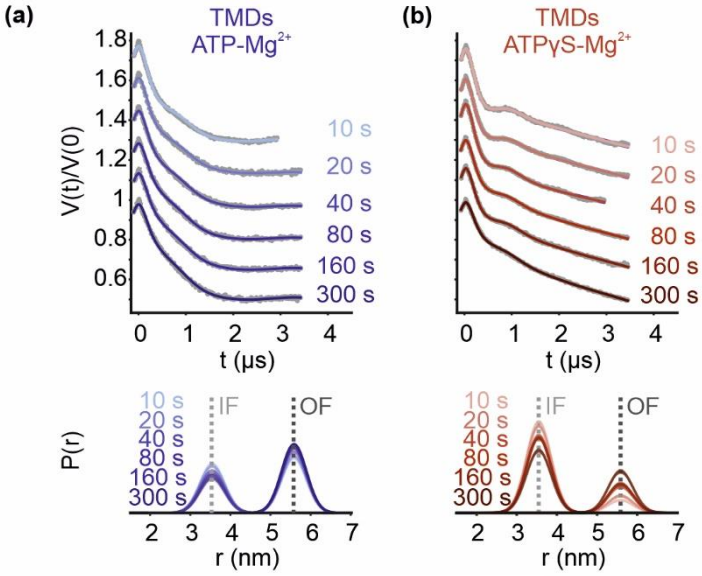

(Figure caption overleaf)

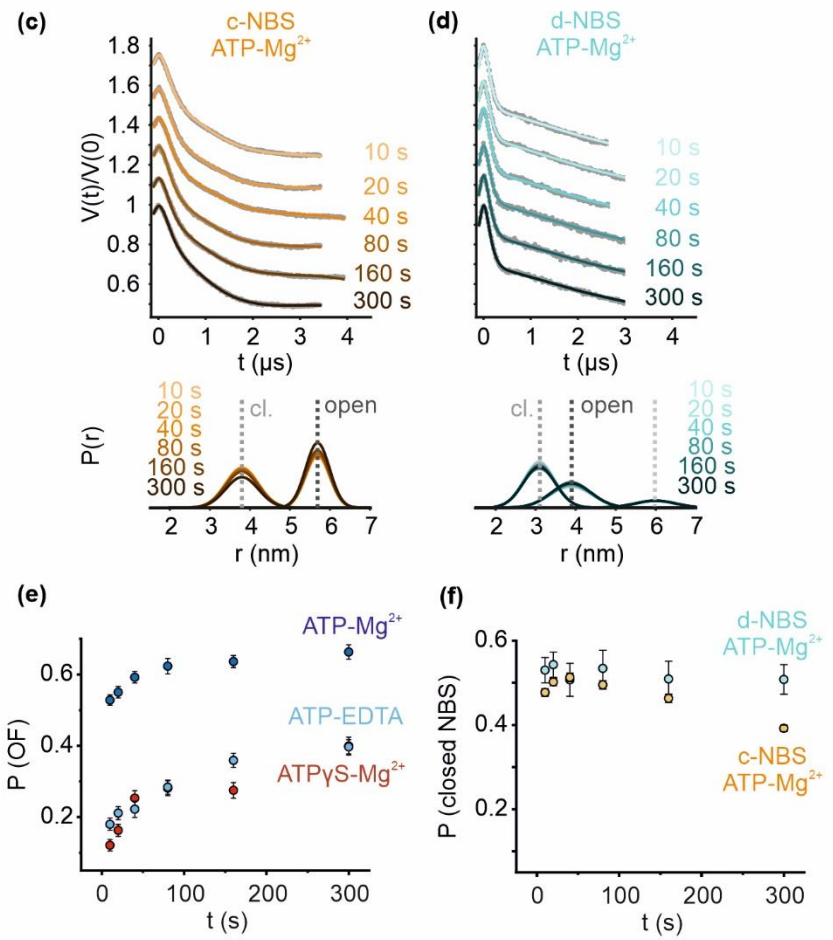

Figure 4.10. TR-PELDOR under hydrolyzing conditions. TmrAB variant V288R1^{A}–E272R1^{B} was incubated with (a) ATP-Mg^{2+} or (b) ATPγS-Mg^{2}, and (c) A416R1^{A}–L458R1^{B} or (d) V461R1^{A}–D349R1^{B} were incubated with ATP-Mg^{2+} at 40 °C for increasing time steps between 10 s and 300 s and immediately frozen in liquid nitrogen. Primary PELDOR data V(t)/V(0) overlaid with the fit are shown. Data were globally analyzed using DeerLab. An experimentally determined two or three Gaussian fit described earlier was used for the analysis. The obtained distance distributions P(r) with a 95% confidence interval are shown. The populations of the OF (e) or closed NBS conformation (f) at each temperature and time point are plotted as a function of time. Error bars are 95% CI.

4.3 Investigation of TmrAB using Mn^{2+}-NO PELDOR spectroscopy

The functional relevance of catalytic asymmetry in ABC transporters is so far not well understood. In order to elucidate the role of both the consensus and the degenerate NBS in regulating the conformational cycle and thus, substrate translocation, a direct investigation of nucleotide interaction at the individual NBSs and the related effects on the TMDs is needed.

Here we examined the asymmetry of nucleotide binding and hydrolysis using PELDOR spectroscopy. However, in contrast to chapter 4.2, we did not solely rely on distance measurements between nitroxide spin labels. We exploited the similar size and charge of the paramagnetic Mn^{2+} ions (see chapter 1.4.7) to replace the Mg^{2+} ions in presence of ATP. Combining Mn^{2+} substitution with an engineered nitroxide label allowed us to simultaneously monitor ATP binding and the conformation at the two NBSs. The following results together with the results in chapter 4.4 have been published.[213]

4.3.1 Design of cysteine variants and manganese substitution

As described in chapter 1.2.2, TmrAB transitions from an inward-facing (IF) to an outward-facing (OF) conformation upon ATP binding or vanadate trapping. This equilibrium transition is temperature-dependent in a broad temperature range (30 – 70 °C) and is driven through an enthalpy-entropy compensation mechanism.[207] First, we designed single-cysteine variants at the NBSs, where the $A416R1^{A}$ and $L458^{B}$ variants probed distances to bound Mn^{2+}-ATP. The $V288R1^{A}$–$V461R1^{A}$–$E272R1^{B}$ variant was used to simultaneously monitor both TMDs and NBSs using NO-NO, Mn^{2+}-NO, and Mn^{2+}- Mn^{2+} PELDOR.

The ATPase activity of the designed and MTSL-labelled variants was confirmed with a colorimetric malachite green phosphate assay at increasing ATP concentrations and was compared to unlabeled wild type TmrAB (**Figure 4.11**). While a decrease of activity is seen with increasing number of labelled positions, all variants actively hydrolyze ATP. Notably, replacing Mg^{2+} with Mn^{2+} had no effect on the activity. Consequently, manganese substitution can be employed to investigate TmrAB under turnover conditions.

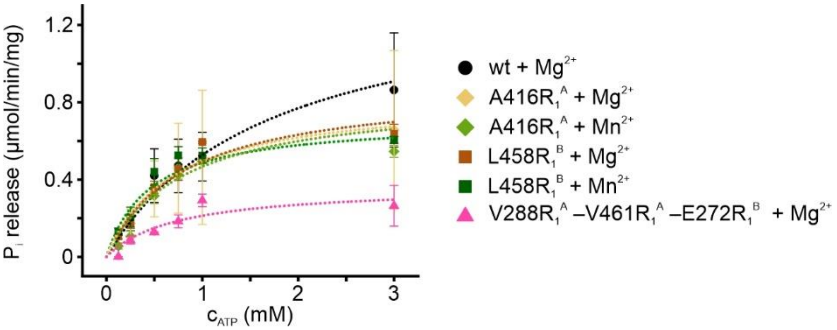

Figure 4.11. ATPase activity assay of spin-labelled variants. Orthophosphate (P_i) forms a green complex with malachite green and molybdate. ATP hydrolysis is measured by monitoring the release of P_i as a function of ATP concentration. All presented ATP hydrolysis data are corrected for background activity in the absence of TmrAB. Data are presented as mean values ± s.d. (n = 3 technical replicates).

4.3.2 Mn^{2+}–ATP is preferentially hydrolyzed at the c-NBS

In vitro experiments involving ABC transporters usually employ mM concentrations of nucleotides and cofactors. In chapter 4.2, 50 mM ATP and Mg^{2+} were added to TmrAB to prepare time-resolved samples under hydrolyzing conditions. However, as explained in chapter 1.4.7, such a large free Mn^{2+} concentration will induce a fast relaxation of the nitroxide labels, and PELDOR distance measurements could become challenging. We overcame this limitation by introducing a buffer exchange step. After incubation of TmrAB with 10 mM of both ATP and Mn^{2+} for 5 min at 50 °C, unbound manganese was removed by fast size exclusion chromatography at 4 °C, while the ATP concentration was kept constant.

First, we investigated the MTSL-labelled single-cysteine variant A416R1^A, where the nitroxide spin label is located at the NBD of TmrA at the c-NBS (yellow rotamers in **Figure 4.12a**). After incubating the transporter with ATP and Mn^{2+} and subsequent removal of free magnesium, we determined distances between A416R1^A and Mn^{2+}-ATP. As TmrAB exists in presence of ATP in an equilibrium between IF and OF conformation, this measurement could yield four distances: distances of the spin label to Mn^{2+}-ATP localized at the c-NBS in its IF (open NBSs) or OF (closed NBSs) conformation, as well as distances of the spin label to Mn^{2+}-ATP localized at the d-NBS in its IF or OF conformation (green and purple dashed lines in **Figure 4.12a**). Our

simulations showed that the interspin distances can clearly be distinguished between Mn^{2+}-ATP bound at the c-NBS and at the d-NBS. However, the simulations showed no significant change in the distances between the open and closed NBS conformations. This means that this labelled variant can yield information about whether manganese is bound to an NBS, but not about the conformation of the NBSs.

We experimentally determined these distances using Mn^{2+}-NO PELDOR spectroscopy. The modulation depths for the Mn^{2+}-NO PELDOR ranged between 5 – 15 % (**Figure 4.12b-e**). The decreased modulation depth observed is mostly due to free manganese, which could not be quantitatively removed during the buffer exchange step and varied between experiments. This contribution is identical for a particular set of samples, which enables a quantitative comparison of the modulation depths between these samples. The smaller modulation depth also suppressed any multi-spin contributions for the respective samples.[214]

The distance distribution P(r) was extracted from the PELDOR time trace by Tikhonov regularization. We observed only a single distance at 4.7 ± 0.4 nm in the distance distribution (black line in **Figure 4.12b**). This distance coincides with the simulated distance of A416R1^{A} to the Mn^{2+} at the d-NBS (purple dashed lines). Distances that could be attributed to Mn^{2+} in the c-NBS are not present. Mn^{2+} at the c-NBS is lost, and we hypothesized that this is due to ATP hydrolysis. While the d-NBS has a greatly reduced ATPase activity, thus retaining ATP and Mn^{2+} in the active site and resulting in the corresponding distance in P(r), the c-NBS readily hydrolyses ATP to ADP, which is quickly exchanged for free ATP and new Mn^{2+}. After the removal of free Mn^{2+} however, no new metal ions are available and the c-NBS remains without Mn^{2+}. To verify this hypothesis, we prepared a sample in the vanadate-trapped state, which stabilizes the NBSs in its closed conformation in an Mn^{2+}-ADP-VO_4^{3-} state (see chapter 4.2.2). Model-free analysis gave a distance at 4.7 ± 0.3 nm, again corresponding to the d-NBS. Notably, however, the primary data revealed a further oscillation, which yielded a second distance at 2.7 ± 0.3 nm **(Figure 4.12c**). This second distance agrees with the simulated distance of A416R1^{A} to Mn^{2+} at the c-NBS (green dashed lines). The trapping of TmrAB now also leads to a stable occlusion of Mn^{2+} at the c-NBS. This confirms that under hydrolyzing conditions in presence of ATP-Mn, the c-NBS rapidly hydrolyses ATP, while the d-NBS preferentially harbors an occluded ATP. In both samples, the experimental data compare well to the simulated distances.

Since position A416R1^{A} cannot distinguish between the open and closed conformations of the NBSs, we designed another spin label, L458C^{B}. Simulations showed that distances from L458R1^{B} can differentiate the two conformations at the

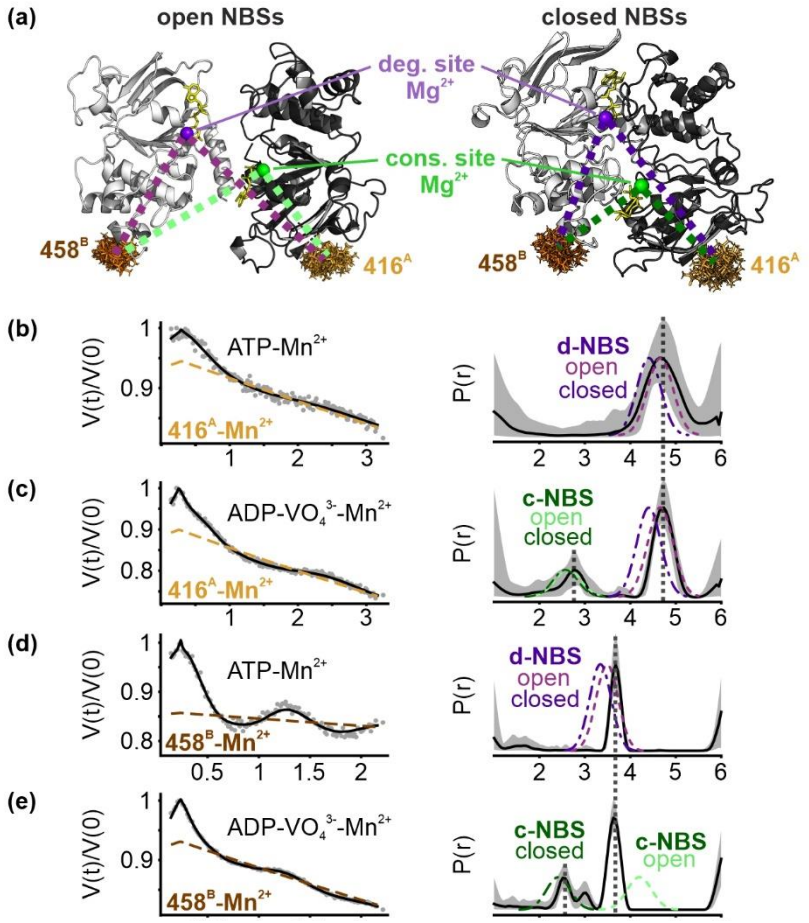

Figure 4.12. Mn^{2+}–NO PELDOR at the two NBSs. (a) MTSL labelled positions with the rotamers and Mg^{2+} ions are highlighted at the NBDs in the open (PDB: 6RAG) or closed (PDB: 6RAJ) conformation. (b,c,d,e) Mn^{2+}–NO PELDOR data (left) and the corresponding distance distributions (right) obtained using the A416R1^{A} or L458R1^{B} variant as indicated (in black). The simulated distances on the IF and OF structures (PDBs 6RAG and 6RAJ respectively) are overlaid with dotted lines.

c-NBS, but not at the d-NBS. As observed with C416R1^{A}, in presence of Mn^{2+}-ATP, L458R1^{B} gave only a single distance at 3.6 ± 0.2 nm corresponding to the d-NBS **Figure 4.12d**). No distances were observed corresponding to the open or closed conformation of the c-NBS. In the vanadate-trapped state, we observed the same peak at 3.6 ± 0.2 nm (d-NBS), as well as a second distance at 2.5 ± 0.2 nm corresponding to the closed conformation of the c-NBS (dark green dashed line in **Figure 4.12e**). Simulations predicted significantly longer distances for the open conformation of the c-NBS (light green dashed line), which we did not detect. Thus, Mn^{2+}-ADP-VO_4^{3-} binds only to the closed conformation of the c-NBS. Since the fast exchange due to hydrolysis at the c-NBS is overcome by vanadate trapping in the post-hydrolysis state, hydrolysis in the closed c-NBS must happen before trapping.

4.3.3 Concomitant observation of TMDs and NBSs

Having established the Mn^{2+}-NO PELDOR approach on the two single-cysteine variants, we wanted to further elucidate the mechanistic details of the coupling between NBSs and TMDs by designing an experiment to detect the conformation of TMDs and NBSs simultaneously in one sample. We engineered a triple MTSL-labelled TmrAB variant by combining the previously used V288C^{A}–E272C^{B} construct with the V461C^{A} substitution at the NBS (magenta and cyan labels in **Figure 4.13**). At position V461C^{A}, simulations showed that it can be clearly distinguished between the open and closed conformations at the d-NBS, but not at the c-NBS. Together with the previously used L458C^{B} variant, the binding and conformational status at both NBSs can be assessed. Samples were prepared as described earlier after incubating with Mn^{2+}-ATP. In this sample, the conformation of TMDs and NBSs was observed using NO-NO and Mn^{2+}-NO PELDOR, respectively. The nitroxide spin labels engineered on the TMDs and NBS are far separated (> 8 – 12 nm) and their interaction was too weak to be detected within the observable time window of the PELDOR experiments (**Supplementary Figure S6**).

First, we investigated the sample incubated with Mn^{2+}–ATP. For the TMDs, NO-NO PELDOR was analyzed with the two-Gaussian model-based approach introduced in chapter 4.2.1, and showed a mixed population of the IF conformation (distance at 3.6 ± 0.3 nm) with a fraction of 0.45, and the OF conformation (distance at 5.6 ± 0.3 nm) with a fraction of 0.55 **Figure 4.14a**), comparable to the distance distributions obtained under hydrolyzing (Mg^{2+}–ATP) conditions in chapter 4.2.7. By measuring the same sample with Mn^{2+}-NO PELDOR, we observed only a single distance at 3.2 ± 0.2 nm, corresponding to the closed conformation at the d-NBS (**Figure 4.14c**). Again, no

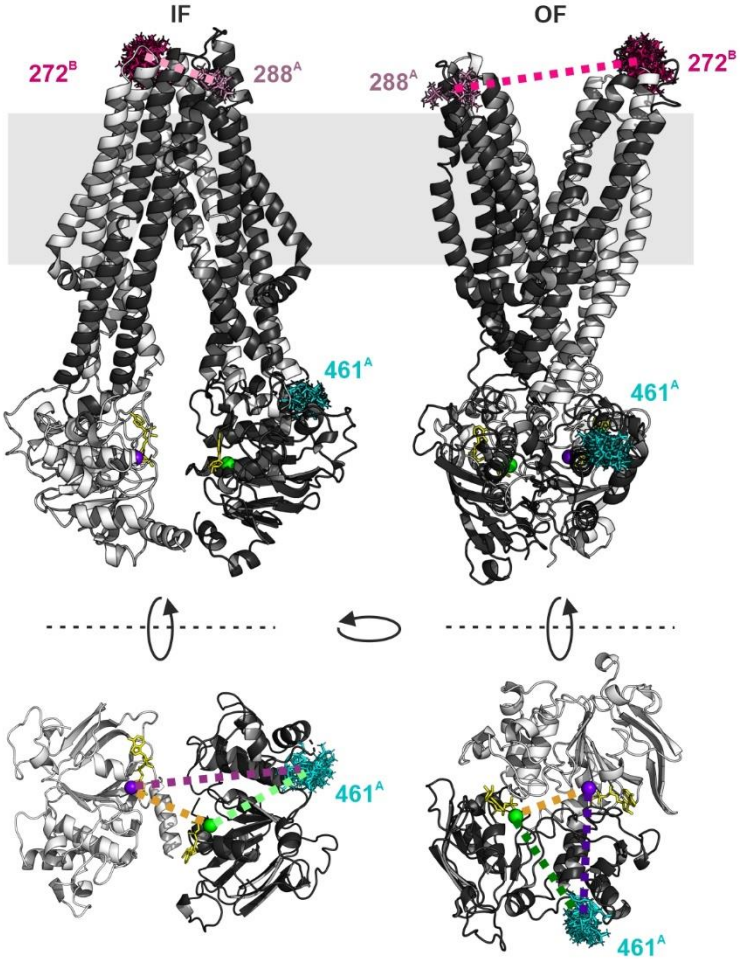

Figure 4.13. MTSL triple-labelled variant of TmrAB. MTSL labeled positions are indicated at the NBDs and TMDs in the IF (PDB: 6RAG) or OF (PDB: 6RAJ) conformation in the full-length transporter (top) and in the isolated NBDs in a view from the membrane towards the cytoplasm (bottom). The Mg^{2+} ion at the c-NBS (green) and at the d-NBS (purple) as well as ATP (yellow) are highlighted. TmrA (black), TmrB (grey). For better visibility, the OF conformation is rotated by 90° clockwise along a vertical axis.

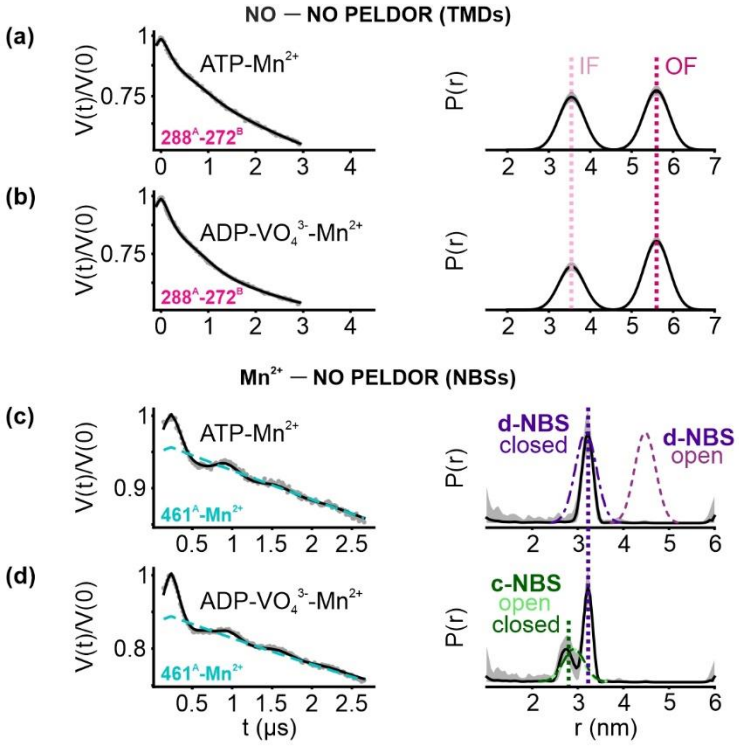

Figure 4.14. Concomitant Mn^{2+}-NO and NO-NO PELDOR of TmrAB WT*. (a,b) NO-NO (for V288R1^{A}–E272R1^{B}), (c,d) Mn^{2+}-NO (for V461R1^{A}) PELDOR data (left) and the corresponding distance distributions (right) for the Cys-less (WT*) variant. For V288R1^{A}–E272R1^{B}, an experimentally determined two Gaussian model was used for the analysis as described in chapter 4.2. A 95% confidence interval is shown, which is invisible if thinner than the linewidth. Simulated distances for the IF and OF conformations (PDBs 6RAG and 6RAJ respectively) are overlaid with dotted lines.

distances corresponding to any conformation of the c-NBS were observed. The absence of distances corresponding to the open d-NBS conformation reveals a reduced affinity for ATP in the open conformation (as with c-NBS, see **Figure 4.12e**).

Next, we repeated the experiment in the vanadate-trapped (5 min at 50 °C) state. For the TMDs, NO-NO PELDOR analysis revealed an increase of the fraction of the OF conformation to approximately 0.65 (**Figure 4.14b**). For the NBSs, Mn^{2+}-NO PELDOR revealed the presence of an additional distance at 2.8 ± 0.2 nm, which corresponds to the c-NBS (**Figure 4.14d**). Based on the results from the L458C^{B} variant (see **Figure 4.12e**), this distance can be attributed to the closed state of the c-NBS, so that under our experimental conditions, binding of Mn^{2+}–ATP can only be observed to the closed conformation of either NBS.

4.3.4 E-to-Q mutation leads to occlusion of ATP at c-NBS

So far, incubating with Mn^{2+}-ATP lead to the occlusion of Mn^{2+}-ATP only at the d-NBS, and vanadate trapping TmrAB in the post-hydrolytic state resulted in a small population corresponding to the closed c-NBS. To validate our hypothesis that the fast ATP hydrolysis at the c-NBS leads to the loss of Mn^{2+}-ATP from the c-NBS, and further investigate the role of the catalytic asymmetry, we repeated the NO-NO and Mn^{2+}-NO PELDOR experiments after substituting the conserved Walker-B catalytic glutamate to glutamine (E-to-Q) at the c-NBS. This catalytically impaired variant with a significantly reduced ATPase activity was also employed in chapter 4.2.5 for the kinetic investigation of TmrAB and was here combined with the triple MTSL-labelled TmrAB variant V288C^{A}–E272C^{B}–V461C^{A}.

TmrA^{EQ}B was incubated with Mn^{2+}-ATP. For the TMDs, NO-NO PELDOR analysis revealed an increase of the fraction of the OF conformation to approximately 0.70 (**Figure 4.15a**, compare to **Figure 4.14a**).

Remarkably, we observed a broad peak in the Mn^{2+}-NO PELDOR that clearly corresponds to the overlaid distances for the closed d-NBS at 3.2 ± 0.2 nm and the closed c-NBS at 2.8 ± 0.2 nm (**Figure 4.15b**). Under the same conditions in the catalytically functional TmrAB variant, no binding of Mn^{2+}-ATP to the c-NBS was detected. In contrast to the vanadate-trapped conditions, Mn^{2+}-ATP binding was substantially increased in the E-to-Q variant. The amplitude of the probability distribution of Mn^{2+}-ATP at the c-NBS became almost equal to the contribution from the d-NBS.

Apart from the distances corresponding to the c-NBS and d-NBS, the Mn^{2+}-NO PELDOR showed an additional minor peak at approximately 2.0 ± 0.2 nm that, based on simulations, could correspond to a Mn^{2+}-Mn^{2+} distance. To further characterize this distance, we measured Mn^{2+}-Mn^{2+} PELDOR on the same sample. Analysis by Tikhonov regularization revealed the same distance of 2.0 ± 0.2 nm. This confirmed that two Mn^{2+} atoms are occluded at the NBSs of TmrA^{EQ}B (**Figure 4.15c**).

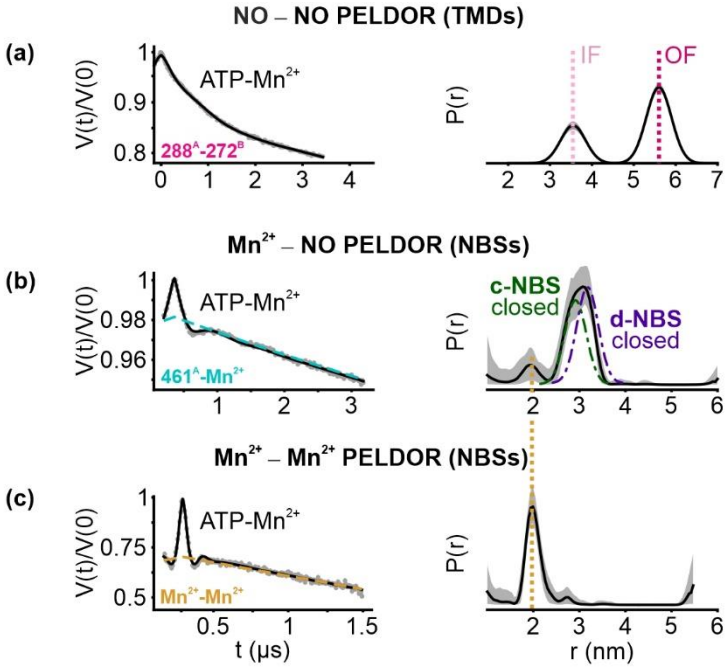

Figure 4.15. Concomitant Mn^{2+}-NO, NO-NO and Mn^{2+}-Mn^{2+} PELDOR of $TmrA^{EQ}B$. (a) NO-NO (for $V288R1^{A}$–$E272R1^{B}$), (b) Mn^{2+}-NO (for $V461R1^{A}$) and (c) Mn^{2+}-Mn^{2+} PELDOR data (left) and the corresponding distance distributions (right) for the E-to-Q variant. For $V288R1^{A}$–$E272R1^{B}$, an experimentally determined two Gaussian model was used for the analysis as described in chapter 4.2. A 95% confidence interval is shown, which is invisible if thinner than the linewidth. Simulated distances for the IF and OF conformations (PDBs 6RAG and 6RAJ respectively) are overlaid with dotted lines.

4.4 Time-resolved Mn^{2+}-NO PELDOR spectroscopy of TmrAB

Since we could establish in chapter 4.2 time-resolved PELDOR spectroscopy of TmrAB as a useful technique to study the kinetics of the conformational transitions, and in chapter 4.3 the combination of NO-NO and Mn^{2+}-NO PELDOR measurements to simultaneously observe the TMDs and the NBSs and to investigate the catalytic asymmetry of a heterodimeric ABC exporter, we have created a promising toolbox. By combining both techniques, we are now able to observe and compare the dynamic behavior on two important protein domains at the same time.

4.4.1 Employed TmrAB cysteine variants

For the time-resolved concomitant measurement of NO-NO and Mn^{2+}-NO PELDOR, we again utilized the triple cysteine variant $V288C^{A}$–$E272C^{B}$–$V461C^{A}$. To probe the conformation of TmrAB using NO-NO PELDOR, we used the double cysteine variants described in chapter 4.2.1: the $V288C^{A}$–$E272C^{B}$ variant for the TMDs, the $A416C^{A}$–$L458C^{B}$ variant for the c-NBS, and the $V461C^{A}$–$D349C^{B}$ variant for the d-NBS.

4.4.2 Reverse transition and loss of Mn^{2+}– ATP from the d-NBS

The Mn^{2+}-NO experiment involves a buffer exchange step to remove free Mn^{2+} from the sample. We exploited this obligatory step to remove ATP at the same time and included a subsequent additional incubation step. With the removal of ATP, TmrAB can now undergo a single reverse transition from the OF state back to the IF state. By varying the second incubation time, we tried to time-resolve this reverse transition to compare our observations at the TMDs and NBSs. After incubating the triple-labelled variant with ATP and Mn^{2+} for 5 min at 50 °C, the buffer containing ATP and Mn^{2+} was exchanged for a buffer containing EDTA to chelate trace amounts of metal ions. Immediately after removal, a sample was prepared for PELDOR measurement. The NO-NO PELDOR data revealed a mixed population of IF and OF conformations at the TMDs (**Figure 4.16a**, 0 s sample), as was expected based on our observations in chapter 4.3.3. The remaining sample after buffer exchange was incubated for 80 s or 300 s at 50 °C, before samples were prepared for measurement. We observed a decrease of the population of the OF state over time, and after 5 min, TmrAB returned almost completely to the IF conformation (**Figure 4.16a**). This confirms that after an induced forward transition, TmrAB can return to the IF state in the absence of ATP.

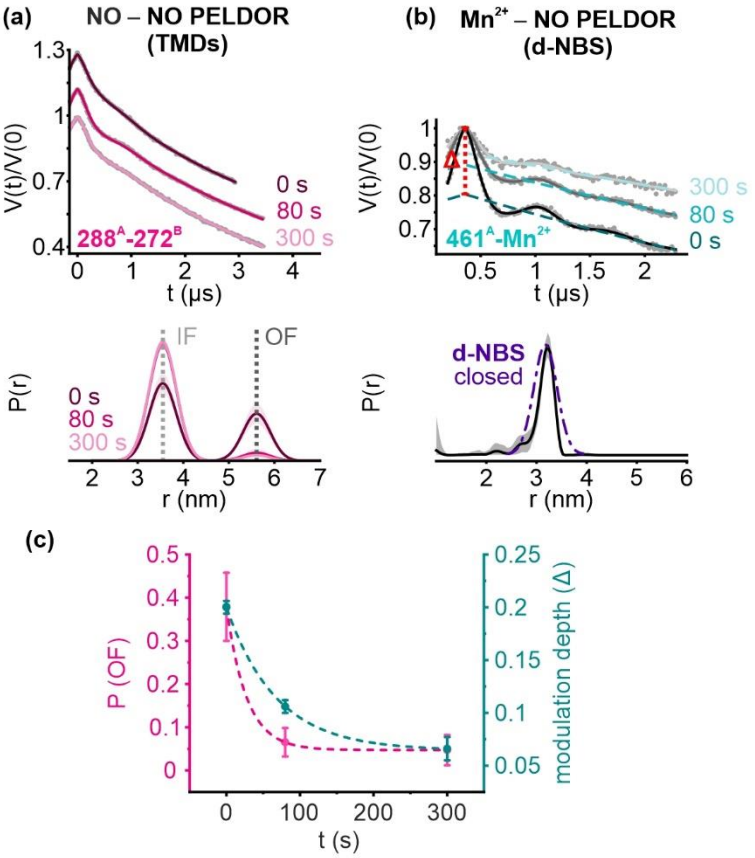

Figure 4.16. Concomitant time-resolved reverse-transition Mn^{2+}-NO and NO-NO PELDOR. Time-resolved *(a)* NO-NO (for V288R1^{A}–E272R1^{B}) or (b) Mn^{2+}–NO (using V461R1^{A}) 4-pulse PELDOR and the corresponding distance distributions. (c) The variation of the modulation depth Δ (cyan) and the probability amplitude (magenta) of the distance distributions (for the OF conformation) are plotted against time. Data were globally analyzed using the DeerLab platform. For V288R1^{A}–E272R1^{B}, an experimentally determined two Gaussian model was used for the analysis as described before. A 95% confidence interval is shown, which is invisible if thinner than the linewidth. Error bars are 95% CI.

The same time-resolved samples were measured by Mn^{2+}-NO PELDOR. As in chapter 4.3.3, we observed a single distance corresponding to the closed state of the d-NBS (**Figure 4.16b**). Since these time-resolved samples were prepared from the same initial sample, they had identical concentrations of protein and Mn^{2+}, and the modulation depth Δ (indicated as dashed red line in **Figure 4.16b**) of the primary PELDOR data contains quantitative information about the amount of Mn^{2+} localized at the d-NBS. ATP hydrolysis or d-NBS opening would lead to a dissociation – and thus loss – of Mn^{2+} from the d-NBS, resulting in a decrease of the modulation depth. Indeed, we observed a decrease of modulation depth with increasing incubation time. Notably, this decrease of the modulation depth correlated with the decrease of the population of the OF conformation at the TMDs (**Figure 4.16c**).

4.4.3 Regulation of the reverse transition

To further investigate the regulation of the reverse transition, we repeated the time-resolved reverse transition experiment in a pure NO-NO PELDOR setup. This gave us more freedom in observing the reverse transition under different conditions by adding cofactors to the sample when ATP is removed.

First, the TMDs were studied, and TmrAB was incubated with 50 mM ATP and 0.5 mM EDTA for 5 min at 50 °C to induce a forward transition under non-hydrolyzing conditions. This was described in detail in chapter 4.2.2, and the fraction of the OF conformation is plotted as a function of the incubation time in **Figure 4.17e**. After 5 min, ATP was removed while the EDTA concentration was kept constant. Analogous to chapter 4.4.3, the samples were then incubated for a second time at 50 °C, for 80, 160, or 300 s, to time-resolve the reverse transition. Without added cofactors and in the presence of 0.5 mM EDTA to chelate trace amounts of metal ions, the time-resolved distance distributions revealed a mixed population between the IF and OF states with a slow and incomplete reverse transition towards the IF state (**Figure 4.17a,e**). If, however, 50 mM Mg^{2+} were added to the sample at the time of the ATP removal, the reverse transition was significantly accelerated (**Figure 4.17b,e**). After 5 min, TmrAB has almost completely switched back to the IF conformation. We also investigated the influence of the presence of 10 mM ADP on the reverse transition. Interestingly, the return to the IF state was significantly accelerated, but not to the extent seen in the presence of Mg^{2+}, and after 5 min of incubation, approximately 20 % of transporters remained in the OF conformation (**Figure 4.17c,e**). Lastly, we also added 50 µM of a

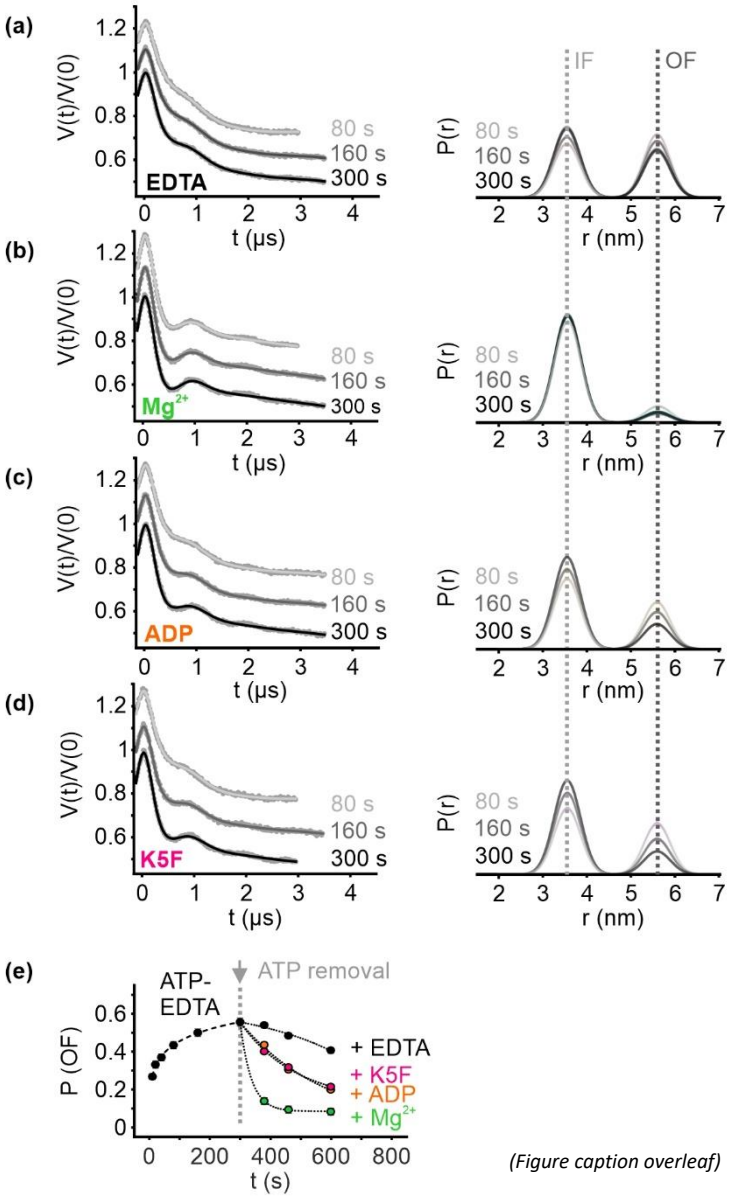

(Figure caption overleaf)

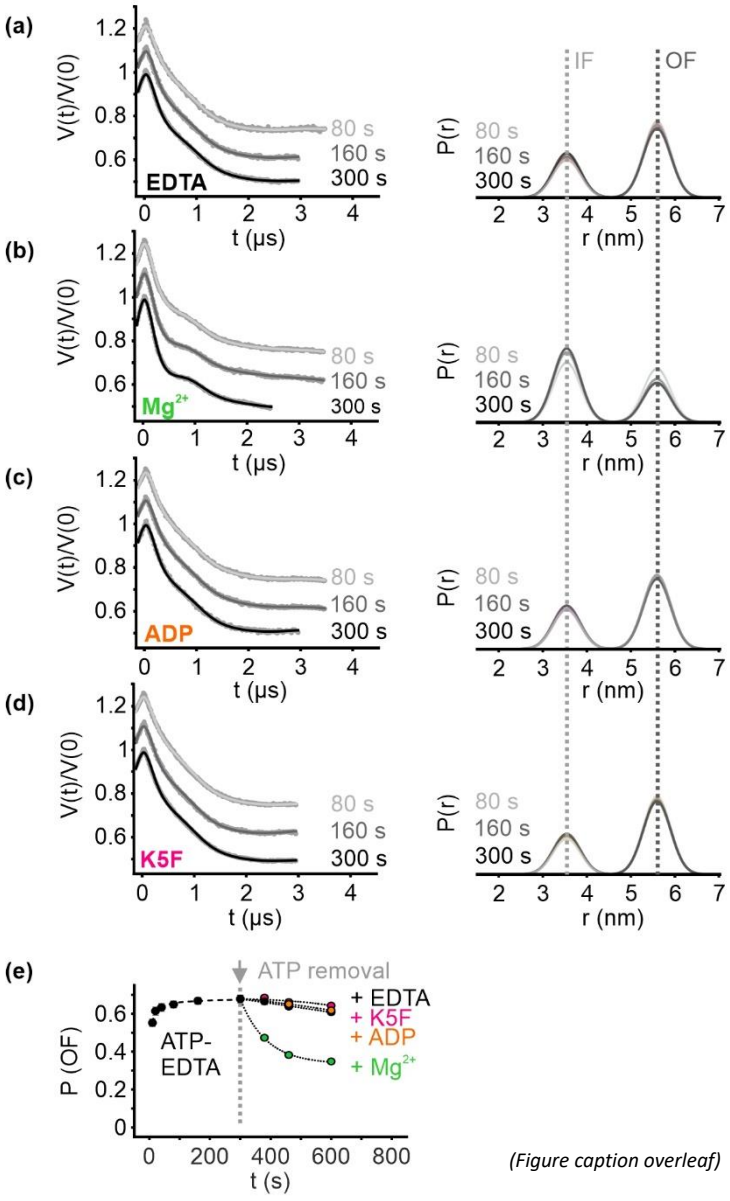

(Figure caption overleaf)

[p. 97] Figure 4.17. Time-resolved reverse-transition NO-NO PELDOR at the TMDs in WT*. To observe the reverse transition (OF-to-IF), TmrAB was incubated with ATP-EDTA at 50 °C for 300 s. Subsequently, ATP was removed in the presence of EDTA (a), $MgCl_2$ (b), ADP (c) or peptide substrate K5F (d) by a desalting step at 4 °C, incubated at 50 °C for increasing time steps between 80 s and 300 s and immediately frozen. (a,b,c,d) Left, NO-NO PELDOR data V(t)/V(0) for $V288R1^{A}$–$E272R1^{B}$ in the Cys-less (WT*) background overlaid with the fit. Data were globally analyzed using the DeerLab program. An experimentally determined two Gaussian model was used for the analysis as described before. Right, the obtained distance distributions P(r) with a 95 % confidence interval. (e) The probabilities for the OF conformation are plotted as a function of the incubation time. The results for the forward transition (ATP-EDTA, 50 °C) from chapter 4.2.3 are included. Error bars are 95% CI.

[p. 98] Figure 4.18. Time-resolved reverse-transition NO-NO PELDOR at the TMDs in $TmrA^{EQ}B$. To observe the reverse transition (OF-to-IF), TmrAB was incubated with ATP-EDTA at 50 °C for 300 s. Subsequently, ATP was removed in the presence of EDTA (a), $MgCl_2$ (b), ADP (c) or peptide substrate K5F (d) by a desalting step at 4 °C, incubated at 50 °C for increasing time steps between 80 s and 300 s and immediately frozen. (a,b,c,d) Left, NO-NO PELDOR data V(t)/V(0) for $V288R1^{A}$–$E272R1^{B}$ in the catalytically impaired E-to-Q background overlaid with the fit. Data were globally analyzed using the DeerLab program. An experimentally determined two Gaussian model was used for the analysis as described before. Right, the obtained distance distributions P(r) with a 95 % confidence interval. (e) The probabilities for the OF conformation are plotted as a function of the incubation time. The results for the forward transition (ATP-EDTA, 50 °C) from chapter 4.2.6 are included. Error bars are 95% CI.

known substrate, the peptide K5F, during the reverse transition. Notably, this accelerated the reverse transition to the same extent as the presence of ADP.

To better understand these observations, we repeated the experiment in the catalytically impaired E-to-Q mutant while again observing the TMDs. As was established in chapter 4.2.5, the E-to-Q mutation significantly alters the energy landscape for the transitions in TmrAB. This results in an accelerated forward transition (see also **Figure 4.18e**). By time-resolving the second incubation after ATP removal in the same manner as in the catalytically functional variant and without the additions of cofactors, the reverse transition was significantly decelerated, and $TmrA^{EQ}B$ remained mostly in the OF conformation (**Figure 4.18a,e**). When Mg^{2+} was present during the second incubation, the reverse transition was significantly increased, but not to the extent as in the catalytically functional variant, and $TmrA^{EQ}B$ remained after 5 min to approximately 40 % in the OF conformation (**Figure 4.18b,e**). The influence of ADP and the peptide substrate K5F was probed. Remarkably, neither

showed an effect on the speed of the reverse transition and remained at the same mix of populations as without the addition of cofactors or substrate (**Figure 4.18c,d,e**). This observation contrasts with the results from the catalytically functional variant (compare **Figures 4.17e and 4.18e**).

4.4.4 Reverse transition involves opening of both NBSs

Based on our findings on the asymmetric behavior of both NBSs in the last chapters, we wanted to compare the results from the TMDs to the reverse transition and their regulation of the c-NBS and d-NBS. The experiment from chapter 4.4.3 was thus repeated with the respective TmrAB variants with the spin label pairs at the c-NBS and d-NBS. Since the nitroxide spin labels are attached at different residue positions in TmrAB, the variants could display a altered energy landscape of conformational transitions. Therefore, we limited the analysis of the reverse transition to a qualitative comparison by normalizing to the maximum population of the OF state P(OF) for the TMDs and the maximum fraction of closed c-NBS P(cl. C-NBS) (**Figure 4.19e**) and d-NBS P(cl. D-NBS) (**Figure 4.19f**).

At the c-NBS, the forward transition was followed in a time-resolved manner at 50 °C after the addition of ATP-EDTA, as was shown in chapter 4.2.3. The normalized forward transition of the c-NBS to its closed conformation coincided with the shift of the TMDs to the OF conformation. ATP removal in the presence of EDTA then lead to a slow and incomplete return of the c-NBS to its open state. This return was similar in extent, but slightly faster than the return of the TMDs to the IF conformation (**Figure 4.19a,e**). After 5 min, approximately 40 % of transporters remained in the closed conformation. When Mg^{2+} was added during the removal of ATP (see chapter 4.4.3), the reverse transition of the c-NBS was accelerated and the c-NBS returned almost completely to its open conformation after 5 min, which correlated to the return of the TMDs (**Figure 4.19b,e**). After 5 min, approximately 20 % of transporters remained in the closed conformation. The forward transition of the d-NBS coincided with the forward transition of the TMDs, as well. The following ATP removal in presence of EDTA resulted in a reverse transition that was faster than the return of the TMDs to the IF state, and after 5 min, approximately 20 % of transporters still had a closed d-NBS. The addition of Mg^{2+} for the reverse transition once again resulted in a fast and full return of the d-NBS to its open conformation.

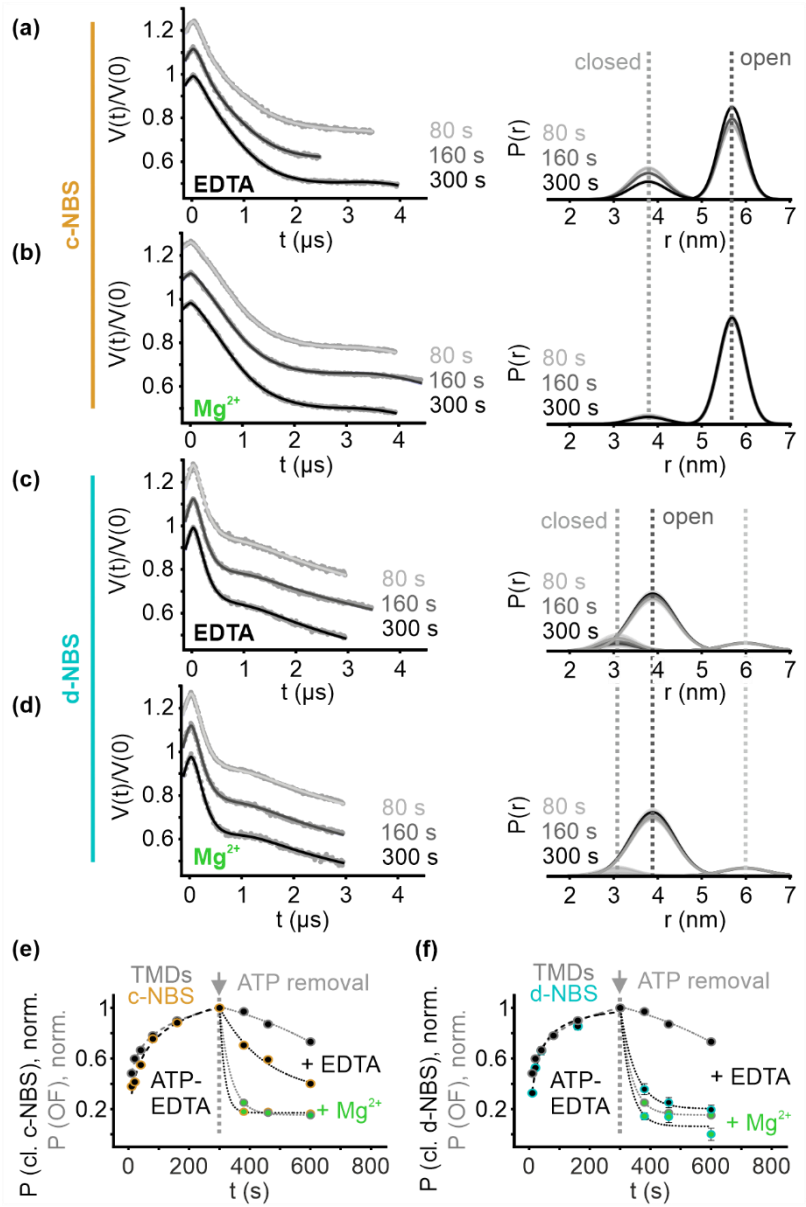

(Figure caption overleaf)

[p. 101] Figure 4.19. Time-resolved reverse-transition NO-NO PELDOR at both NBSs in WT*. To observe the reverse transition (closed-to-open NBS), TmrAB was incubated with ATP-EDTA at 50 °C for 300 s. Subsequently, ATP was removed in the presence of EDTA (a,c) or $MgCl_2$ (b,d) by a desalting step at 4 °C, incubated at 50 °C for increasing time steps between 80 s and 300 s and immediately frozen. Left, NO-NO PELDOR data V(t)/V(0) at the c-NBS for A416**R1**^{A}–L458R1^{B} (a,b) or at the d-NBS for V461R1^{A}–D349R1^{B} (c,d) in the Cys-less (WT*) background overlaid with the fit. Data were globally analyzed using the DeerLab program. An experimentally determined Gaussian model was used for the analysis as described before. Right, the obtained distance distributions P(r) with a 95 % confidence interval. The normalized probabilities for the closed c-NBS (e) and d-NBS (f) conformation are plotted as a function of the incubation time. The results for the forward transition (ATP-EDTA, 50 °C) from chapter 4.2.7 are included. The normalized probabilities for the OF conformation of the TMDs from **Figure 4.17** are overlaid. Error bars are 95% CI.

5 DISCUSSION

5.1 Kinetic analysis of TmrAB using time-resolved PELDOR spectroscopy

So far, the characterization of kinetic parameters for the conformational transitions of large biomolecules such as ABC transporters is largely missing. By preparing identical samples of TmrAB in presence of ATP with different incubation times, the evolution of the conformational equilibrium could be resolved as a function of time and temperature using PELDOR spectroscopy. This enabled me to observe the conformational distribution of key regions in TmrAB.

Analysis of the primary data of the TMD variant by fitting with a non-parametric distribution showed that both the IF and the OF conformation are characterized mainly by one interspin distance, respectively, which compared well to simulations (**Figure 4.3**). For the c-NBS and d-NBS, the same results were previously obtained. Since results in an earlier study also showed that samples incubated for 5 min at different temperatures could be fitted with a parametrized model based only on these distance restraints[207], the same approach was chosen here. The time-resolved samples of all three spin label pairs exhibit good fits of the respective Gaussian models to the primary data for all temperature and time points. No further distance restraint was necessary, indicating that no additional distance between the spin labels is present in the sample. This could suggest that indeed only the IF and OF state exist over the time-resolved data series. However, another conformation of TmrAB was characterized by cryo-EM in $TmrA^{EQ}B$ under turnover conditions. In this outward-facing occluded conformation ($OF^{occluded}$, see chapter 1.2.6), the NBDs are dimerized, and the periplasmic gate is closed, resulting in distances indistinguishable from the closed conformation of both NBSs and the OF conformation of the TMDs. Based on our spectroscopic data alone, the presence of this occluded state cannot be ruled out with certainty. Due to the inability to distinguish the $OF^{occluded}$ state with the here used spin-labelled variants, it was neglected from our considerations regarding the observed conformations, but our interpretations must therefore be taken with a grain of salt until further clarification. For the heterodimeric ABC exporter TM287/288, unbiased MD simulations showed that initial NBS closure leads to the formation of an occluded conformation, with subsequent opening of the TMDs[215]. It is therefore well possible that TmrAB transiently via $OF^{occluded}$ conformation as intermediate state during the forward transition, but this might happen on time scales faster than the

resolution of this experimental setup. This question was further investigated by the here conducted quantitative analysis of the conformational transitions and will be discussed later in this chapter.

The time-dependent change of the conformational distribution of proteins can be a fast process in the milliseconds or even microseconds timescale[216–218]. For these fast transitions, a manual preparation of time-resolved samples is not sufficient. Recently, the use of an RFQ-EPR setup was demonstrated to obtain temporal resolution on the milliseconds timescale.[165] However, this approach requires large amounts of sample, which is challenging for membrane proteins with low expression yields. For TmrAB, it was recently shown that decreasing the temperature to 45 °C slows down the transport activity to the timescale of minutes.[210] In a publication that employed PELDOR spectroscopy for the temperature-dependent investigation of TmrAB, the transporter reached its equilibrium at reduced temperatures of 40 and 50 °C within 5 min upon incubation with ATP. We therefore chose the same temperature conditions. Our TR-PELDOR results under non-hydrolyzing conditions (ATP-EDTA, **Figures 4.4-4.6**) show that we could slow down the kinetics of conformational transition enough to achieve temporal resolution without a RFQ setup. Even so, time-resolved sample preparation with snapshots of the conformational evolution requires substantial amount of sample. Moreover, the measurement time was significant. For these reasons, no sound statistical analysis could be performed for the values obtained from spectroscopic experiments that would have required at least biological triplicates for the most meaningful results. For the TMD variant, incubated with ATP-EDTA at 40 °C, biological triplicates were measured, and a standard error of the mean between 0.005 and 0.027 was calculated. This shows that both the deviations between different batches of protein expression and purification, and technical deviations from mixing errors and manual operation of sample incubation and freezing were low enough to investigate the conformational transitions. For the other labelling positions and conditions, biological replicates were partly generated and measured, and usually showed a comparable deviation of 0.01 - 0.03 (see Appendix, **Supplementary Tables S2-S4**).

Qualitatively, both the variants probing the NBSs and the one probing the TMDs showed the same behavior. The conformational distribution slowly shifted over the course of the observed incubation time towards the open periplasmic gate and the closed NBS conformations. Both maximum extent and initial speed of this shift increased with increasing temperature. The same time scale was observed for the prototypical NBD MJ0796, where 3 min were required for its dimerization.[161] While the extent of TMD opening and c-NBS closure was comparable in our experiments, the extent of d-NBS closure was smaller. This difference could arise due to different

energy landscapes based on the incorporation of the spin labels at different positions, or it could reveal an asymmetric behavior of TmrAB during the IF-to-OF transition. Altogether, these observations agree with the view that ATP induces the closure of both NBSs, which further drives TMD opening.

In order to compare the kinetics of TMD opening and NBS closure beyond a qualitative level, the rate constants for the respective conformational transitions need to be determined. To obtain the rate constants, a kinetic model was chosen than can best and in the simplest way describe the experimental observations. This model was established in our previous publication for TmrAB.[207] The same model was suggested to interpret the cryo-EM results obtained for the peptidase-containing ABC transporter PCAT1 under non-hydrolyzing conditions.[219] Furthermore, a similar model was proposed as part of the transport cycle for the heterodimeric ABC transporter MRP1, but with the forward rate constant k_1 describing the binding of ATP and NBD dimerization, and the reverse rate constant k_{-1} describing the NBD opening and ATP dissociation. For TmrAB, a low dissociation constant $K_{D,ATP}$ = 0.81 ± 0.31 µM has been reported[144], and the transporter should exist in a mainly ATP-bound state at a 1000-fold excess of ATP as was the case in our experiments. Results for evaluating the goodness of fit were good for TMDs and c-NBS and acceptable for the d-NBS, and no consideration of the $OF^{occluded}$ conformation as an intermediate was necessary to model the time-resolved conformational transition. Therefore, while the $OF^{occluded}$ state likely is the intermediate for the IF-to-OF transition, its lifetime appears to be too short to be relevant for the overall kinetics of the process in TmrAB.

So far, only few studies investigated the rate constants of conformational transitions in membrane proteins, and even fewer did so for ABC transporters. For MsbA, several studies that relied on different spectroscopic techniques determined rate constants k_1 for the forward transition or NBD dimerization that varied considerably, with values of 0.25 s^{-1} and 0.49 s^{-1} for full-size MsbA in detergent micelles[150,220], and 20 s^{-1} for full-size MsbA in lipid nanodiscs[152]. These rates are significantly higher than the values obtained in this work for the periplasmic gate opening (0.003 – 0.015 s^{-1}) or c-NBS and d-NBS closure (0.002 – 0.008 s^{-1} and 0.003 – 0.005 s^{-1}, respectively). To further discuss this discrepancy, the activation energies of both systems in detergent micelles have to be considered. The results from MsbA are in agreement with a similarly broad range of ATPase activity observed under different solubilization methods, with 14 s^{-1} in nanodiscs and 2 s^{-1} in detergent micelles and show that the solubilization conditions and the environment of an ABC transporter have a large impact on the kinetics of a transporter.

The ATPase activity assay performed in this work (**Figure 4.11**) at a final ATP concentration of 3 mM and at 68 °C for MTSL-labelled variants of TmrAB gives an ATP

turnover rate of approximately 2 s^{-1}. This value is lower than in previous studies performed on TmrAB, where a turnover rate of 7.5 s^{-1} was reported.[48] Since the ATP concentration there was higher (10 mM) which leads to an increased ATP turnover, and spin-labelled TmrAB shows a decreased activity (for both points, see also **Figure 4.11**), this was expected. In contrast to MsbA, where both the ATPase assays and the kinetic experiments were conducted at the same temperature of 37 °C, the ATPase assays in this thesis were performed at 68 °C and the kinetic experiments at reduced temperatures. For TmrAB, no ATPase activity was detectable at 37 °C.[48] The reduced temperature is therefore one of the reasons for the small rate constants observed here. If the ATPase activity is determined for the same temperatures and concentrations as in the time-resolved experiment, the resulting rates could be compared to see potential correlations of the experimentally isolated forward transition (IF-to-OF) with the ATP turnover.

This leads to the next point that should be considered to understand the obtained rate constants - the fact that ATP hydrolysis was excluded by incubating with ATP-EDTA. The above-mentioned studies on MsbA were performed under turnover conditions. The comparison between the conformational kinetics under non-hydrolyzing and hydrolyzing conditions at the TMDs (**Figure 4.10e**) shows how turnover conditions lead to significantly more transporters in the OF conformation and a faster transition to the OF fraction in the sample. A previous study proposed that turnover conditions would lead to an enrichment of the IF state and suggested the implementation of an additional irreversible rate constant k_2 to characterize the corresponding kinetic model.[219] The opposite is visible here, with an increase of the OF state, and the above model could not fit the experimental data. Due to the assumed complexity of the kinetic model under turnover conditions, no rate constants could be determined for this experiment. Nevertheless, the qualitative characterization leads to important observations. First, the fact that the OF conformation is enhanced is surprising. Since ATP hydrolysis takes place, another pathway to return to the IF conformation is available. It is thus possible that under our experimental turnover conditions, the IF conformation is only shortly reached before the transporter returns to the OF conformation. Alternatively, hydrolysis could also result in an (equally transient) occluded conformation before return to the OF conformation. In both cases, the accumulation of the OF state suggests a significant modulation of the energy landscape of the conformational transitions by the turnover conditions. Interestingly, when substituting ATP with ATPγS, the kinetics reversed to non-hydrolyzing levels, even in the presence of Mg^{2+}. This could show that the presence of Mg^{2+} alone at the NBDs is not sufficient to induce this apparent stabilization of the OF state. However, ATPγS was acquired as a tetralithium salt, and

sample concentrations of 50 mM ATPγS would result in high Li^+ concentrations of 200 mM. Despite their different magnitude of charge, Li^+ is a known competitor for Mg^{2+}, and was shown to inhibit Mg^{2+}-dependent biomolecules.[221,222] To exclude the putative influence of Li^+ presence on our observations, the ATPγS solution should be treated to exchange Li^+ for another, non-competing counterion, such as Na^+. The mechanistic basis for the significant impact of ATP hydrolysis on energetic favorability of the OF conformation remains open and needs to be further investigated.

While the time-resolved data of the TMDs under turnover conditions show the above discussed stabilization of the OF state over the course of the incubation time, the c-NBS shows an initial burst of closure followed by a slow decrease of the closed conformation over the rest of the incubation time (**Figure 4.10f**). The d-NBS does not exhibit this behavior. If we consider that now ATP hydrolysis takes place, the decrease of available free ATP could result in less transporters remaining in the closed c-NBS state. Based on our ATPase assays we can extrapolate that after 60 s, already 10 % of ATP is hydrolyzed. At higher ATP concentrations, as is the case here, the rate of ATP hydrolysis would likely be higher. This could indeed lead to a sufficient loss of available ATP and/or accumulation of ADP (see chapter 5.3). Since the d-NBS has a significantly reduced ATPase activity, this gradual decrease of ATP levels will affect the c-NBS first and more strongly. The fact that we see no sensitivity of the TMDs for the decrease of ATP concentrations indicates that opening of the c-NBS alone is not sufficient for the return of the TMDS to the IF conformation. The question, whether one or both NBSs fully open during a transport cycle is under ongoing debate, and studies show evidence for the opening of one[223] or two[210] NBSs. It is well possible that different transporters exhibit different mechanisms that are predetermined by the underlying conformational kinetics of (symmetric or asymmetric) NBSs and TMDs.

Since the time-resolved experiments under non-hydrolyzing conditions were performed under different temperatures, the temperature dependence of the reaction rates can be characterized using several analytical treatments of the data. Such a characterization of conformational transitions has not been previously performed. In this work, the empirical Arrhenius equation was employed to calculate the activation energy E_a for the conformational transitions. Additionally, the statistical Eyring equation that is based on the transition state theory can be used to calculate the free energy of activation $\Delta G^{\ddagger}$ that contains both the enthalpy $\Delta H^{\ddagger}$ and entropy $\Delta S^{\ddagger}$ needed to reach the transition state. Analysis based on the Eyring equation was beyond the scope of this work.

To calculate E_a using Arrhenius equation, $ln\, k$ was plotted as a function of $1/\mathrm{T}$, and the slope was obtained from linear regression (**Figure 4.8**). The goodness of fit was good for k_1 in TMDs (TmrAB and $TmrA^{EQ}B$) and c-NBS and k_2 in the TMDs for

TmrA^{EQ}B, with corrected R^2 values between 0.78 and 0.99. For k_2 in the TMDs and c-NBS with catalytically active c-NBS, goodness of fit was worse with corrected R^2 values of 0.34 and 0.35. The reverse transition exhibits a slight concave trend in the Arrhenius plot. Non-linear Arrhenius plots can indicate a higher or lower reactivity in dependence of the temperature, for example through a change in the rate-limiting step of a conformational transition.[224] In addition, non-linear behavior has been reported for refolding and aggregation processes, where protein aggregation often displays a concave-up behaviour.[225] With only three temperatures points in the Arrhenius plot, this non-linear behavior cannot be sufficiently analyzed, and more temperature points are necessary for a profound investigation.

Based on the linear treatment of the Arrhenius plots, we determined values for the forward transition of 75 ± 27 kJ/mol (TMDs) and 56 ± 3 kJ/mol (c-NBS). The activation energy for c-NBS closure is smaller, but the activation energy of the TMD opening has a rather large error. It is therefore difficult to conclude whether c-NBS closure precedes TMD opening. Molecular dynamics (MD) simulations on the heterodimeric ABC transporter TM287/288 indicated that NBD dimerization happens first and leads to an occluded state OF^{occluded}, followed by subsequent opening of the periplasmic gate to the OF conformation. We therefore initiated a collaboration to further investigate the coupling of NBS closure to TMD opening by MD simulations in the future. Comparing these results to our experimental data, including the d-NBS, will help to further elucidate the conformational cycle.

Due to the novelty of this analysis, no information from conformational transitions in other biological systems exists that can be directly compared. However, ABC transporters have been analyzed regarding other biochemical features using Arrhenius equation. For the homodimeric lysosomal polypeptide transporter TAPL, the activation energy for peptide transport was determined.[226] A non-linear Arrhenius plot was observed, with higher activation energies between 134 kJ/mol and 178 kJ/mol (depending on the length of peptide substrate) below 36 °C, and lower activations energies between 44 kJ/mol and 77 kJ/mol above. It was hypothesized that structural rearrangements lead to different rate-limiting steps, namely from the IF to an occluded conformation below 36 °C, and from the occluded conformation to the OF state above 36 °C. The range of these described values agrees with our values for the activation energies of c-NBS closure and TMD opening, suggesting that these conformational transitions are the rate-limiting steps for peptide transport. Apart from that, the non-linear Arrhenius plot shows a convex behavior, hence our observed non-linearity (if confirmed) likely has another origin. In another study on TAP, high activation energies for peptide binding (106 kJ/mol) and dissociation (80 kJ/mol) have been determined.[227] Since peptide binding represents an independent step prior to

ATP binding, it can be neglected here. The dissociation of peptide after ATP hydrolysis, however, involves the conformational forward transition that we investigate here. Again, activation energy for peptide dissociation is well in agreement with the activation energy for TMD opening. In a study on the maltose importer $MalFGK_2$, the activation energy of the ATPase activity was calculated depending on presence of its SBP, MalE, and/or maltose, with values of 85 kJ/mol (without MalE or substrate) and 60 kJ/mol (with MalE).[228] Interestingly, these values agree with our results, as well. However, the difference between ABC importer and exporter might be too big to correlate these findings. Nevertheless, it could be that the same underlying conformational transitions define the energetic landscape.

As discussed above, based on our results, the question whether NBS closure and TMD opening occur sequentially or concomitantly during the forward transition cannot be conclusively answered. A repetition of the experiment at further temperature points could enable a more robust analysis of the Arrhenius plots. A further limitation arises from the fact that the key regions of TmrAB (namely c-NBS, d-NBS and TMDs) were probed separately. While all spin-labelled variants showed ATPase and transport activity, an effect of the label position on the quantitative kinetics cannot be ruled out. An elegant yet challenging solution for that would be the combination of the probing positions into one TmrAB variant. For the concomitant NO-NO and Mn^{2+}-NO PELDOR experiment, the same MTSL spin label could be employed for labelling all three cysteine residues, since different, non-overlaying observer pulses were used for the different regions of TmrAB, even if the resulting distances in the different regions fall together. The Mg^{2+}-to-Mn^{2+} substitution approach can't be directly used for the kinetic investigation for two reasons. The removal of excess Mn^{2+} limits the experimental flexibility, this will be discussed in chapter 5.2. Since the presence of Mn^{2+} leads to turnover conditions, the forward transition cannot be isolated from the ATP hydrolysis pathway. Therefore, a set of two covalently linked spin pairs is better suited for such a combined TR-PELDOR experiment. In this case, however, MTSL alone can't be used to label all four positions, as the same pump and observer frequencies to probe two regions with similar expected distances leads to convoluted results. The use of two different, spectroscopically orthogonal spin labels to label different regions could remedy this limitation. Apart from a nitroxide spin label such as MTSL, trityl molecules or Gd^{3+} complexes are potential paramagnetic species to serve as spin labels.[171,172] For this, the labelling strategies must be independent of each other. The use of a genetically encoded spin label has been demonstrated in the last years, where either a spin-labelled noncanonical amino acid is incorporated into a protein[137], or a noncanonical amino acid is incorporated and subsequently spin-labelled using click chemistry[229].

Another approach could be the labelling of double-histidine motifs with Cu^{2+} chelate complexes.[230,231] One labelling strategy could be used for the TMDs, and one for either the c-NBS or d-NBS (or both, using three different strategies), and the time-resolved evolution of both the NBS and TMD conformation could be characterized in the same sample and thus directly correlated.

In addition to the time-resolved experiments in catalytically active TmrAB, the experiment was also performed in $TmrA^{EQ}B$ (**Figure 4.9**). While the stabilization of the OF state by the reduced ATPase activity is known, the significant increase of the activation energy was a surprising result. The E-to-Q mutation leads to stronger temperature dependence of both the forward and reverse transition. Since E_a of the reverse transition increases more (60 kJ/mol) than the forward transition (50 kJ/mol), the equilibrium is shifted towards the OF conformation. This shows that the catalytic glutamate at the center of the c-NBS is key for maintaining the energy landscape required for a functional transport cycle.

In this work, experiments were performed on detergent solubilized TmrAB. While this facilitates sample preparation and improves the signal quality, detergent micelles are no physiological environment for ABC transporters. For MsbA, it was shown that the choice of solubilization method has a significant impact on the kinetics.[160] Therefore, a transfer of the here made observations to more native conditions is an important next step. Also, experiments under physiological nucleotide and Mg^{2+} concentrations could shed further light on the transport cycle under native conditions. However, the results obtained here for the isolated forward transition are valuable for the evaluation of these future findings.

5.2 Investigation of TmrAB using Mn^{2+}-NO PELDOR spectroscopy

The role of Mg^{2+}-mediated ATP hydrolysis is of key importance to understand the function of ABC transporters, especially those that exhibit catalytic asymmetry such as TmrAB. Here, we combined SDSL at singular cysteine residues in the NBDs of TmrAB with Mg^{2+}-to-Mn^{2+} substitution to investigate this asymmetry by Mn^{2+}-NO PELDOR spectroscopy. While Mn^{2+}-NO PELDOR could be already applied to measure the interspin distances in artificial model compounds[192,193], and Mg^{2+}-to-Mn^{2+} substitutions could be used in an ABC transporter to measure the interspin distances between two localized Mn^{2+} ions[195], we determined the interspin distances between Mn^{2+} and a nitroxide spin label for the first time in a large and complex biomolecule. This opens a new approach for the investigation of biological systems that require the

presence of Mg^{2+} ions. In the case of TmrAB, it enabled us to elucidate the differences between the c-NSB and d-NBS, as well as its influence on the conformational cycle of the whole protein.

The ATPase activity assays, as well as probing of the periplasmic gate (**see Figure 4.16**) proved that Mn^{2+} substitution induces the conformational transition to the OF state in an almost identical manner to Mg^{2+}. By employing three different spin label positions at the NBDs (compare **Figures 4.12,4.14**), the following principal observation was made: under turnover conditions with Mn^{2+}–ATP, no distances in the distance distribution could be attributed to an interspin distance between MTSL and the Mn^{2+} ion in the c-NBS. We explained this observation with the fast hydrolysis of ATP at the c-NBS. This explanation is based on the different hydrolysis rates of c-NSB and d-NBS. It is well in line with the functional understanding previously suggested in literature, where the d-NBS of the heterodimeric ABC transporter BmrCD maintains its ATP-bound dimerized conformation, while the c-NBS disengages faster.[51] Through the lack of the corresponding c-NBS distance, we have direct evidence for the asymmetric behavior regarding ATP hydrolysis in TmrAB. The results from all three spin label positions under vanadate-trapping conditions validate that also the c-NBS can harbor Mn^{2+} and that it can be arrested.

Apart from the distinction between c-NBS and d-NBS, the results from the labelled variants A416R1^{A} and L458R1^{B} (**Figure 4.12d,e** and **Figure 4.14c,d**) together showed that both c-NBS and d-NBS only exhibit binding of Mn^{2+}–ATP in their closed conformation, no binding could be detected to the open conformation. Cryo-EM structures suggested the binding of nucleotides (ATP at the d-NBS and ADP at the c-NBS) and Mg^{2+} also to the open conformation of both NBSs.[232] The reason that we could not observe this interaction may be the different experimental conditions. A large amount of ATP and Mg^{2+} (5 - 6 mM, respectively) was present in the cryo-EM samples under turnover conditions. Due to the explained interference of Mn^{2+} with the Mn^{2+}–NO PELDOR measurements, these conditions were not possible and only the ATP concentration was kept at 10 mM. The still present ATP could therefore again bind to the c-NBS and keep it in a closed conformation, as was also the case for our ATP-EDTA experiments (see chapter 4.2.4). Since Mn^{2+} was already removed from the sample, this closed state would be silent and not detectable by Mn^{2+}–NO PELDOR. Nevertheless, the open NBSs clearly show a reduced affinity for nucleotides, which is likely an important feature of their conformational cycle.

In an advanced experimental setup, we combined the just described Mn^{2+}–NO PELDOR experiment with a NO-NO PELDOR measurement that probed the periplasmic gate at the TMDs to correlate two of the most relevant transporter domains and their conformational states. This approach has not been described in literature before.

Recently, orthogonal labelling with Gd^{3+}, trityl, and nitroxide was employed to investigate the heterooligomeric cobalamin transport complex BtuB.[197] In the Mn^{2+}–NO setup used in this work, the sufficiently long distances (8-12 nm) between the two NO spin labels at the TMDs to the one NO spin label at the d-NBS made it possible to use the same spin label for all positions. As for the single-labelled variants, it is difficult to exclude Mn^{2+}-less ATP binding at the c-NBS. There is an important observation to be made here: from the probing of the periplasmic gate, we know that TmrAB exists in both the IF and OF conformation under hydrolyzing conditions (**Figure 4.14**). The observations of the NBSs show that the c-NBS has already lost its ATP-Mn^{2+} due to fast hydrolysis. This means that a significant fraction of transporters is still in the OF conformation, while ATP has already been hydrolyzed at the c-NBS. As discussed above, the fraction of OF transporters could also stem from ATP-only bound transporters (without Mn^{2+}) after removal of Mn^{2+}. However, during the time-resolved Mn^{2+}-NO PELDOR experiment (**Figure 4.16 a,b**), both Mn^{2+} and ATP are removed, and still a significant fraction of transporters remained in the OF conformation. This observation is strong evidence for the asymmetric coupling of c-NBS and d-NBS to the TMDs, and in agreement with cryo-EM structures from TmrAB under turnover conditions where the c-NBS harbors ADP and the d-NBS still contains ATP.[104] In contrast to the cryo-EM data, however, where no OF conformation could be resolved under turnover conditions, this was possible under our experimental conditions. This asymmetric loss of ATP from the OF conformation would require the release of ADP and P_i from a partly engaged c-NBS. This release could take place either through a tunnel in the c-NBS, and/or through a partly opening of the c-NBS to enable nucleotide exchange. A pathway for the release of P_i has been identified for several ABC transporters including TmrAB[104], but the precise mechanism remains to be solved. Interestingly, such release tunnels were found in the heterodimeric ABC transporter TM287/288 only in the c-NBS.[233] In the isolated NBD of the homodimeric HlyB that exhibits asymmetric NBSs through sequential ATP hydrolysis, one such release tunnel is accessible, while the other is closed by two amino acid residues forming a salt bridge.[234] Similarly, phosphate release could be facilitated at the c-NSB in TmrAB, followed by release of ADP. The release of the nucleotide cannot take place through the same narrow tunnel. We hypothesized that ATP hydrolysis at the c-NBS may lead to a partial opening of the c-NBS to release ADP. To further investigate this assumption, cryo-EM samples were prepared under the same conditions. To improve sample quality, these conditions have to be optimized, which was beyond the scope of this work. In addition, the assumption led us to the development of the time-resolved reverse transition experiment discussed in chapter 5.3.

By repeating the concomitant NO-NO and Mn^{2+}-NO PELDOR experiment in catalytically impaired $TmrA^{EQ}B$, occlusion of ATP-Mn^{2+} at the c-NBS could be achieved under turnover conditions. This agrees with cryo-EM structures of TmrAB carrying the E-to-Q mutation that also harbors two ATP in its NBSs.[104] Thus, the E-to-Q substitution leads to a stable occlusion of Mn^{2+}-ATP at the c-NBS and the drastically decreased ATP hydrolysis leads to a larger fraction of transporters being trapped in the OF conformation. While only little ATP-Mn^{2+} was occluded at the c-NBS in the post-hydrolysis state stabilized by vanadate trapping, the E-to-Q substitution led to significantly more occlusion of ATP-Mn^{2+}. The high presence of Mn^{2+} in both NBSs further enabled the measurement of Mn^{2+}-Mn^{2+} PELDOR. The simultaneous determination of NO-NO, Mn^{2+}-NO, and Mn^{2+}-Mn^{2+} interspin distances in the same sample has not been performed before. Several studies suggest that also homodimeric ABC transporters may exhibit asymmetry regarding their NBSs.[44,235] The here developed experimental approach can be applied to homodimeric systems to investigate catalytic asymmetry.

In general, the Mn^{2+}-NO PELDOR experiment is made more difficult by the induced fast relaxation of NO by excess Mn^{2+}. At the same time, Mn^{2+} concentrations during incubation have to be sufficiently high to achieve occlusion at the NBSs. The removal of excess Mn^{2+} using Micro Bio-Spin columns represents an elegant method to avoid unnecessarily fast relaxation of the NO spins. This buffer exchange itself is performed at 4 °C and our results show that at low temperatures, no conformational transitions are observed. Nevertheless, the additional buffer exchange step limits the experimental conditions. In other pulsed EPR studies, the Mn^{2+} concentration was reduced to 2 mM.[236] If this condition could be applied to TmrAB with sufficient occlusion of Mn^{2+} at the NBSs whilst avoiding too fast NO relaxation, the buffer exchange step could be removed, enabling more complex experiments, such as TR-PELDOR of the forward transition with the concomitant observation of TMDs and NBSs.

5.3 Time-resolved Mn^{2+}-NO PELDOR spectroscopy of TmrAB

So far in this work, the forward transition of TmrAB from the IF to the OF state was studied, or the transporter was investigated under turnover conditions. To understand ATP hydrolysis, its order of events and effect on the transport mechanism, it is essential to isolate the ATP hydrolysis pathway from the rest of the transport cycle – similar to the isolation of the non-hydrolysis pathway by ATP-EDTA conditions or

employment of catalytically impaired TmrA^{EQ}B. The experimental conditions discussed in chapter 5.2 gave me the idea to further exploit the buffer exchange step: by removing ATP and Mn^{2+} at the same time, the hydrolysis pathway could be isolated from the other conformational transitions. Computational studies on MalK suggested that ATP removal induces opening of the NBDs.[237] Using concomitant NO-NO and Mn^{2+}-NO PELDOR spectroscopy, the closure of the periplasmic gate could be observed over time, while only the d-NBS harbors an occluded Mn^{2+} that is lost over a time of 5 min (**Figure 4.16**). Quantification of the modulation depth of the Mn^{2+}-NO PELDOR measurements further showed that the closure of the periplasmic gate and the loss of Mn^{2+} from the d-NBS are correlated processes. We observed that in the presence of ATP, a significant c-NBS fraction is in the closed conformation, and the periplasmic gate cannot return to its closed conformation. Only by ATP removal can the return to the IF state be induced, and this is accompanied by the loss of ATP-Mn^{2+} from the c-NBS. Taken together, we concluded that hydrolysis at the c-NBS must be the first step to initiate return of the TMDs to the IF conformation. The hydrolysis of ATP at the c-NBS weakens the NBD dimer sufficiently to energetically facilitate the reverse transition. The loss of the second ATP from the d-NBS would then result in complete dissociation of the NBD dimer and leads to the return of TmrAB to the IF state. This loss of ATP from the d-NBS could occur either through direct dissociation from the binding site, or by slow hydrolysis to ADP followed by dissociation. Based on our observations, we cannot determine which one or whether both of these mechanisms lead to the loss of ATP-Mn^{2+} from the d-NBS. Recently, it was shown for TmrAB that only 50 % of ATP is hydrolyzed during one round of transport, and that one single ATP turnover at the c-NBS launches the return to the IF state[210], indicating that no hydrolysis takes place at the d-NBS. To investigate this in the future within our experimental setup, the identity of the nucleotide phosphates coordinated to Mn^{2+} could be distinguished by ^{31}P- electron-nuclear double resonance (ENDOR) experiments, where ATP and ADP are characterized by different spectral features (or absence thereof). At the same time, the kinetics of ATP turnover could be followed by the signal intensity in ^{31}P- electron-electron double resonance (ELDOR) detected NMR (EDNMR). Both applications have been described in literature.[194] Furthermore, these experiments could be conducted using catalytically impaired TmrA^{EQ}B, where the c-NBS has no ATPase activity and the residual ATPase activity of the d-NBS can be studied. The kinetics of ATP hydrolysis (measured by EDNMR) could then be correlated in the same sample to the loss of Mn^{2+} from the d-NBS and the return of the TMDs to the IF conformation (measured by PELDOR).

The physiological function of the d-NBS is not completely understood, but studies proposed a permanent occupation by an ATP molecule, thus keeping the NBDs

associated, which could facilitate more efficient ATP hydrolysis at the c-NBS.[54] The complete removal of ATP chosen here to initiate the reverse transition is no physiological condition, but it enables us to understand the order of events and dependencies of processes. On the timescale of physiological conditions with 10 mM ATP, where substrate is transported within seconds or faster, the d-NBS could indeed be described to remain in the ATP-bound state, while only the c-NBS rotates quickly through the different hydrolysis states. This theory, however, remains to be proven.

The influence of Mg^{2+} on the reverse transition was further investigated. While the presence of Mn^{2+} in the previously discussed experiment resulted in turnover conditions, TmrAB was now incubated under non-hydrolyzing conditions (**Figures 4.17-4.19**). This means that no Mg^{2+} (or Mn^{2+}) was present during incubation and both NBSs harbor an unhydrolyzed ATP molecule. Subsequent removal of ATP in absence of Mg^{2+} led to a slow and incomplete return to the IF state and open c-NBS, and presence of Mg^{2+} was necessary to achieve complete return. In contrast, the d-NBS showed a complete return to its open state even in absence of Mg^{2+}. As for the NO-NO PELDOR results from chapter 4.2, these observations stem from independent TmrAB variants, and the results can be influenced by differences in the transition kinetics of the variants. However, the distinct difference between the behaviors of c-NBS and d-NBS is likely not only based on these variations. The observations from the TMDs and c-NBS again proves the importance of hydrolysis at the c-NBS for the reverse transition. The observation of return transitions in the complete absence of Mg^{2+} (both during incubation and after ATP removal) could be either due to ATP autohydrolysis or a transient opening of TmrAB induced by thermal energy and subsequent dissociation of ATP. The accelerated return of the d-NBS in comparison to the c-NBS could be explained by a weaker closure of the d-NBS: without hydrolysis taking place, the c-NBS is tightly closed. The d-NBS might exhibit a weaker closure and undergo opening even without hydrolysis taking place, while the c-NBS remains closed and the TMDs remain in the OF conformation until the c-NBS opens slowly. In this scenario, re-opening of the d-NBS was not sufficient to efficiently induce return of the TMDs. When Mn^{2+} was present during the forward transition (compare **Figure 4.17** to **Figure 4.16**), however, the opposite was observed: the opening of the c-NBS was very fast and happened faster than the timescale of the experiment. The TMDs then returned to the IF state together with the opening of the d-NBS. To verify whether the d-NBS can lose its unhydrolyzed ATP independently of the conformational status of the c-NBS as observed in **Figure 4.19**, the concomitant time-resolved NO-NO and Mn^{2+}-NO PELDOR experiment could be repeated in catalytically impaired $TmrA^{EQ}B$. If the hypothesis holds true, the c-NBS would harbor an occluded ATP, while the d-NBS again exhibits a loss of ATP-Mn^{2+} over time. These both cases together could then

indicate that the TMDs need both NBSs to open to return to the IF conformation, but only the c-NBS needs to hydrolyze ATP for that to happen. Since under physiological conditions, both ATP and Mg^{2+} are available, the c-NBS will hydrolyze and open faster and the d-NBS will open more slowly and thus regulate the return of the TMDs to the IF conformation.

Interestingly, an ADP concentration of 10 mM had an accelerating influence on the reverse transition. ADP is a known inhibitor of the ATPase activity in ABC transporters.[238] On the other side, the case of increased ATP hydrolysis by ADP was reported for the multidrug resistance-associated protein (MRP) for low ADP concentrations up to 1 mM, while high concentrations above 4 mM showed an inhibitory effect.[239] An ADP concentration of 10 mM should therefore have an inhibiting effect on ATP hydrolysis. However, with the removal of excess ATP, only one round of (already occluded) ATP hydrolysis can take place, which is likely not directly affected by the sample concentration of ADP. It could rather be that ADP acts as a binding competitor to ATP in the d-NBS, and by replacing unhydrolyzed ATP there accelerates the reverse transition. This is supported by the control experiment in catalytically impaired $TmrA^{EQ}B$: here, ADP exhibits no effect on the reverse transition because without ATP hydrolysis at the c-NBS, the NBD dimer is sufficiently stabilized and ATP-ADP exchange at the d-NBS has little effect on return to the IF state.

Like ADP, a sample concentration of 50 µM (1:1) substrate had an accelerating effect on the reverse transition. This was a surprising observation and has not been described before in literature. Since this affect was not observable in the E-to-Q background, it can be suggested that this acceleration is a post-hydrolytic effect, too. After ATP hydrolysis at the c-NBS and the resulting weakening of the NBD dimer and the OF conformation as a whole, the substrate could interact with the now energetically more accessible IF conformation to which it shows a high affinity, thus stabilizing the IF state and accelerating the return to it. This hypothesis, however, remains to be verified, and a control experiment using a different substrate could prove as informative to rule out the influence of the specific substrate employed here.

The observation of the reverse transition at key regions of TmrAB in a time-resolved manner enables the determination of kinetic parameters for the reverse transition. This will be an important next step in characterizing the kinetics of the whole transport cycle. For this, an appropriate kinetic model has to be used. It could be possible that a monomolecular irreversible model can be employed to describe the transitions between OF and IF state (or closed and open NBSs, respectively). However, the influence of ATP hydrolysis and dissociation on the return kinetics must be carefully assessed and may be considered in the kinetic model to obtain profound values for the rate constants. A subsequent temperature-dependent analysis of the

reverse transition will then yield the activation energy for the return to the IF conformation as an isolated pathway from the ATP-bound state. Together with the results from chapter 4.2.5 where the activation energy was obtained for the isolated forward transition, this will elucidate the kinetics of the complex transitions of TmrAB under physiological turnover conditions.

5.4 Summary

Taken together, the results presented here deepen our understanding of the transport cycle in heterodimeric ABC transporters. In **Figure 5.1**, the transport mechanism in TmrAB is detailed based on these new insights. We could show that the dimerization of the NBSs and opening of the periplasmic gate are energetically uphill processes, and without ATP binding at the NBSs, the IF conformation is the favored state even at increased temperatures. Thermal energy may be sufficient for NBD dimerization even without ATP as was shown for the transporter McjD.[156] But only binding of ATP stabilizes the OF conformation sufficiently to enable substrate transport (**Figure 5.1**, step 1 to 2).

In the IF-to-OF transition, the forward transition has an activation energy that is approximately 30 kJ/mol higher than the reverse transition. At the high physiological temperatures of TmrAB, the forward transition will be favored. It is possible that NBS closure and TMD opening happen sequentially through an occluded intermediate, or simultaneously. ATP hydrolysis at the c-NBS subsequently destabilizes the OF state and is the trigger to accelerate reverse transition (step 2 to 3). This might create an intermediate occluded state, which fully reverses towards the IF conformation with an accelerated rate (step 4). Having a drastically reduced ATPase activity, the d-NBS stably binds ATP. This in effect prevents complete opening of (both) NBS and leads to an asymmetric post-hydrolytic state. It was shown that ATP hydrolysis is in several systems uncoupled from substrate transport, meaning that a transporter hydrolyzes ATP even without substrate present.[226] On the other side, heterodimeric transporters such as TAP exhibit strict coupling between ATP hydrolysis and substrate transport.[240] The slow hydrolysis rate of d-NBS could serve as a cellular 'energy-saving mode'. With a thus modified energy landscape, a heterodimeric ABC transporter is able to access both IF and OF conformation without the necessity to hydrolyze both ATPs in a transport cycle. It could also increase the lifetime of the OF conformation and allow substrate to be release from the low-affinity binding pocket. The overall equilibrium might be regulated through an interplay between Mg^{2+}–ATP, Mg^{2+}–ADP, and substrate concentrations as well as the rates for forward and reverse transitions.

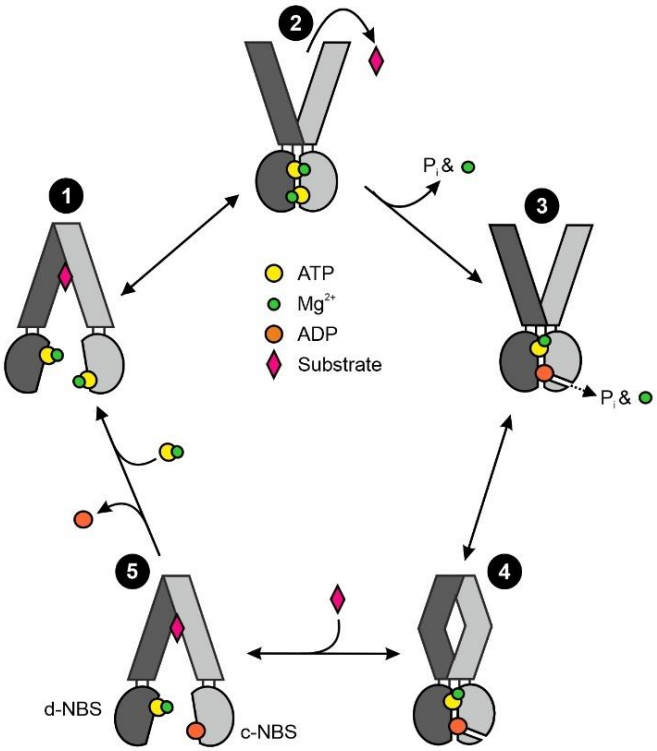

Figure 5.1. Mechanism for substrate translocation in TmrAB. Substrate can bind to the high affinity IF conformation (1) and binding of ATP induces transition to the OF conformation and substrate release from the low affinity binding pocket (2). Afterwards, ATP hydrolysis at the c-NBS (3) and immediate Pi and Mg^{2+} release through a previously identified path in the closed conformation takes place (3). The TMDs could also adopt an occluded conformation (4) before further transitioning to the IF conformation (5). This step may be regulated through an opening and loss of ATP from the d-NBS. This reverse transition (towards the IF conformation) is accelerated in presence of ADP, substrate and most significantly under hydrolyzing conditions. Finally, substrate binds again to the IF conformation and replacement of Mg^{2+}-ADP with Mg^{2+}-ATP resets the transport cycle to start the next round of transport.

6 OUTLOOK

The time-resolved preparation of samples combined with a temperature-dependent observation of the conformational distributions by PELDOR spectroscopy opens up a new methodology to investigate the kinetics in biomolecules. It can help to fully understand the complex pathways of conformational transitions. Together with the strategic combination of experimental conditions with different paramagnetic probes, important aspects of the function of ABC transporters can be elucidated. But new questions emerged, too, and there remain many challenges and opportunities. In what way differ catalytically symmetric transporters from their asymmetric counterparts? How does ATP hydrolysis mechanistically affect the conformational kinetics? How do the biophysical properties of the lipid membrane affect the activity of ABC transporters? How does the presence of substrate affect the forward transition?

For these questions, the dynamic properties of ABC transporters are of central importance. A new emerging field that is gathering considerable momentum is time-resolved cryo-EM (trEM).[241] By shortening the reaction and freezing times, short-lived intermediates could be enriched in the pre-equilibrium states, making snapshots of a whole biomolecule during its conformational transitions accessible. This will likely prove to be an impressive new tool for the functional investigation of proteins. However, the requirements for this technique are in every way enormous.[242] Experimentally flexible approaches that yield high-resolution information about dynamic properties of protein conformations, such as PELDOR spectroscopy, will therefore remain crucial for the investigation of ABC transporters.

In the end, the great challenge will be the translation of our mechanistic understanding into new therapies against diseases based on ABC transporter disorders or MDR. This will involve different and complementary scientific fields working together, with yet unknown and exciting techniques waiting to be discovered.

REFERENCES

1. Deamer, D. Membranes and the Origin of Life: A Century of Conjecture. *J. Mol. Evol.* **83**, 159–168 (2016).

2. Birch, J. *et al.* Changes in membrane protein structural biology. *Biology (Basel).* **9**, 1–31 (2020).

3. Yin, H. & Flynn, A. D. Drugging Membrane Protein Interactions. *Annu. Rev. Biomed. Eng.* **18**, 51–76 (2016).

4. Stillwell, W. Membrane Transport. *An Introd. to Biol. Membr.* 423–451 (2016) doi:10.1016/b978-0-444-63772-7.00019-1.

5. King, R. B. Modeling Membrane Transport. *Adv. Food Nutr. Res.* **40**, 243–262 (1996).

6. Cho, I., Jackson, M. R. & Swift, J. Roles of Cross-Membrane Transport and Signaling in the Maintenance of Cellular Homeostasis. *Cell. Mol. Bioeng.* **9**, 234–246 (2016).

7. Gastaldi, G. *et al.* Energy depletion differently affects membrane transport and intracellular metabolism of riboflavin taken up by isolated rat enterocytes. *J. Nutr.* **129**, 406–409 (1999).

8. Czuba, L. C., Hillgren, K. M. & Swaan, P. W. Post-translational modifications of transporters. *Pharmacol. Ther.* **192**, 88–99 (2018).

9. Okamoto, C. T. Regulation of transporters and channels by membrane-trafficking complexes in epithelial cells. *Cold Spring Harb. Perspect. Biol.* **9**, 1–20 (2017).

10. Dean, M. & Annilo, T. Evolution of the ATP-binding cassette (ABC) transporter superfamily in vertebrates. *Annu. Rev. Genomics Hum. Genet.* **6**, 123–142 (2005).

11. Wang, B., Dukarevich, M., Sun, E. I., Yen, M. R. & Saier, M. H. Membrane Porters of ATP-Binding Cassette Transport Systems Are Polyphyletic. *J. Membr. Biol.* **231**, 1–10 (2009).

12. Hyde, S. C. *et al.* Structural model of ATP-binding proteing associated with cystic fibrosis, multidrug resistance and bacterial transport. *Nature* **346**, 362–365 (1990).

13. Gil-Martins, E., Barbosa, D. J., Silva, V., Remião, F. & Silva, R. Dysfunction of ABC transporters at the blood-brain barrier: Role in neurological disorders. *Pharmacol. Ther.* **213**, 107554 (2020).

14. Greene, N. P., Kaplan, E., Crow, A. & Koronakis, V. Antibiotic Resistance Mediated by the MacB ABC Transporter Family: A Structural and Functional Perspective. *Front.*

Microbiol. **9**, 950 (2018).

15. Robey, R. W. *et al.* Revisiting the role of ABC transporters in multidrug-resistant cancer. *Nat. Rev. Cancer* **18**, 452–464 (2018).

16. Rees, D. C., Johnson, E. & Lewinson, O. ABC transporters: The power to change. *Nature Reviews Molecular Cell Biology* vol. 10 218–227 (2009).

17. Linton, K. J. & Higgins, C. F. MicroGenomics The Escherichia coli ATP-binding cassette (ABC) proteins. **28**, 5–13 (1998).

18. Thomas, C. & Tampé, R. Multifaceted structures and mechanisms of ABC transport systems in health and disease. *Current Opinion in Structural Biology* vol. **51** 116–128 (2018).

19. Hopfner, K. P. *et al.* Structural biology of Rad50 ATPase: ATP-driven conformational control in DNA double-strand break repair and the ABC-ATPase superfamily. *Cell* **101**, 789–800 (2000).

20. Hung, L. W. *et al.* Crystal structure of the ATP-binding subunit of an ABC transporter. *Nature* **396**, 703–707 (1998).

21. Vetter, I. R. & Wittinghofer, A. Nucleoside triphosphate-binding proteins: different scaffolds to achieve phosphoryl transfer. *Q. Rev. Biophys.* **32**, 1–56 (1999).

22. Walker, J. E., Saraste, M., Runswick, M. J. & Gay, N. J. Distantly related sequences in the alpha- and beta-subunits of ATP synthase, myosin, kinases and other ATP-requiring enzymes and a common nucleotide binding fold. *EMBO J.* **1**, 945–951 (1982).

23. Thomas, C. & Tampé, R. Structural and Mechanistic Principles of ABC Transporters. *Annu. Rev. Biochem.* **89**, 605–636 (2020).

24. ter Beek, J., Guskov, A. & Slotboom, D. J. Structural diversity of ABC transporters. *J. Gen. Physiol.* **143**, 419–435 (2014).

25. Oldham, M. L. & Chen, J. Snapshots of the maltose transporter during ATP hydrolysis. *Proc. Natl. Acad. Sci. U. S. A.* **108**, 15152–15156 (2011).

26. Grossmann, N. *et al.* Mechanistic determinants of the directionality and energetics of active export by a heterodimeric ABC transporter. *Nat. Commun.* **5**, 5419 (2014).

27. Zheng, W. H. *et al.* Evolutionary relationships of ATP-Binding Cassette (ABC) uptake porters. *BMC Microbiol.* **13**, 98 (2013).

28. Karpowich, N. *et al.* Crystal structures of the MJ1267 ATP binding cassette reveal an induced-fit effect at the ATPase active site of an ABC transporter. *Structure* **9**, 571–586 (2001).

29. Gerber, S., Comellas-Bigler, M., Goetz, B. A. & Locher, K. P. Structural basis of trans-inhibition in a molybdate/tungstate ABC transporter. *Science* **321**, 246–250 (2008).

30. Kadaba, N. S., Kaiser, J. T., Johnson, E., Lee, A. & Rees, D. C. The high-affinity E. coli methionine ABC transporter: structure and allosteric regulation. *Science* **321**, 250–253 (2008).

31. Locher, K. P. Mechanistic diversity in ATP-binding cassette (ABC) transporters. *Nat. Struct. Mol. Biol.* **23**, 487–493 (2016).

32. Matte, A., Tari, L. W. & Delbaere, L. T. J. How do kinases transfer phosphoryl groups? *Structure* **6**, 413–419 (1998).

33. Moody, J. E., Millen, L., Binns, D., Hunt, J. F. & Thomas, P. J. Cooperative, ATP-dependent Association of the Nucleotide Binding Cassettes during the Catalytic Cycle of ATP-binding Cassette Transporters*. *J. Biol. Chem.* **277**, 21111–21114 (2002).

34. Urbatsch, I. L. *et al.* Mutational Analysis of Conserved Carboxylate Residues in the Nucleotide Binding Sites of P-Glycoprotein. *Biochemistry* **39**, 14138–14149 (2000).

35. Geourjon, C. *et al.* A common mechanism for ATP hydrolysis in ABC transporter and helicase superfamilies. *Trends Biochem. Sci.* **26**, 539–544 (2001).

36. Zaitseva, J., Jenewein, S., Jumpertz, T., Holland, I. B. & Schmitt, L. H662 is the linchpin of ATP hydrolysis in the nucleotide-binding domain of the ABC transporter HlyB. *EMBO J.* **24**, 1901–1910 (2005).

37. Scheffzek, K., Kliche, W., Wiesmüller, L. & Reinstein, J. Crystal Structure of the Complex of UMP/CMP Kinase from Dictyostelium discoideum and the Bisubstrate Inhibitor P1-(5'-Adenosyl) P5-(5'-Uridyl) Pentaphosphate (UP5A) and Mg2+ at 2.2 Å: Implications for Water-Mediated Specificity. *Biochemistry* **35**, 9716–9727 (1996).

38. Abele, U. & Schulz, G. E. High-resolution structures of adenylate kinase from yeast ligated with inhibitor Ap5A, showing the pathway of phosphoryl transfer. *Protein Sci.* **4**, 1262–1271 (1995).

39. Szöllősi, D., Szakács, G., Chiba, P. & Stockner, T. Dissecting the Forces that Dominate Dimerization of the Nucleotide Binding Domains of ABCB1. *Biophys. J.* **114**, 331–342 (2018).

40. Cotten, J. F., Ostedgaard, L. S., Carson, M. R. & Welsh, M. J. Effect of cystic fibrosis-associated mutations in the fourth intracellular loop of cystic fibrosis transmembrane conductance regulator. *J. Biol. Chem.* **271**, 21279–21284 (1996).

41. Currier, S. J. *et al.* Identification of residues in the first cytoplasmic loop of P-glycoprotein involved in the function of chimeric human MDR1-MDR2 transporters. *J. Biol. Chem.* **267**, 25153–25159 (1992).

42. Dawson, R. J. P. & Locher, K. P. Structure of a bacterial multidrug ABC transporter. *Nature* **443**, 180–185 (2006).

43. Loo, T. W., Bartlett, M. C. & Clarke, D. M. Human P-glycoprotein contains a greasy ball-and-socket joint at the second transmission interface. *J. Biol. Chem.* **288**, 20326–20333 (2013).

44. Mittal, A., Böhm, S., Grütter, M. G., Bordignon, E. & Seeger, M. A. Asymmetry in the homodimeric ABC transporter MsbA recognized by a DARPin. *J. Biol. Chem.* **287**, 20395–20406 (2012).

45. Procko, E., O'Mara, M. L., Bennett, W. F. D., Tieleman, D. P. & Gaudet, R. The mechanism of ABC transporters: general lessons from structural and functional studies of an antigenic peptide transporter. *FASEB J. Off. Publ. Fed. Am. Soc. Exp. Biol.* **23**, 1287–1302 (2009).

46. Seyffer, F. & Tampé, R. ABC transporters in adaptive immunity. *Biochim. Biophys. Acta* **1850**, 449–460 (2015).

47. Hohl, M., Briand, C., Grütter, M. G. & Seeger, M. A. Crystal structure of a heterodimeric ABC transporter in its inward-facing conformation. *Nat. Struct. Mol. Biol.* **19**, 395–402 (2012).

48. Zutz, A. *et al.* Asymmetric ATP hydrolysis cycle of the heterodimeric multidrug ABC transport complex TmrAB from Thermus thermophilus. *J. Biol. Chem.* **286**, 7104–7115 (2011).

49. Stockner, T., Gradisch, R. & Schmitt, L. The role of the degenerate nucleotide binding site in type I ABC exporters. *FEBS Lett.* **594**, 3815–3838 (2020).

50. Goda, K. *et al.* Human ABCB1 with an ABCB11-like degenerate nucleotide binding site maintains transport activity by avoiding nucleotide occlusion. *PLoS Genet.* **16**, e1009016 (2020).

51. Mishra, S. *et al.* Conformational dynamics of the nucleotide binding domains and the power stroke of a heterodimeric ABC transporter. *Elife* **3**, e02740 (2014).

52. Csanády, L., Vergani, P. & Gadsby, D. C. Structure, Gating, and Regulation of the CFTR Anion Channel. *Physiol. Rev.* **99**, 707–738 (2018).

53. Szöllősi, D., Chiba, P., Szakacs, G. & Stockner, T. Conversion of chemical to mechanical energy by the nucleotide binding domains of ABCB1. *Sci. Rep.* **10**, 2589 (2020).

54. Tsai, M.-F., Li, M. & Hwang, T.-C. Stable ATP binding mediated by a partial NBD dimer of the CFTR chloride channel. *J. Gen. Physiol.* **135**, 399–414 (2010).

55. Hohl, M. *et al.* Structural basis for allosteric cross-talk between the asymmetric nucleotide binding sites of a heterodimeric ABC exporter. *Proc. Natl. Acad. Sci. U. S. A.*

111, 11025–11030 (2014).

56. Dean, M., Rzhetsky, A. & Allikmets, R. The human ATP-binding cassette (ABC) transporter superfamily. *Genome Res.* **11**, 1156–1166 (2001).

57. Gadsby, D. C., Vergani, P. & Csanády, L. The ABC protein turned chloride channel whose failure causes cystic fibrosis. *Nature* **440**, 477–483 (2006).

58. Thomas, C. *et al.* Structural and functional diversity calls for a new classification of ABC transporters. *FEBS Lett.* **594**, 3767–3775 (2020).

59. Oldham, M. L., Khare, D., Quiocho, F. A., Davidson, A. L. & Chen, J. Crystal structure of a catalytic intermediate of the maltose transporter. *Nature* **450**, 515–521 (2007).

60. Leisico, F. *et al.* Multitask ATPases (NBDs) of bacterial ABC importers type I and their interspecies exchangeability. *Sci. Rep.* **10**, 19564 (2020).

61. Scheepers, G. H., Lycklama A Nijeholt, J. A. & Poolman, B. An updated structural classification of substrate-binding proteins. *FEBS Lett.* **590**, 4393–4401 (2016).

62. Quiocho, F. A. & Ledvina, P. S. Atomic structure and specificity of bacterial periplasmic receptors for active transport and chemotaxis: variation of common themes. *Mol. Microbiol.* **20**, 17–25 (1996).

63. Korkhov, V. M., Mireku, S. A. & Locher, K. P. Structure of AMP-PNP-bound vitamin B12 transporter BtuCD-F. *Nature* **490**, 367–372 (2012).

64. Rice, A. J., Park, A. & Pinkett, H. W. Diversity in ABC transporters: type I, II and III importers. *Crit. Rev. Biochem. Mol. Biol.* **49**, 426–437 (2014).

65. Joseph, B., Korkhov, V. M., Yulikov, M., Jeschke, G. & Bordignon, E. Conformational cycle of the vitamin B12 ABC importer in liposomes detected by double electron-electron resonance (DEER). *J. Biol. Chem.* **289**, 3176–3185 (2014).

66. Rodionov, D. A. *et al.* A novel class of modular transporters for vitamins in prokaryotes. *J. Bacteriol.* **191**, 42–51 (2009).

67. Xu, K. *et al.* Crystal structure of a folate energy-coupling factor transporter from Lactobacillus brevis . *Nature* **497**, 268–271 (2013).

68. Swier, L. J. Y. M., Guskov, A. & Slotboom, D. J. Structural insight in the toppling mechanism of an energy-coupling factor transporter. *Nat. Commun.* **7**, 11072 (2016).

69. Majsnerowska, M. *et al.* Substrate-Induced Conformational Changes in the S-Component ThiT from an Energy Coupling Factor Transporter. *Structure* **21**, 861–867 (2013).

70. Mi, W. *et al.* Structural basis of MsbA-mediated lipopolysaccharide transport. *Nature*

549, 233–237 (2017).

71. Wong, K., Ma, J., Rothnie, A., Biggin, P. C. & Kerr, I. D. Towards understanding promiscuity in multidrug efflux pumps. *Trends Biochem. Sci.* **39**, 8–16 (2014).

72. Badiee, S. A., Isu, U. H., Khodadadi, E. & Moradi, M. The Alternating Access Mechanism in Mammalian Multidrug Resistance Transporters and Their Bacterial Homologs. *Membranes (Basel).* **13**, (2023).

73. Stefan, E., Hofmann, S. & Tampé, R. A single power stroke by ATP binding drives substrate translocation in a heterodimeric ABC transporter. *Elife* **9**, e55943 (2020).

74. Bi, Y., Mann, E., Whitfield, C. & Zimmer, J. Architecture of a channel-forming O-antigen polysaccharide ABC transporter. *Nature* **553**, 361–365 (2018).

75. Liu, F., Lee, J. & Chen, J. Molecular structures of the eukaryotic retinal importer ABCA4. *Elife* **10**, (2021).

76. Szöllősi, D., Rose-Sperling, D., Hellmich, U. A. & Stockner, T. Comparison of mechanistic transport cycle models of ABC exporters. *Biochim. Biophys. Acta - Biomembr.* **1860**, 818–832 (2018).

77. Manolaridis, I. *et al.* Cryo-EM structures of a human ABCG2 mutant trapped in ATP-bound and substrate-bound states. *Nature* **563**, 426–430 (2018).

78. Caffalette, C. A., Corey, R. A., Sansom, M. S. P., Stansfeld, P. J. & Zimmer, J. A lipid gating mechanism for the channel-forming O antigen ABC transporter. *Nat. Commun.* **10**, 824 (2019).

79. Luo, Q. *et al.* Structural basis for lipopolysaccharide extraction by ABC transporter LptB(2)FG. *Nat. Struct. Mol. Biol.* **24**, 469–474 (2017).

80. Li, Y., Orlando, B. J. & Liao, M. Structural basis of lipopolysaccharide extraction by the LptB(2)FGC complex. *Nature* **567**, 486–490 (2019).

81. Owens, T. W. *et al.* Structural basis of unidirectional export of lipopolysaccharide to the cell surface. *Nature* **567**, 550–553 (2019).

82. Fitzpatrick, A. W. P. *et al.* Structure of the MacAB-TolC ABC-type tripartite multidrug efflux pump. *Nat. Microbiol.* **2**, 17070 (2017).

83. Du, D. *et al.* Multidrug efflux pumps: structure, function and regulation. *Nat. Rev. Microbiol.* **16**, 523–539 (2018).

84. Crow, A., Greene, N. P., Kaplan, E. & Koronakis, V. Structure and mechanotransmission mechanism of the MacB ABC transporter superfamily. *Proc. Natl. Acad. Sci. U. S. A.* **114**, 12572–12577 (2017).

85. Moore, J. M., Bell, E. L., Hughes, R. O. & Garfield, A. S. ABC transporters: human disease and pharmacotherapeutic potential. *Trends Mol. Med.* **29**, 152–172 (2023).

86. Alam, A. & Locher, K. P. Structure and Mechanism of Human ABC Transporters. *Annu. Rev. Biophys.* **52**, 275–300 (2023).

87. Navarro-Quiles, C., Mateo-Bonmatí, E. & Micol, J. L. ABCE Proteins: From Molecules to Development. *Front. Plant Sci.* **9**, 1125 (2018).

88. Skuodas, S. *et al.* The ABCF gene family facilitates disaggregation during animal development. *Mol. Biol. Cell* **31**, 1324–1345 (2020).

89. Kitai, K. *et al.* The lysosomal protein ABCD4 can transport vitamin B(12) across liposomal membranes in vitro. *J. Biol. Chem.* **296**, 100654 (2021).

90. Tinker, A., Aziz, Q. & Thomas, A. The role of ATP-sensitive potassium channels in cellular function and protection in the cardiovascular system. *Br. J. Pharmacol.* **171**, 12–23 (2014).

91. Stockner, T., Gradisch, R. & Schmitt, L. The role of the degenerate nucleotide binding site in type I ABC exporters. *FEBS Lett.* **594**, 3815–3838 (2020).

92. Dean, M., Moitra, K. & Allikmets, R. The human ATP-binding cassette (ABC) transporter superfamily. *Hum. Mutat.* **43**, 1162–1182 (2022).

93. Chaplin, D. D. Overview of the immune response. *J. Allergy Clin. Immunol.* **125**, S3-23 (2010).

94. Wajant, H. Principles and mechanisms of CD95 activation. *Biol. Chem.* **395**, 1401–1416 (2014).

95. Kisselev, A. F., Akopian, T. N., Castillo, V. & Goldberg, A. L. Proteasome active sites allosterically regulate each other, suggesting a cyclical bite-chew mechanism for protein breakdown. *Mol. Cell* **4**, 395–402 (1999).

96. Eggensperger, S. & Tampé, R. The transporter associated with antigen processing: a key player in adaptive immunity. **396**, 1059–1072 (2015).

97. Uebel, S. *et al.* Recognition principle of the TAP transporter disclosed by combinatorial peptide libraries. *Proc. Natl. Acad. Sci. U. S. A.* **94**, 8976–8981 (1997).

98. Lankat-Buttgereit, B. & Tampé, R. The transporter associated with antigen processing: function and implications in human diseases. *Physiol. Rev.* **82**, 187–204 (2002).

99. Goldsmith, K., Chen, W., Johnson, D. C. & Hendricks, R. L. Infected cell protein (ICP)47 enhances herpes simplex virus neurovirulence by blocking the CD8+ T cell response. *J. Exp. Med.* **187**, 341–348 (1998).

100. Verweij, M. C. *et al.* Structural and functional analysis of the TAP-inhibiting UL49.5 proteins of varicelloviruses. *Mol. Immunol.* **48**, 2038–2051 (2011).

101. Wycisk, A. I. *et al.* Epstein-Barr viral BNLF2a protein hijacks the tail-anchored protein insertion machinery to block antigen processing by the transport complex TAP. *J. Biol. Chem.* **286**, 41402–41412 (2011).

102. Koppers-Lalic, D. *et al.* Varicellovirus UL49.5 Proteins Differentially Affect the Function of the Transporter Associated with Antigen Processing, TAP. *PLOS Pathog.* **4**, e1000080 (2008).

103. Nöll, A. *et al.* Crystal structure and mechanistic basis of a functional homolog of the antigen transporter TAP. (2017) doi:10.1073/pnas.1620009114.

104. Hofmann, S. *et al.* Conformation space of a heterodimeric ABC exporter under turnover conditions. *Nature* **571**, 580–583 (2019).

105. Xue, M., Cheng, L., Faustino, I., Guo, W. & Marrink, S. J. Molecular Mechanism of Lipid Nanodisk Formation by Styrene-Maleic Acid Copolymers. *Biophys. J.* **115**, 494–502 (2018).

106. Xue, M., Cheng, L., Faustino, I., Guo, W. & Marrink, S. J. Molecular Mechanism of Lipid Nanodisk Formation by Styrene-Maleic Acid Copolymers. *Biophys. J.* **115**, 494–502 (2018).

107. Engel, A. & Gaub, H. E. Structure and mechanics of membrane proteins. *Annu. Rev. Biochem.* **77**, 127–148 (2008).

108. Columbus, L. & Hubbell, W. L. A new spin on protein dynamics. *Trends Biochem. Sci.* **27**, 288–295 (2002).

109. Huxford, T. X-Ray Crystallography. *Brenner's Encycl. Genet. Second Ed.* 366–368 (2013) doi:10.1016/B978-0-12-374984-0.01657-0.

110. Claxton, D. P., Kazmier, K., Mishra, S. & McHaourab, H. S. Navigating Membrane Protein Structure, Dynamics, and Energy Landscapes Using Spin Labeling and EPR Spectroscopy. *Methods Enzymol.* **564**, 349–387 (2015).

111. Acharya, K. R. & Lloyd, M. D. The advantages and limitations of protein crystal structures. *Trends Pharmacol. Sci.* **26**, 10–14 (2005).

112. Liang, B., Tamm, L. K. & Struct Mol Biol Author manuscript, N. NMR as a Tool to Investigate Membrane Protein Structure, Dynamics and Function HHS Public Access Author manuscript. *Nat Struct Mol Biol* **23**, 468–474 (2016).

113. Chatham, J. C. & Blackband, S. J. Nuclear magnetic resonance spectroscopy and imaging in animal research. *ILAR J.* **42**, 189–208 (2001).

114. Kainosho, M. *et al.* Optimal isotope labelling for NMR protein structure determinations. *Nature* **440**, 52–57 (2006).

115. Reif, B., Ashbrook, S. E., Emsley, L. & Hong, M. Solid-state NMR spectroscopy. *Nat. Rev. Methods Prim.* **1**, (2021).

116. Lilly Thankamony, A. S., Wittmann, J. J., Kaushik, M. & Corzilius, B. Dynamic nuclear polarization for sensitivity enhancement in modern solid-state NMR. *Prog. Nucl. Magn. Reson. Spectrosc.* **102**–**103**, 120–195 (2017).

117. Kaur, H. *et al.* The ABC exporter MsbA probed by solid state NMR – challenges and opportunities. *Biol. Chem.* **396**, 1135–1149 (2015).

118. Lacabanne, D. *et al.* Solid-State NMR Reveals Asymmetric ATP Hydrolysis in the Multidrug ABC Transporter BmrA. *J. Am. Chem. Soc.* **144**, 12431–12442 (2022).

119. Hurtley, S. M. Continuing the resolution revolution. *Science (80-.).* **360**, 282 (2018).

120. Carroni, M. & Saibil, H. R. Cryo electron microscopy to determine the structure of macromolecular complexes. *Methods* **95**, 78–85 (2016).

121. Sgro, G. G. & Costa, T. R. D. Cryo-EM Grid Preparation of Membrane Protein Samples for Single Particle Analysis. *Front. Mol. Biosci.* **5**, 1–8 (2018).

122. Chari, A. & Stark, H. Prospects and Limitations of High-Resolution Microscopy. (2023).

123. Gust, A. *et al.* A starting point for fluorescence-based single-molecule measurements in biomolecular research. *Molecules* **19**, 15824–15865 (2014).

124. Broussard, J. A. & Green, K. J. Research Techniques Made Simple: Methodology and Applications of Förster Resonance Energy Transfer (FRET) Microscopy. *J. Invest. Dermatol.* **137**, e185–e191 (2017).

125. Bartels, K., Lasitza-Male, T., Hofmann, H. & Löw, C. Single-Molecule FRET of Membrane Transport Proteins. *ChemBioChem* **22**, 2657–2671 (2021).

126. Bajar, B. T., Wang, E. S., Zhang, S., Lin, M. Z. & Chu, J. A guide to fluorescent protein FRET pairs. *Sensors (Switzerland)* **16**, 1–24 (2016).

127. D. Goldfarb, S. S. *EPR spectroscopy - fundamentals and methods*. (2018).

128. Hofmann, L. & Ruthstein, S. EPR Spectroscopy Provides New Insights into Complex Biological Reaction Mechanisms. *J. Phys. Chem. B* **126**, 7486–7494 (2022).

129. Senesi, G. S. & Senesi, N. Electron paramagnetic resonance spectroscopy: Part I Historiccal Perspectives. *Ref. Modul. Earth Syst. Environ. Sci.* 519–532 (2023) doi:10.1016/B978-0-12-822974-3.00071-9.

130. Jeschke, G. The contribution of modern EPR to structural biology. *Emerg. Top. Life Sci.*

2, 9–18 (2018).

131. Claxton, D. P., Kazmier, K., Mishra, S. & Mchaourab, H. S. Chapter Twelve - Navigating Membrane Protein Structure, Dynamics, and Energy Landscapes Using Spin Labeling and EPR Spectroscopy. in *Electron Paramagnetic Resonance Investigations of Biological Systems by Using Spin Labels, Spin Probes, and Intrinsic Metal Ions, Part B* (eds. Qin, P. Z. & Warncke, K. B. T.-M. in E.) vol. 564 349–387 (Academic Press, 2015).

132. Hustedt, E. J., Smirnov, A. I., Laub, C. F., Cobb, C. E. & Beth, A. H. Molecular distances from dipolar coupled spin-labels: the global analysis of multifrequency continuous wave electron paramagnetic resonance data. *Biophys. J.* **72**, 1861–1877 (1997).

133. Roser, P., Schmidt, M. J., Drescher, M. & Summerer, D. Site-directed spin labeling of proteins for distance measurements in vitro and in cells. *Org. Biomol. Chem.* **14**, 5468–5476 (2016).

134. Yang, Y. *et al.* A Reactive, Rigid GdIII Labeling Tag for In-Cell EPR Distance Measurements in Proteins. *Angew. Chemie Int. Ed.* **56**, 2914–2918 (2017).

135. Galazzo, L. *et al.* The ABC transporter MsbA adopts the wide inward-open conformation in E. coli cells. *Sci. Adv.* **8**, eabn6845 (2022).

136. Widder, P., Schuck, J., Summerer, D. & Drescher, M. Combining site-directed spin labeling in vivo and in-cell EPR distance determination. *Phys. Chem. Chem. Phys.* **22**, 4875–4879 (2020).

137. Schmidt, M. J., Borbas, J., Drescher, M. & Summerer, D. A Genetically Encoded Spin Label for Electron Paramagnetic Resonance Distance Measurements. *J. Am. Chem. Soc.* **136**, 1238–1241 (2014).

138. Ketter, S. *et al.* In situ distance measurements in a membrane transporter using maleimide functionalized orthogonal spin labels and 5-pulse electron-electron double resonance spectroscopy. *J. Magn. Reson. Open* **10**–**11**, 100041 (2022).

139. Gopinath, A., Rath, T., Morgner, N. & Joseph, B. Lateral gating mechanism and plasticity of the BAM complex in micelles and E. coli. *PNAS Nexus* pgae019 (2024) doi:10.1093/pnasnexus/pgae019.

140. Omote, H., Figler, R. A., Polar, M. K. & Al-Shawi, M. K. Improved Energy Coupling of Human P-glycoprotein by the Glycine 185 to Valine Mutation. *Biochemistry* **43**, 3917–3928 (2004).

141. Lewinson, O., Lee, A. T., Locher, K. P. & Rees, D. C. A distinct mechanism for the ABC transporter BtuCD-BtuF revealed by the dynamics of complex formation. *Nat. Struct. Mol. Biol.* **17**, 332–338 (2010).

142. Videmann, B., Tep, J., Cavret, S. & Lecoeur, S. Epithelial transport of deoxynivalenol: Involvement of human P-glycoprotein (ABCB1) and multidrug resistance-associated

protein 2 (ABCC2). *Food Chem. Toxicol.* **45**, 1938–1947 (2007).

143. de Boer, M., Cordes, T. & Poolman, B. Kinetic Modelling of Transport Inhibition by Substrates in ABC Importers. *J. Mol. Biol.* **432**, 5565–5576 (2020).

144. Millan, C. R. *et al.* A Conserved Motif in Intracellular Loop 1 Stabilizes the Outward-Facing Conformation of TmrAB. *J. Mol. Biol.* **433**, 166834 (2021).

145. Vergani, P., Nairn, A. C. & Gadsby, D. C. On the Mechanism of MgATP-dependent Gating of CFTR Cl− Channels . *J. Gen. Physiol.* **121**, 17–36 (2002).

146. Wilson, C. B. & Tycko, R. Millisecond Time-Resolved Solid-State NMR Initiated by Rapid Inverse Temperature Jumps. *J. Am. Chem. Soc.* **144**, 9920–9925 (2022).

147. Schmidt, T. *et al.* Time-resolved DEER EPR and solid-state NMR afford kinetic and structural elucidation of substrate binding to Ca2+-ligated calmodulin. *Proc. Natl. Acad. Sci.* **119**, e2122308119 (2022).

148. Jeon, J., Blake Wilson, C., Yau, W.-M., Thurber, K. R. & Tycko, R. Time-resolved solid state NMR of biomolecular processes with millisecond time resolution. *J. Magn. Reson.* **342**, 107285 (2022).

149. Syberg, F., Suveyzdis, Y., Kötting, C., Gerwert, K. & Hofmann, E. Time-resolved Fourier Transform Infrared Spectroscopy of the Nucleotide-binding Domain from the ATP-binding Cassette Transporter MsbA: ATP HYDROLYSIS IS THE RATE-LIMITING STEP IN THE CATALYTIC CYCLE*. *J. Biol. Chem.* **287**, 23923–23931 (2012).

150. Mann, D., Labudda, K., Zimmermann, S., Vocke, K. U. & Gasper, R. ATP binding and ATP hydrolysis in full-length MsbA monitored via time-resolved Fourier transform infrared spectroscopy. *Biol. Chem.* **404**, 727–737 (2023).

151. Kim, J. G., Kim, T. W., Kim, J. & Ihee, H. Protein Structural Dynamics Revealed by Time-Resolved X-ray Solution Scattering. *Acc. Chem. Res.* **48**, 2200–2208 (2015).

152. Josts, I. *et al.* Structural Kinetics of MsbA Investigated by Stopped-Flow Time-Resolved Small-Angle X-Ray Scattering. *Structure* **28**, 348-354.e3 (2020).

153. Josts, I. *et al.* Photocage-initiated time-resolved solution X-ray scattering investigation of protein dimerization. *IUCrJ* **5**, 667–672 (2018).

154. Schuler, B. Single-molecule FRET of protein structure and dynamics - a primer. *J. Nanobiotechnology* **11**, S2 (2013).

155. Gouridis, G. *et al.* Conformational dynamics in substrate-binding domains influences transport in the ABC importer GlnPQ. *Nat. Struct. Mol. Biol.* **22**, 57–64 (2015).

156. Husada, F. *et al.* Conformational dynamics of the ABC transporter McjD seen by single-molecule FRET. *EMBO J.* **37**, (2018).

157. Goudsmits, J. M. H., Slotboom, D. J. & van Oijen, A. M. Single-molecule visualization of conformational changes and substrate transport in the vitamin B(12) ABC importer BtuCD-F. *Nat. Commun.* **8**, 1652 (2017).

158. Yang, M. *et al.* Single-molecule probing of the conformational homogeneity of the ABC transporter BtuCD. *Nat. Chem. Biol.* **14**, 715–722 (2018).

159. Wang, L. *et al.* Characterization of the kinetic cycle of an ABC transporter by single-molecule and cryo-EM analyses. *Elife* **9**, e56451 (2020).

160. Liu, Y., Liu, Y., He, L., Zhao, Y. & Zhang, X. C. Single-molecule fluorescence studies on the conformational change of the ABC transporter MsbA. *Biophys. Reports* **4**, 153–165 (2018).

161. Zoghbi, M. E., Fuson, K. L., Sutton, R. B. & Altenberg, G. A. Kinetics of the association/dissociation cycle of an ATP-binding cassette nucleotide-binding domain. *J. Biol. Chem.* **287**, 4157–4164 (2012).

162. Kaufmann, R., Yadid, I. & Goldfarb, D. A novel microfluidic rapid freeze-quench device for trapping reactions intermediates for high field EPR analysis. *J. Magn. Reson.* **230**, 220–226 (2013).

163. Dockter, C. *et al.* Refolding of the integral membrane protein light-harvesting complex II monitored by pulse EPR. *Proc. Natl. Acad. Sci. U. S. A.* **106**, 18485–18490 (2009).

164. Collauto, A. *et al.* Rates and equilibrium constants of the ligand-induced conformational transition of an HCN ion channel protein domain determined by DEER spectroscopy. *Phys. Chem. Chem. Phys.* **19**, 15324–15334 (2017).

165. Hett, T. *et al.* Spatiotemporal Resolution of Conformational Changes in Biomolecules by Combining Pulsed Electron–Electron Double Resonance Spectroscopy with Microsecond Freeze-Hyperquenching. *J. Am. Chem. Soc.* **143**, 6981–6989 (2021).

166. Schweiger, A. & Jeschke, G. *Principles of Pulse Electron Paramagnetic Resonance*. (Oxford University Press, 2001).

167. Goldfarb, D. & Stoll, S. *EPR Spectroscopy: Fundamentals and Methods*. (Wiley, 2018).

168. Hemminga, M. A. & Berliner, L. *ESR Spectroscopy in Membrane Biophysics*. (Springer, 2007).

169. Liu, J. *et al.* Metalloproteins containing cytochrome, iron-sulfur, or copper redox centers. *Chem. Rev.* **114**, 4366–4469 (2014).

170. Weaver, E. C. EPR Studies of Free Radicals in Photosynthetic Systems. *Annu. Rev. Plant Physiol.* **19**, 283–294 (1968).

171. Joseph, B. *et al.* Selective High-Resolution Detection of Membrane Protein-Ligand

Interaction in Native Membranes Using Trityl-Nitroxide PELDOR. *Angew. Chemie Int. Ed.* **55**, 11538–11542 (2016).

172. Yang, Y. *et al.* A Reactive, Rigid Gd(III) Labeling Tag for In-Cell EPR Distance Measurements in Proteins. *Angew. Chem. Int. Ed. Engl.* **56**, 2914–2918 (2017).

173. Cunningham, T. F., Putterman, M. R., Desai, A., Horne, W. S. & Saxena, S. The double-histidine Cu^{2+}-binding motif: a highly rigid, site-specific spin probe for electron spin resonance distance measurements. *Angew. Chem. Int. Ed. Engl.* **54**, 6330–6334 (2015).

174. Altenbach, C., Flitsch, S. L., Khorana, H. G. & Hubbell, W. L. Structural studies on transmembrane proteins. 2. Spin labeling of bacteriorhodopsin mutants at unique cysteines. *Biochemistry* **28**, 7806–7812 (1989).

175. Jeschke, G. MMM: A toolbox for integrative structure modeling. *Protein Sci.* **27**, 76–85 (2018).

176. Sahu, I. D. & Lorigan, G. A. Electron Paramagnetic Resonance as a Tool for Studying Membrane Proteins. *Biomolecules* **10**, (2020).

177. Huber, M. *et al.* Phase memory relaxation times of spin labels in human carbonic anhydrase II: pulsed EPR to determine spin label location. *Biophys. Chem.* **94**, 245–256 (2001).

178. Borbat, P. P., Georgieva, E. R. & Freed, J. H. Improved Sensitivity for Long-Distance Measurements in Biomolecules: Five-Pulse Double Electron–Electron Resonance. *J. Phys. Chem. Lett.* **4**, 170–175 (2013).

179. Tseitlin, M., Quine, R. W., Rinard, G. A., Eaton, S. S. & Eaton, G. R. Digital EPR with an arbitrary waveform generator and direct detection at the carrier frequency. *J. Magn. Reson.* **213**, 119–125 (2011).

180. Doll, A. *et al.* Gd(III)-Gd(III) distance measurements with chirp pump pulses. *J. Magn. Reson.* **259**, 153–162 (2015).

181. Jeschke, G. DEER Distance Measurements on Proteins. *Annu. Rev. Phys. Chem.* **63**, 419–446 (2012).

182. Milov, A. D., Salikhov, K. M. & Shirov, M. D. Application of ELDOR in electron-spin echo for paramagnetic center space distribution in solids. *Fiz. Tverd. Tela* **23**, 975–982 (1981).

183. Milov, A. D. & Tsvetkov, Y. D. Double electron-electron resonance in electron spin echo: Conformations of spin-labeled poly-4-vinilpyridine in glassy solutions. *Appl. Magn. Reson.* **12**, 495–504 (1997).

184. Pannier, M., Veit, S., Godt, A., Jeschke, G. & Spiess, H. W. Dead-time free measurement of dipole-dipole interactions between electron spins. *J. Magn. Reson.* **142**, 331–340

(2000).

185. Martin, R. E. *et al.* Determination of End-to-End Distances in a Series of TEMPO Diradicals of up to 2.8 nm Length with a New Four-Pulse Double Electron Electron Resonance Experiment. *Angew. Chem. Int. Ed. Engl.* **37**, 2833–2837 (1998).

186. Breitgoff, F. D., Polyhach, Y. O. & Jeschke, G. Reliable nanometre-range distance distributions from 5-pulse double electron electron resonance. *Phys. Chem. Chem. Phys.* **19**, 15754–15765 (2017).

187. Bock, C. W. *et al.* Manganese as a Replacement for Magnesium and Zinc : Functional Comparison of the Divalent Ions. **2**, 7360–7372 (1999).

188. Schramm, V. L. *Manganese in metabolism and enzyme function*. (Elsevier, 2012).

189. Morbach, S., Tebbe, S. & Schneiders, E. The ATP-binding Cassette (ABC) Transporter for Maltosehktaltodextrins of Salmonella typhimurium. *J. Biol. Chem.* **268**, 18617–18621 (1993).

190. Giannoulis, A., Feintuch, A., Unger, T., Amir, S. & Goldfarb, D. Monitoring the Conformation of the Sba1/Hsp90 Complex in the Presence of Nucleotides with Mn(II)-Based Double Electron − Electron Resonance. (2021) doi:10.1021/acs.jpclett.1c03641.

191. Berezin, A. S. *et al.* A red-emitting Mn(II)-based coordination polymer build on 1,2,4,5-tetrakis(diphenylphosphinyl)benzene. *Inorg. Chem. Commun.* **107**, 107473 (2019).

192. Akhmetzyanov, D., Plackmeyer, J., Endeward, B., Denysenkov, V. & Prisner, T. F. Pulsed electron-electron double resonance spectroscopy between a high-spin Mn(2+) ion and a nitroxide spin label. *Phys. Chem. Chem. Phys.* **17**, 6760–6766 (2015).

193. Meyer, A. & Schiemann, O. PELDOR and RIDME Measurements on a High-Spin Manganese(II) Bisnitroxide Model Complex. *J. Phys. Chem. A* **120**, 3463–3472 (2016).

194. Collauto, A., Mishra, S., Litvinov, A., Mchaourab, H. S. & Goldfarb, D. Direct Spectroscopic Detection of ATP Turnover Reveals Mechanistic Divergence of ABC Exporters. *Structure* **25**, 1264-1274.e3 (2017).

195. Kaur, H. *et al.* Unexplored Nucleotide Binding Modes for the ABC Exporter MsbA. *J. Am. Chem. Soc.* **140**, 14112–14125 (2018).

196. Wiegand, T. *et al.* Solid-state NMR and EPR Spectroscopy of Mn2+-Substituted ATP-Fueled Protein Engines. *Angew. Chemie Int. Ed.* **56**, 3369–3373 (2017).

197. Ketter, S. & Joseph, B. Gd3+–Trityl–Nitroxide Triple Labeling and Distance Measurements in the Heterooligomeric Cobalamin Transport Complex in the Native Lipid Bilayers. *J. Am. Chem. Soc.* **145**, 960–966 (2023).

198. Jeschke, G. Dipolar Spectroscopy – Double-Resonance Methods. in *eMagRes* 1459–

1476 (2016).

199. Fábregas Ibáñez, L., Jeschke, G. & Stoll, S. DeerLab: a comprehensive software package for analyzing dipolar electron paramagnetic resonance spectroscopy data. *Magn. Reson. (Gottingen, Ger.* **1**, 209–224 (2020).

200. Edwards, T. H. & Stoll, S. A Bayesian approach to quantifying uncertainty from experimental noise in DEER spectroscopy. *J. Magn. Reson.* **270**, 87–97 (2016).

201. Tikhonov, A. N. Solution of incorrectly formulated problems and the regularization method. *Sov Dok* **4**, 1035–1038 (1963).

202. Hansen, P. C. Analysis of Discrete Ill-Posed Problems by Means of the L-Curve. *SIAM Rev.* **34**, 561–580 (1992).

203. Edwards, T. H. & Stoll, S. Optimal Tikhonov regularization for DEER spectroscopy. *J. Magn. Reson.* **288**, 58–68 (2018).

204. Sima, D. M. & Van Huffel, S. Separable nonlinear least squares fitting with linear bound constraints and its application in magnetic resonance spectroscopy data quantification. *J. Comput. Appl. Math.* **203**, 264–278 (2007).

205. Budil, D. E., Lee, S., Saxena, S. & Freed, J. H. Nonlinear-Least-Squares Analysis of Slow-Motion EPR Spectra in One and Two Dimensions Using a Modified Levenberg–Marquardt Algorithm. *J. Magn. Reson. Ser. A* **120**, 155–189 (1996).

206. Sen, K. I., Logan, T. M. & Fajer, P. G. Protein dynamics and monomer-monomer interactions in AntR activation by electron paramagnetic resonance and double electron-electron resonance. *Biochemistry* **46**, 11639–11649 (2007).

207. Barth, K. *et al.* Thermodynamic Basis for Conformational Coupling in an ATP- Binding Cassette Exporter. (2020) doi:10.1021/acs.jpclett.0c01876.

208. Brandon, S., Beth, A. H. & Hustedt, E. J. The global analysis of DEER data. *J. Magn. Reson.* **218**, 93–104 (2012).

209. Rein, S., Lewe, P., Andrade, S. L., Kacprzak, S. & Weber, S. Global analysis of complex PELDOR time traces. *J. Magn. Reson.* **295**, 17–26 (2018).

210. Stefan, E., Hofmann, S. & Tampé, R. A single power stroke by ATP binding drives substrate translocation in a heterodimeric ABC transporter. *Elife* **9**, (2020).

211. Smith, C. A. & Rayment, I. X-ray structure of the magnesium(II)·ADP·vanadate complex of the Dictyostelium discoideum myosin motor domain to 1.9 Å resolution. *Biochemistry* **35**, 5404–5417 (1996).

212. Barth, K. *et al.* Conformational Coupling and trans-Inhibition in the Human Antigen Transporter Ortholog TmrAB Resolved with Dipolar EPR Spectroscopy. *J. Am. Chem.*

Soc. **140**, 4527–4533 (2018).

213. Rudolph, M., Tampé, R. & Joseph, B. Time-Resolved Mn2+−NO and NO−NO Distance Measurements Reveal That Catalytic Asymmetry Regulates Alternating Access in an ABC Transporter. *Angew. Chemie - Int. Ed.* **62**, e202307091, (2023).

214. Valera, S. *et al.* Accurate Extraction of Nanometer Distances in Multimers by Pulse EPR. *Chemistry* **22**, 4700–4703 (2016).

215. Göddeke, H. *et al.* Atomistic Mechanism of Large-Scale Conformational Transition in a Heterodimeric ABC Exporter. *J. Am. Chem. Soc.* **140**, 4543–4551 (2018).

216. Takeuchi, K., Imai, M. & Shimada, I. Conformational equilibrium defines the variable induction of the multidrug-binding transcriptional repressor QacR. *Proc. Natl. Acad. Sci.* **116**, 19963–19972 (2019).

217. De Simone, A., Montalvao, R. W. & Vendruscolo, M. Determination of Conformational Equilibria in Proteins Using Residual Dipolar Couplings. *J. Chem. Theory Comput.* **7**, 4189–4195 (2011).

218. Cafiso, D. S. Identifying and Quantitating Conformational Exchange in Membrane Proteins Using Site-Directed Spin Labeling. *Acc. Chem. Res.* **47**, 3102–3109 (2014).

219. Kieuvongngam, V. & Chen, J. Structures of the peptidase-containing ABC transporter PCAT1 under equilibrium and nonequilibrium conditions. *Proc. Natl. Acad. Sci. U. S. A.* **119**, (2022).

220. Liu, Y., Liu, Y., He, L., Zhao, Y. & Zhang, X. C. Single-molecule fluorescence studies on the conformational change of the ABC transporter MsbA. *Biophys. Reports* **4**, 153–165 (2018).

221. Jakobsson, E. *et al.* Towards a Unified Understanding of Lithium Action in Basic Biology and its Significance for Applied Biology. *J. Membr. Biol.* **250**, 587–604 (2017).

222. Birch, N. J. Lithium and Magnesium-Dependent Enzymes. *Lancet* **304**, 965–966 (1974).

223. Zoghbi, M. E. & Altenberg, G. A. Hydrolysis at one of the two nucleotide-binding sites drives the dissociation of ATP-binding cassette nucleotide-binding domain dimers. *J. Biol. Chem.* **288**, 34259–34265 (2013).

224. Silva, V. H. C., Aquilanti, V., de Oliveira, H. C. B. & Mundim, K. C. Uniform description of non-Arrhenius temperature dependence of reaction rates, and a heuristic criterion for quantum tunneling vs classical non-extensive distribution. *Chem. Phys. Lett.* **590**, 201–207 (2013).

225. Wang, W. & Roberts, C. J. Non-Arrhenius protein aggregation. *AAPS J.* **15**, 840–851 (2013).

226. Bock, C., Zollmann, T., Lindt, K.-A., Tampé, R. & Abele, R. Peptide translocation by the lysosomal ABC transporter TAPL is regulated by coupling efficiency and activation energy. *Sci. Rep.* **9**, 11884 (2019).

227. Neumann, L., Abele, R. & Tampé, R. Thermodynamics of Peptide Binding to the Transporter Associated with Antigen Processing (TAP). *J. Mol. Biol.* **324**, 965–973 (2002).

228. Bao, H., Dalal, K., Cytrynbaum, E. & Duong, F. Sequential Action of MalE and Maltose Allows Coupling ATP Hydrolysis to Translocation in the MalFGK2 Transporter*. *J. Biol. Chem.* **290**, 25452–25460 (2015).

229. Kucher, S. *et al.* Orthogonal spin labeling using click chemistry for in vitro and in vivo applications. *J. Magn. Reson.* **275**, 38–45 (2017).

230. Vitali, V., Ackermann, K., Hagelueken, G. & Bode, B. E. Spectroscopically Orthogonal Labelling to Disentangle Site-Specific Nitroxide Label Distributions. *Appl. Magn. Reson.* (2023) doi:10.1007/s00723-023-01611-1.

231. Wort, J. L., Arya, S., Ackermann, K., Stewart, A. J. & Bode, B. E. Pulse Dipolar EPR Reveals Double-Histidine Motif CuII–NTA Spin-Labeling Robustness against Competitor Ions. *J. Phys. Chem. Lett.* **12**, 2815–2819 (2021).

232. Hofmann, S. *et al.* Conformation space of a heterodimeric ABC exporter under turnover conditions. *Nature* **571**, 580–583 (2019).

233. Hutter, C. A. J. *et al.* The extracellular gate shapes the energy profile of an ABC exporter. *Nat. Commun.* **10**, 1–13 (2019).

234. Zaitseva, J. *et al.* A structural analysis of asymmetry required for catalytic activity of an ABC-ATPase domain dimer. *EMBO J.* **25**, 3432–3443 (2006).

235. Aittoniemi, J., de Wet, H., Ashcroft, F. M. & Sansom, M. S. P. Asymmetric Switching in a Homodimeric ABC Transporter: A Simulation Study. *PLOS Comput. Biol.* **6**, e1000762 (2010).

236. Hetzke, T. *et al.* Binding of tetracycline to its aptamer determined by 2D-correlated Mn2+ hyperfine spectroscopy. *J. Magn. Reson.* **303**, 105–114 (2019).

237. Oloo, E. O., Fung, E. Y. & Tieleman, D. P. The Dynamics of the MgATP-driven Closure of MalK, the Energy-transducing Subunit of the Maltose ABC Transporter*. *J. Biol. Chem.* **281**, 28397–28407 (2006).

238. Patzlaff, J. S., van der Heide, T. & Poolman, B. The ATP/Substrate Stoichiometry of the ATP-binding Cassette (ABC) Transporter OpuA*. *J. Biol. Chem.* **278**, 29546–29551 (2003).

239. Chang, X.-B., Hou, Y.-X. & Riordan, J. R. Stimulation of ATPase Activity of Purified

Multidrug Resistance-associated Protein by Nucleoside Diphosphates*. *J. Biol. Chem.* **273**, 23844–23848 (1998).

240. Gorbulev, S., Abele, R. & Tampé, R. Allosteric crosstalk between peptide-binding, transport, and ATP hydrolysis of the ABC transporter TAP. *Proc. Natl. Acad. Sci.* **98**, 3732–3737 (2001).

241. Amann, S. J., Keihsler, D., Bodrug, T., Brown, N. G. & Haselbach, D. Frozen in time: analyzing molecular dynamics with time-resolved cryo-EM. *Structure* **31**, 4–19 (2023).

242. Papasergi-Scott, M. M. *et al.* Time-resolved cryo-EM of G protein activation by a GPCR. *bioRxiv* 2023.03.20.533387 (2023) doi:10.1101/2023.03.20.533387.

APPENDIX

Table S1. Pulse settings. The following pulses were used for Mn^{2+}-NO and Mn^{2+}- Mn^{2+} PELDOR experiments.

Sample(s)	Figure	ν_{pump} (ns)	ν_{obs} (ns)	Pulse shape
416^{A} (WT*), ATP-Mn^{2+}	1c	12	32	Rectangular
416^{A} (WT*), ATP-VO_4^{3-}-Mn^{2+}	1c	10	32	Rectangular
458^{B} (WT*), ATP-Mn^{2+}	1d	32	32	Chirped
458^{B} (WT*), ATP-VO_4^{3-}-Mn^{2+}	1d	32	32	Chirped
288^{A},461^{A}-272^{B} (WT*), ATP-Mn^{2+}	2c	30	32	Gaussian
288^{A},461^{A}-272^{B} (WT*), ATP-VO_4^{3-}-Mn^{2+}	2c	30	32	Gaussian
288^{A},461^{A}-272^{B} (E-to-Q), ATP-Mn^{2+}	2d	12	32	Gaussian
288^{A},461^{A}-272^{B} (E-to-Q), ATP-Mn^{2+}	2d	20	24	Gaussian
288^{A},461^{A}-272^{B} (WT*), ATP-Mn^{2+} (TR series)	3a	16	32	Gaussian

Table S2. Fitting values from V288R1^{A}–E272R1^{B} under ATP-EDTA conditions. The values for P_{OF} from V288R1^{A}–E272R1^{B} either in the WT* or E-to-Q background under non-hydrolysing (ATP-EDTA) conditions as determined by linear combination of the respective Gaussians ($P_{OF} + P_{IF} = 1$) with the distance restraints r_{IF} and r_{OF} are given for every temperature and time point with a 95 % confidence interval based on the quality of the fit. Replicates (n = 1,2,3) are listed for comparison.

T (°C)	t (s)	WT* ATP-EDTA			E-to-Q, ATP-EDTA
		n = 1	n = 2	n = 3	n = 1
30	10	0.176 ± 0.017	0.167 ± 0.02		0.192 ± 0.013
	20	0.168 ± 0.017	0.178 ± 0.022		0.208 ± 0.015
	40	0.205 ± 0.022	0.182 ± 0.022		0.269 ± 0.016
	80	0.205 ± 0.021	0.192 ± 0.022		0.336 ± 0.019
	160	0.262 ± 0.023	0.226 ± 0.026		0.424 ± 0.021
	300	0.293 ± 0.022	0.239 ± 0.024		0.483 ± 0.022
40	10	0.180 ± 0.017	0.219 ± 0.019	0.146 ± 0.012	0.421 ± 0.014
	20	0.211 ± 0.018	0.232 ± 0.015	0.194 ± 0.012	0.470 ± 0.016
	40	0.222 ± 0.023	0.276 ± 0.019	0.235 ± 0.014	0.575 ± 0.013
	80	0.284 ± 0.020	0.324 ± 0.020	0.325 ± 0.016	0.623 ± 0.016
	160	0.359 ± 0.020	0.385 ± 0.021	0.372 ± 0.016	0.664 ± 0.020
	300	0.397 ± 0.020	0.422 ± 0.025	0.435 ± 0.016	0.667 ± 0.018
50	10	0.268 ± 0.016			0.552 ± 0.019
	20	0.332 ± 0.019			0.614 ± 0.021
	40	0.370 ± 0.019			0.633 ± 0.020
	80	0.434 ± 0.019			0.649 ± 0.018
	160	0.500 ± 0.020			0.668 ± 0.017
	300	0.556 ± 0.021			0.678 ± 0.020

Table S3. Fitting values from A416R1^{A}–L458R1^{B} and V461R1^{A}–D349R1^{B} under ATP-EDTA conditions. The values for P_{closed} as determined by linear combination of the respective Gaussians ($P_{open} + P_{closed} = 1$, or $P_{open} + P_{closed} + P_{fix} = 1$, with $P_{fix} = 0.1$) with the distance restraints r_{open} and r_{closed} and r_{fix} are given for every temperature and time point with a 95 % confidence interval based on the quality of the. Replicates (n = 1,2) are listed for comparison.

T (°C)	t (s)	A416C^{A}–L458C^{B}		V461C^{A}–D349C^{B}
		n = 1	n = 2	n = 1
30	10	0.126 ± 0.017		0.150 ± 0.040
	20	0.134 ± 0.014		0.156 ± 0.028
	40	0.149 ± 0.026		0.137 ± 0.023
	80	0.162 ± 0.013		0.195 ± 0.032
	160	0.204 ± 0.017		0.202 ± 0.025
	300	0.240 ± 0.012		0.244 ± 0.041
40	10	0.153 ± 0.026	0.138 ± 0.018	
	20	0.166 ± 0.010	0.150 ± 0.015	
	40	0.203 ± 0.015	0.211 ± 0.023	
	80	0.286 ± 0.010	0.292 ± 0.008	
	160	0.348 ± 0.016	0.365 ± 0.011	
	300	0.460 ± 0.011	0.415 ± 0.008	
50	10	0.196 ± 0.015		0.101 ± 0.020
	20	0.214 ± 0.013		0.163 ± 0.023
	40	0.284 ± 0.010		0.205 ± 0.032
	80	0.391 ± 0.008		0.303 ± 0.030
	160	0.457 ± 0.011		0.265 ± 0.030
	300	0.518 ± 0.011		0.310 ± 0.027

Table S4. Fitting values from experiments under turnover conditions. The values of P_{OF} from V288R1^{A}–E272R1^{B} and P_{closed} from both A416R1^{A}–L458R1^{B} and V461R1^{A}–D349R1^{B} under turnover conditions (ATP-Mg^{2+}) as described in **Table S2** and **Table S3.** Replicates (n = 1,2) are listed for comparison.

		TMDs			
		WT* ATP-Mg^{2+}		WT* ATPγS-Mg^{2+}	
T (°C)	t (s)	n = 1	n = 2	n = 1	
40	10	0.528 ± 0.015		0.121 ± 0.016	
	20	0.550 ± 0.016	0.450 ± 0.024	0.163 ± 0.017	
	40	0.592 ± 0.016		0.253 ± 0.021	
	80	0.623 ± 0.022	0.573 ± 0.021	0.281 ± 0.021	
	160	0.636 ± 0.017		0.275 ± 0.022	
	300	0.663 ± 0.020	0.600 ± 0.024	0.399 ± 0.025	
		c-NBS		d-NBS	
		WT* ATP-Mg^{2+}		WT* ATP-Mg^{2+}	
T (°C)	t (s)	n = 1	n = 2	n = 1	n = 2
40	10	0.477 ± 0.009	0.497 ± 0.013	0.530 ± 0.030	
	20	0.502 ± 0.009		0.543 ± 0.030	0.564 ± 0.051
	40	0.513 ± 0.010	0.517 ± 0.013	0.507 ± 0.039	
	80	0.495 ± 0.010		0.534 ± 0.043	0.562 ± 0.0048
	160	0.463 ± 0.010	0.443 ± 0.012	0.509 ± 0.042	
	300	0.392 ± 0.008		0.508 ± 0.035	0.547 ± 0.055

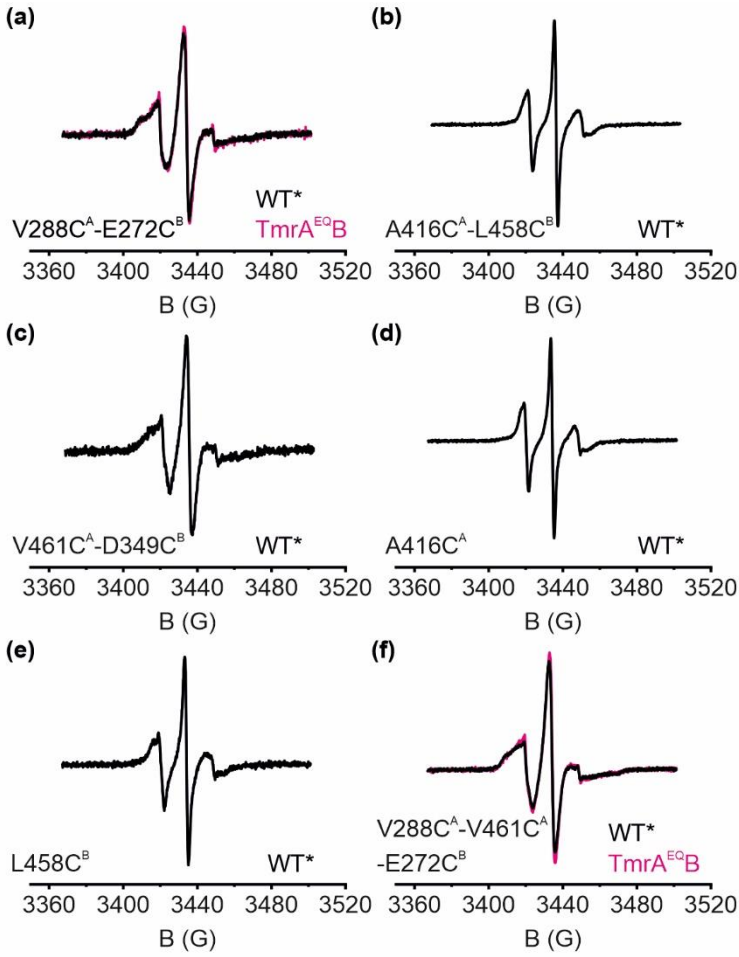

Figure S1. cw EPR spectra of the MTSL labelled TmrAB variants used in this work. The variants with the same spin label positions in the WT* and E-to-Q background are overlaid in black and pink, respectively. Spectra recorded as described in chapter 3.2.5.

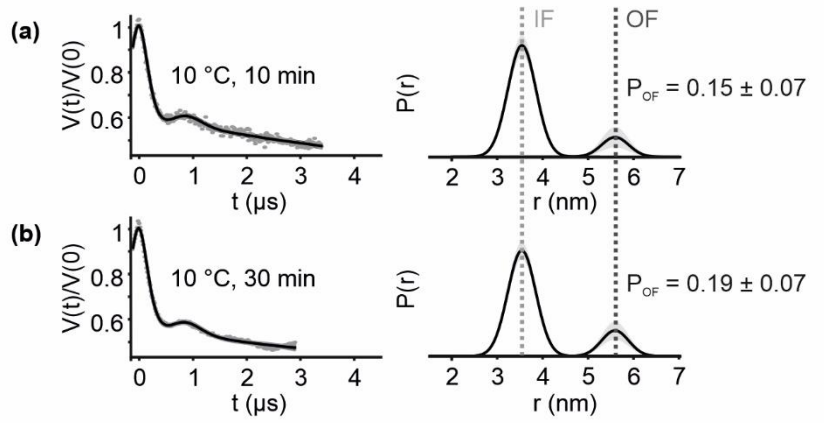

Figure S2. PELDOR measurements of V288R1^{A}-E272R1^{B} with ATP-EDTA at 10 °C. Samples were prepared under the same conditions as described in chapter 3.2.8.2 under non-hydrolyzing conditions. To simulate the sample equilibration during the kinetic experiment, samples were incubated at 10 °C for 10 min (a) or 30 min (b). Primary PELDOR data V(t)/V(0) overlaid with the fit are shown. Data were globally analyzed using DeerLab. An experimentally determined two Gaussian model corresponding to the IF and OF conformation was used for the analysis. The obtained distance distributions P(r) with a 95% confidence interval are shown. The resulting values P_{OF} are given.

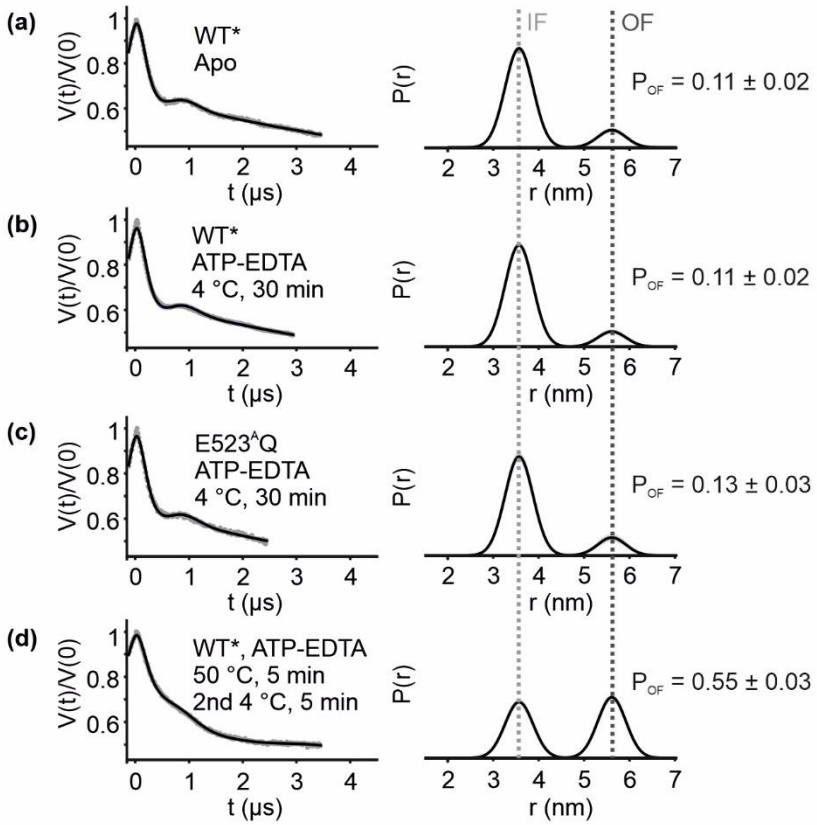

Figure S3. PELDOR measurements of V288R1^{A}-E272R1^{B} at 4 °C. (a) PELDOR measurement of V288R1^{A}-E272R1^{B} under Apo conditions as a reference. The same spin-labelled variant either in the WT* (b) or E-to-Q background (c) was incubated with ATP-EDTA at 4 °C for 30 min. (d) The same spin-labelled variant was incubated with ATP-EDTA at 50 °C for 5 min, and subsequently incubated at 4 °C for 5 min. Primary PELDOR data V(t)/V(0) overlaid with the fit are shown. Data were globally analyzed using DeerLab. An experimentally determined two Gaussian model corresponding to the IF and OF conformation was used for the analysis. The obtained distance distributions P(r) with a 95% confidence interval are shown. The resulting values POF are given.

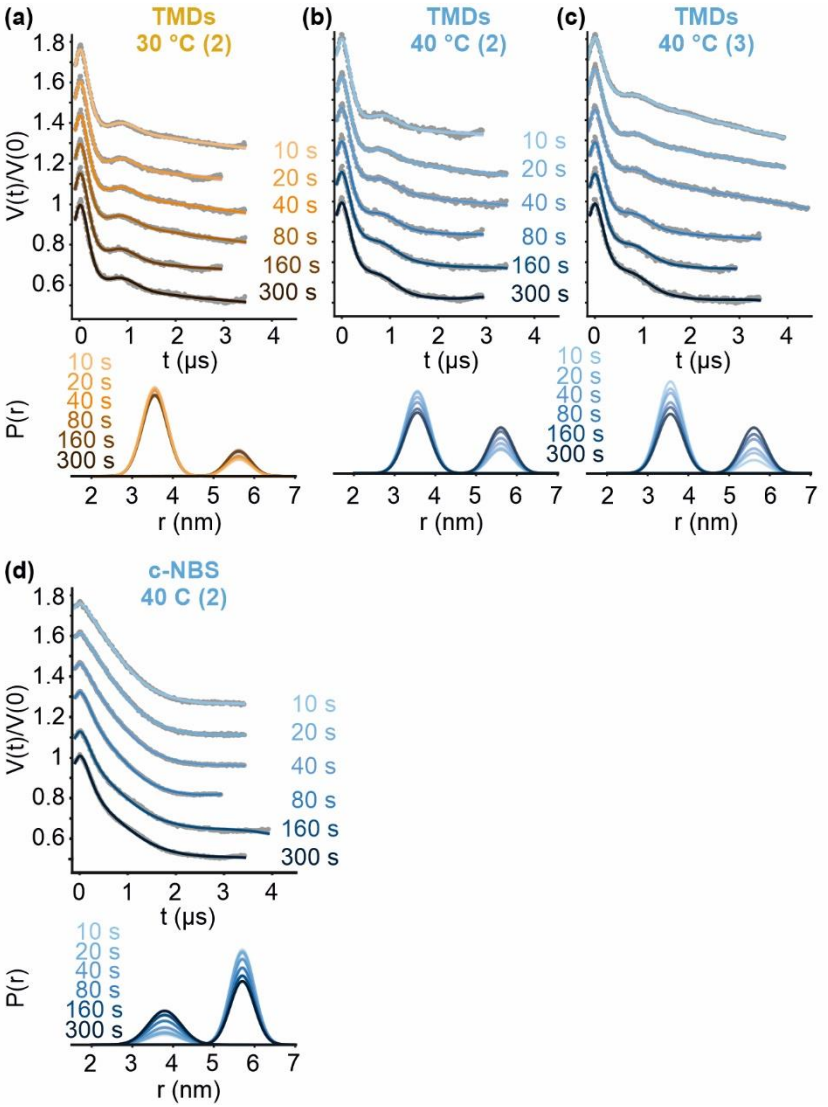

Figure S4. Replica PELDOR measurements under ATP-EDTA conditions. Biological replica of TmrAB incubated with ATP-EDTA as described in chapter 3.2.8. Replica of V288R1^{A}-E272R1^{B} incubated at 30 °C (a), and twice at 40 °C (b,c), as well as of A416R1^{A}–L458R1^{B} at 40 °C (d). PELDOR measurement and data analysis performed as described before.

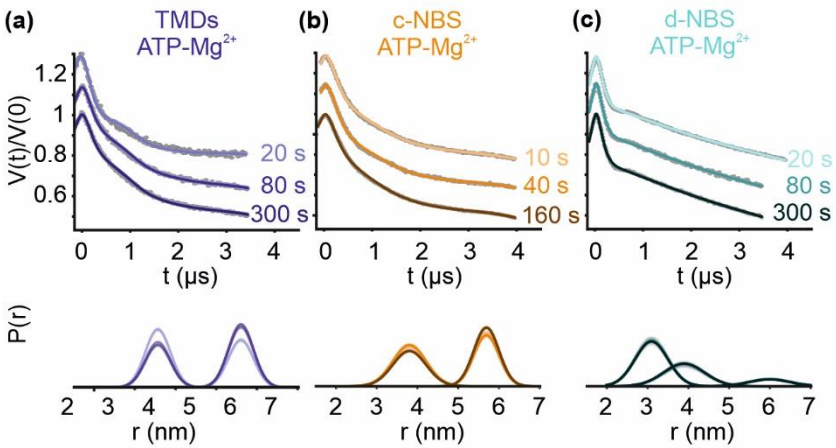

Figure S5. Replica PELDOR measurements under ATP-Mg^{2+} conditions. Biological replica of TmrAB incubated at 40 °C with ATP-Mg^{2+} as described in chapter 3.2.8. Replica of V288R1^{A}-E272R1^{B} (a), A416R1^{A}–L458R1^{B} (b) and V461R1^{A}–D349R1^{B} (c). PELDOR measurement and data analysis performed as described before.

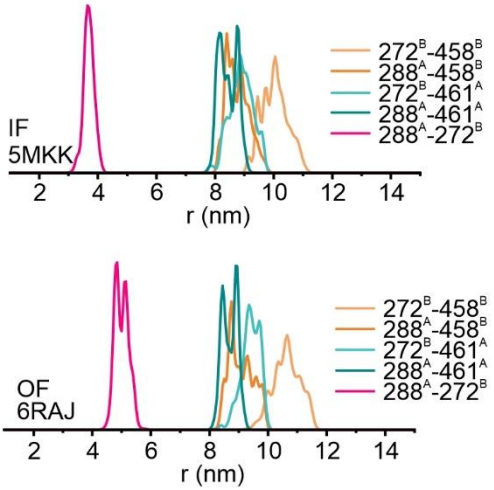

Figure S6. Simulated distance distributions for MTSL labelled cysteine variants. The distance distributions for the MTSL labelled TMD double cysteine variant V288R1^{A} – E272R1^{B} or for a combination of one these single cysteine variants with a position located at the NBS (461^{A} or 458^{B}) are overlaid. Simulations of the distance distributions were obtained on the structures of TmrAB in its IF conformation (PDB 5MKK) (a) and in its OF conformation (PDB 6RAJ) (b) using the rotamer libraries for MTSL as implemented in the MATLAB-based software package MMM.